Photophysical and electronic properties of pyrene-based 3D coordination polymers.

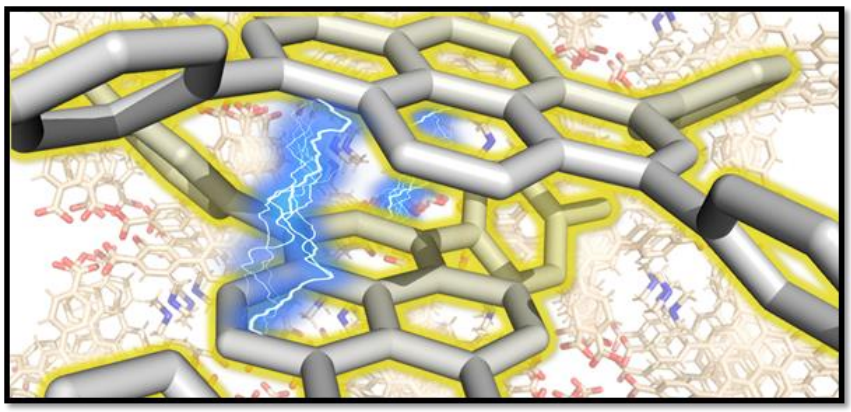

A thesis presented to

The School of Physical Sciences

at

The University of Adelaide

in fulfilment of the requirements for

The Degree of

Master of Chemical Science

by

Christopher Coleman

THE UNIVERSITY of ADELAIDE

Adelaide, Australia

May 2020

Declaration

I certify that this work contains no material which has been accepted for the award of any other degree or diploma in my name, in any university or other tertiary institution and, to the best of my knowledge and belief, contains no material previously published or written by another person, except where due reference has been made in the text. In addition, I certify that no part of this work will, in the future, be used in a submission in my name, for any other degree or diploma in any university or other tertiary institution without the prior approval of the University of Adelaide and where applicable, any partner institution responsible for the joint-award of this degree.

I acknowledge that copyright of published works contained within this thesis resides with the copyright holder(s) of those works.

I also give permission for the digital version of my thesis to be made available on the web, via the University's digital research repository, the Library Search and also through web search engines, unless permission has been granted by the University to restrict access for a period of time.

I acknowledge the support I have received for my research through the provision of an Australian Government Research Training Program Scholarship.

Chris Coleman

Publications

Structural modulation of the photophysical and electronic properties of pyrene-based 3D metal–organic frameworks derived from s-block metals

C. N. Coleman, P. C. Tapping, M. T. Huxley, T. W. Kee, D. M. Huang, C. J. Doonan and C. J. Sumby, *CrystEngComm*, 2021, **23**, 82-90. DOI:10.1039/d0ce01505a.

Acknowledgements

It has been a pleasure to work under the supervision of Prof. Christian J. Doonan and Prof. Christopher J. Sumby, whom I sincerely thank for their constant support throughout my degree. The guidance from every member of the Sumby-Doonan group has been outstanding, and I particularly acknowledge the assistance I have received from Dr. Alexandre Burgun, Dr Weibin Liang, Dr Michael Huxley, Dr Ricardo Peralta, Dr Oliver Linder-Patton, Dr Rosemary Young and Dr Matt Bull.

Aspects of this work were performed in conjunction with Dr Patrick Tapping, Tomas DePrinse, Dr Tak Kee and Associate Professor David Huang from the University of Adelaide. Travelling to Osaka to work for one month in 2018 was an inspiring experience and I thank Prof. Takahashi and Dr Ikigaki for their support and the provision of their laboratories during this time.

Much of the X-ray crystallography work conducted in this project was performed at the Australian Synchrotron using the MX1 and MX2 beamlines and access to such an outstanding facility has been pivotal to the success of the project.

The Energy Dispersive X-ray Spectroscopy (EDX) and Scanning Electron Microscope (SEM) facilities provided by Adelaide Microscopy was integral to the analysis of MOF samples throughout the project. I thank the staff at Adelaide Microscopy for their support and training in the use of their instruments.

It has genuinely been an honour to contribute to the long history of outstanding scientific research that has been and continues to be conducted at the University of Adelaide.

Table of Contents

Thesis Abstract

Metal-organic Frameworks (MOFs) are porous, crystalline materials built from metal 'nodes' and interconnecting organic ligands. The overwhelming majority of MOFs apply d-block metals as nodes. Ligand field theory describes how the orbital arrangement of transition metals forms stable and predictable co-ordination bonds with ligands resulting in a limitless variety of crystalline materials.

Used far less for coordination chemistry than the transition metals are the s-block series or the group 1 and group 2 alkali and alkaline metals. Without any d-orbitals present in these metal ions, the application of ligand field theory to predict the geometry and strength of bonds no longer applies. This can make their rational design challenging. Containing non-directional s frontier orbitals, the bonds they form with ligands are purely ionic and generally not as strong as those formed by the transition metals due to the absence of changes in ligand field stabilization energy. Despite these perceived disadvantages it would be unwise to discount the s-block metals and their potential contribution to the future of coordination chemistry.

In Chapter 2 I examine the how novel s-block MOFs can be rationally designed, fabricated, and applied in functional materials. The extent of interchromophoric interaction for structurally distinct assemblies of the π-conjugated aromatic ligand 4,4',4'',4'''-(1,3,6,8-pyrenetetrayl) tetrabenzoic acid (TBAPy) was studied within two novel metal-organic frameworks (MOFs): Na(TBAPy)(DMF) and K(TBAPy)(DMF). Spectroscopic data in conjunction with computational results indicate the extent of the interchromophoric interaction, leading to anisotropic charge transport, increased stability and distinct transient emission decay profiles, governed by the differing arrangements of ligands in the two MOFs made possible by the use of s-block metals. Now more than ever before, finding ecologically sound and low-cost solutions in materials chemistry is of the utmost importance. Non-toxic and several orders of magnitude more globally abundant than their heavier transition metal counterparts, s-block metals such as sodium and potassium are poised to play a dominant role in chemical research. Computational experiments investigating charge delocalization within the MOFs confirmed our theories and an application as a hole transport layer in a functioning LED was realized for the sodium based MOF.

Another subclass of crystalline framework materials that has received less attention than their more robust metalized counterparts is hydrogen bonded frameworks (HOFs). Lacking any metals nodes, these materials form a multitude of structures via hydrogen bonds and other supra molecular interactions. The

kinetic and thermodynamic landscape that governs the formation of these materials can be tuned by adjusting factors like heat, solvent polarity, and the steric bulk of the ligands.

In Chapter 3 I removed the metal nodes from the MOFs reported in Chapter 2 to form previously reported HOF, PFC-1. Prior work showed that the use of π rich aromatic molecules could have a dramatic stabilizing effect on HOFs as well as other porous frameworks. It was the close stacking of polycyclic ligands and its effect on the emission spectrum of PFC-1 that prompted us to investigate its potential as an organic phosphor material for use in solid state lighting. Being able to tailor the emissive properties of luminescent materials as a function of their topological net as opposed to altering their chemical structure via synthesis is an approach I believe could be of significance in the field of optoelectronics. A detailed spectroscopic study and the fabrication and optimization of a functioning device confirmed our hypothesis.

Chapter 1. Introduction

1.1 Porous Crystalline Frameworks

Porous crystalline framework materials are of intense interest to chemists due to their potential application to a diverse range of emerging technologies. Given their highly ordered structures these materials can be studied using x-ray diffraction methods, which offers valuable, atomically precise chemical insight into their fundamental properties. The recent advances in diffractor detector technology[1] in combination with the exponential growth of computational processing capability[2] has seen the field of crystallography flourish in recent decades. Thus, diffraction techniques can be employed to study interactions between atoms contained within the lattice and guest molecules.[3] Two areas of research where this technology has proven to be particularly valuable is gas adsorption[3] and catalytic mechanisms.[4]

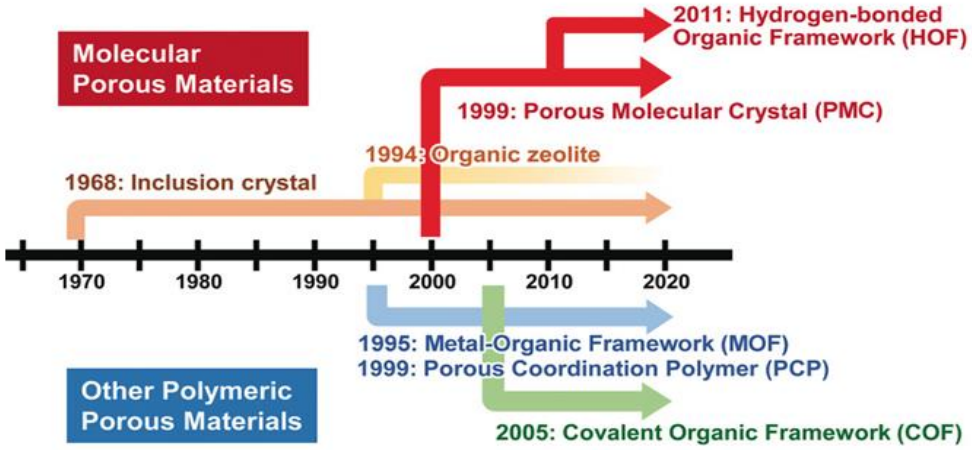

Fig. 1. Timeline for the development of porous molecular materials. (*Angew. Chem*. Int. Ed., 2019, **33**, 11160-11170).

In homogeneous synthetic chemistry, the nature of interactions between molecules is a random process that relies heavily on concentration and diffusion kinetics.[5] However, porous crystalline framework materials operate in a heterogeneous environment[6] where atoms within the crystal are locked in position and provide nano-sized cavities that can influence reactivity via confinement effects.[7] As well as providing specialized reaction environments for molecules,[8] pore networks can also provide space for the formation of nanoparticles[9] and discreet metal clusters[10] which are particularly useful for heterogeneous catalysis.[11]

Long before researchers began trying design and synthesize 3D crystalline framework materials, naturally occurring zeolites were well known for having several interesting properties which were attributed to their crystallinity[12] and porosity.[13] Consisting of crystalline aluminosilicates with primary building blocks of $SiO_4/AlO_4/MO_4$ tetrahedra, zeolites have found their way into chemical manufacturing in areas such as separation science[14] and catalysis.[15]

Robert Milton, one of the founders of zeolite synthesis chemistry, began his hydro-thermal synthesis program in the laboratories of the Linde corporation in 1949.[16] By the end of 1953, Milton and his colleagues had synthesized 20 zeolites, including 14 unknown as natural minerals.[17] The novelty and functionality of these new crystalline frameworks meant patents were soon to follow and an entire new field of chemistry was established. In 1964, in a review titled "Crystalline Molecular Sieves", the authors gave what is believed to be the first schematic representation of synthetic zeolite formation.[18]

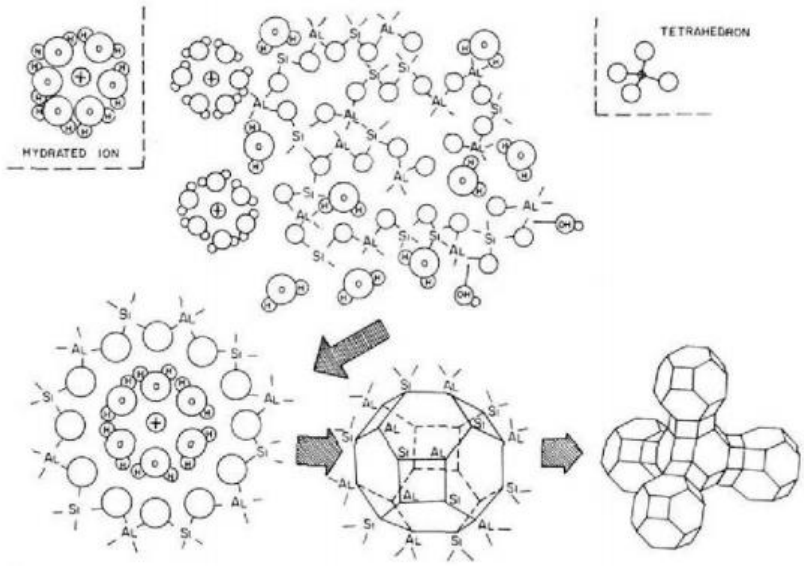

Fig. 2. The first pictorial depiction of zeolite synthesis (D. W. Breck). "Schematic representation of the formation of zeolite crystal nuclei in a hydrous gel" (*Journal of Chemical Education,* 1964, **41**, 678.)

The fixed silica compositions of zeolites mean their topology and functionality is limited but undoubtedly, they served as inspiration for material chemists to begin to design and synthesize new porous crystalline materials made from other elements. This initial research on the synthesis of 3D porous crystalline frameworks evolved over time and eventually in the late 90s a new material, metal organic frameworks (MOFs) were reported for the first time.[19]

1.2 Metal Organic Frameworks & Hydrogen Bonded Frameworks

Metal Organic Frameworks

MOFs consist of an organic linker that is connected to a metal node *via* a coordination bond.[20] The metal node can consist of a single metal ion or a cluster of metal ions (known as a secondary building unit or SBU). The organic ligands and metal SBUs can combine to form a multitude of different crystalline topologies. Molecules with negatively charged donor atoms are used to bridge and form coordination bonds with positively charged metal SBUs (see Fig 3).

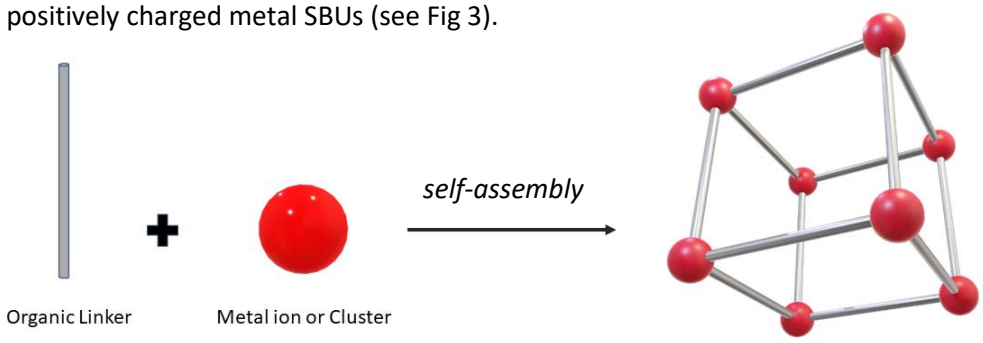

Fig. 3. Representation how of organic linkers and metal nodes can coordinate through self-assembly to form a metal organic framework.

Pioneered in the late 1990s by Prof. Omar Yaghi at UC Berkeley, MOFs have become a quickly developing research field. His paper; "Design and synthesis of an exceptionally stable and highly porous metal-organic framework" published in 1999, introduced the world to the iconic MOF-5 which revealed a material synthesized via self-assembly from simple precursors that remained highly porous and crystalline after being fully desolvated.[21] The methods used by chemists to assemble MOFs varies considerably. Optimizing suitable conditions for the growth of a new MOFs can be time consuming and difficult. Slow vapour diffusion,[22] solvothermal,[23] electrochemical,[24] mechanochemical,[25] ultrasound[26] and microwave assisted[27] are methods commonly used for creating MOFs. All these techniques for synthesising MOFs relate to what is known as “bottom up synthesis”[28]. This involves the self-assembly of atoms and molecules to form crystal planes which then stack to form nanostructures. This allows for the fabrication of nanomaterials that would otherwise be impossible to create. The alternate method of creating nanomaterials, “top down synthesis”[29] involves removing material from an existing composition until the desired nanostructure is achieved. There are limits to the resolution of such processes and the ability to form internal cavities at the nano-scale is exceptionally difficult using the top down method. Bottom-up synthesis however allows

for the internal architecture of these materials to be easily modified by exchanging precursor components prior to self-assembly.

Although not all MOFs are porous, porosity is a property that has become synonymous with MOFs.[30] Periodic porosity and the resultant high internal surface area of these materials is initially what set them apart from many other solid crystalline materials. It was quickly found that not only can the size and shape of these pores be fine-tuned though careful selection of ligands but guest molecules could be absorbed and encapsulated within the lattice. Gas separation/storage[31] and heterogeneous catalysis[32] are two areas of research that have taken advantage and rely heavily upon the porosity and high surface areas of MOFs. It is unusual to see a MOF paper that does not include isotherm data detailing experimental porosity.

As can be seen in Fig. 4, MOF-5 readily adsorbs N_2 gas into the pores until they become saturated.[33] The rate at which atoms or molecules are adsorbed and desorbed by a porous material is determined primarily by the size and shape of the pores (size of the absorbate and charged species will also impact the rate of sorption). Their size can be classified as microporous (<2 nm),[34] mesoporous (2-50 nm)[35] and macroporous (>50nm).[36]

There are number of different isotherm "types" that indicate pore size and distribution. Fig. 4 is a Type I isotherm,[37] indicating the MOF has a microporous structure and that monolayer adsorption[38] is occurring whereas a type IV isotherm[39] for example, suggests the material is mesoporous and in addition to multilayer adsorption,[40] capillary condensation[41] is also occurring resulting in a hysteresis loop indicative of mesoporous materials. For MOF researchers interested in porosity, isotherm data has become an invaluable tool.

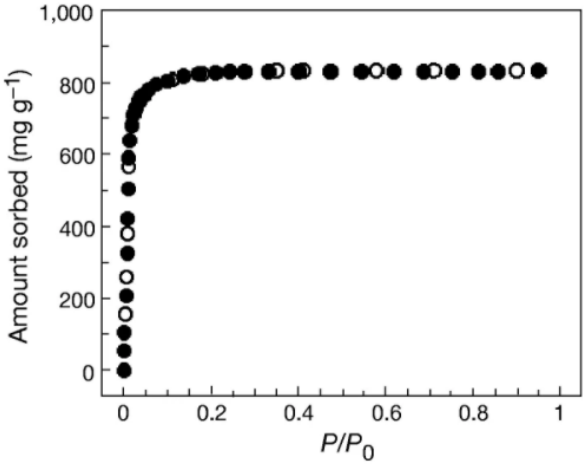

Fig. 4. Nitrogen gas sorption isotherm at 78 K for MOF-5. "Design and synthesis of an exceptionally stable and highly porous metal-organic framework". (*Nature,* 1999*,* **402,** 276–279).

Hydrogen Bonded Frameworks.

Another subset of crystalline frameworks are hydrogen bonded frameworks (HOFs).[42] Relying solely on hydrogen bonding[43] and other supramolecular interactions,[44] these crystalline materials are completely devoid of the metal nodes that are present in MOFs to connect the ligands. Instead, functional groups attached to ligands that are capable of hydrogen bonding such as OH or NH, bond with each other to form 2D and 3D topologies that in many cases look structurally very similar to MOFs.

The strength of hydrogen bonds[45] is considerably less than that of metal-ligand bonds.[46] As a result, HOFs are generally less stable than MOFs, meaning they are more prone to structural degradation due external stimuli or changes in environment.[47] Often the structure of a HOF will collapse when the materials are removed from solvent and only a handful of HOFs with high surface areas and/or permanent porosity have been reported to date.[48,49,50] They can also be susceptible to changes in pH, temperature and solvents that contain hydrogen bonding functional groups that interfere with the hydrogen bonds holding the HOF together.[51] Despite these issues concerning stability, HOF research continues to gain momentum and innovative and noteworthy hydrogen bonded structures are added to crystallographic databases daily.

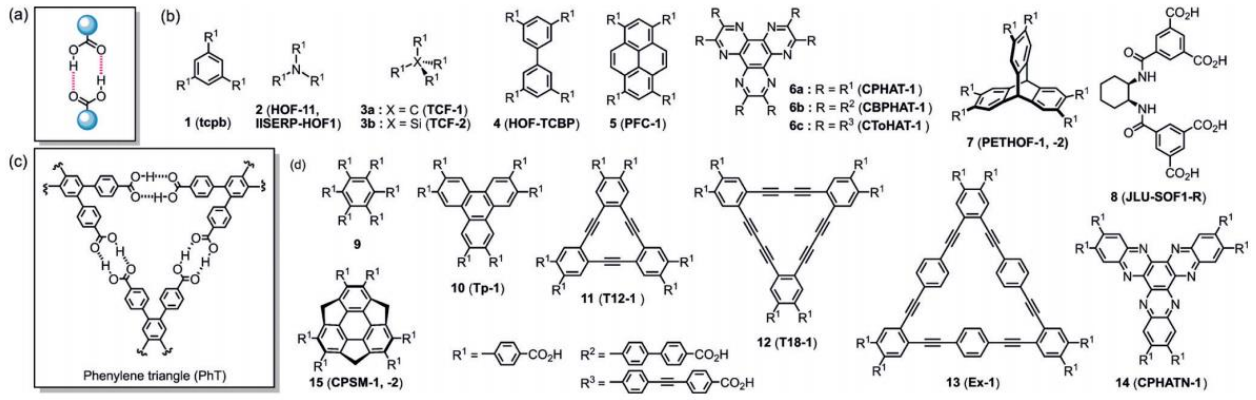

Fig. 5. **(a)** H-bonding carboxylic acid groups. **(b)** Tectons with carboxy groups that are known to form HOFs. **(c)** Cyclic H-bonded motif named phenylene triangle (PhT), which is formed by C_3-symmetric tetons **(d)** with *o*-bis(4-carboxyphenyl) aryl moieties to give low density hexagonal sheets. Literature names for the HOFs are shown in parentheses. (Angew. Chem. Int. Ed., 2019, **33**, 11160-11170).

There are several advantages HOFs have over their metalated equivalents. Consisting of only organic molecules, often the cost of the components is less.[52] Also, their ease of processability, regularly from a straightforward crystallization process, makes them suited for use as thin films and printable/flexible

electronics.[53] Finally, HOFs can easily be regenerated and purification is usually a far simpler process than with a MOF.[54]

Recently, an exceptionally stable HOF was reported: PFC-1.[55] Displaying permanent porosity with a surface area of 2122 m^2g^{-1}, PFC-1 demonstrates excellent chemical stability in a variety of harsh conditions. Consisting exclusively of tetra benzoic acid pyrene (TBAPy), the discreet carboxylic acid functionalized pyrene molecules connect with each other through intermolecular hydrogen bonds to form a single layer. Different layers are packed together through strong face to face π–π stacking interactions to form a 3D framework with one-dimensional (1D) voids (18 x23Å). Different layers are packed together in an AA packing mode, similar to those in a number of well-studied stable 2D covalent organic frameworks (COFs).[56] Computational analysis indicates significant pyrene-pyrene π orbital interactions are responsible for the exceptional stability of this material.

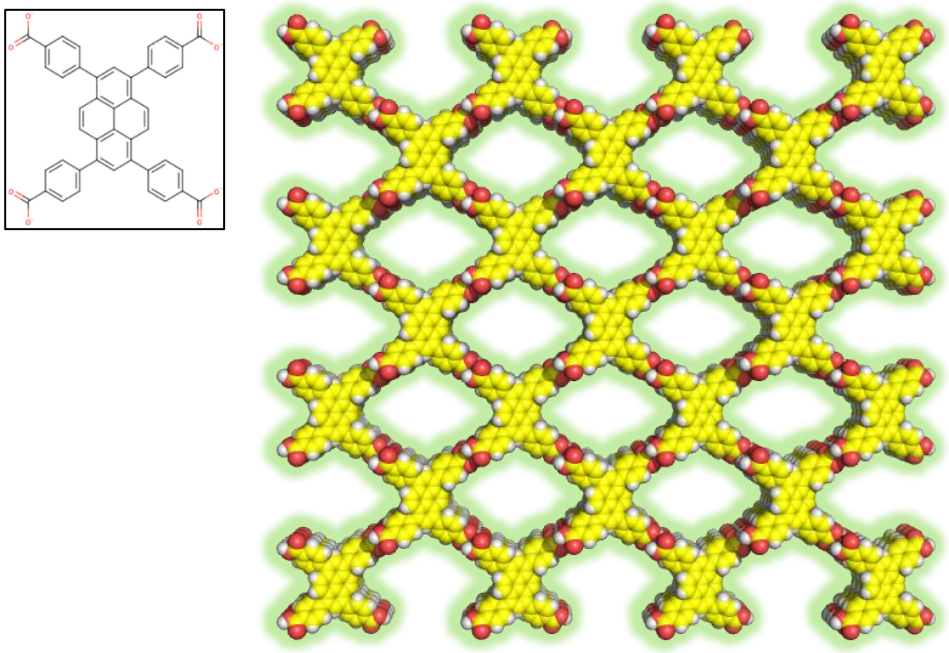

Fig. 6. Molecular structure of PFC-1 obtained by single crystal x-ray diffraction (Oxygen: red, carbon: yellow, hydrogen: white). Inset: TBAPy molecule.

The development of stable, permanently porous hydrogen bonded frameworks is an important step forward in the field of crystal engineering. For a time, MOFs were thought not to be viable functional materials because the ones that were known collapsed after desolvation.[57] The advancement of

structurally stable MOFs has led to a diverse field of research that continues to grow. Inevitably HOF chemistry will uncover more permanently porous and stable HOFs over time, however the labile nature of hydrogen bonds may prove to be the trait that sets them apart from MOFs in applications where material degradation over time, such as battery technology,[58] is a problem. HOFs can regenerate far more easily than MOFs[59] which require specific conditions and concentrations of precursors to form. One might speculate that for applications where MOFs may fail structurally over time, HOFs could repeatably regenerate. HOFs weaker hydrogen bonds could prove to be their strength.

1.3 Historical Applications and Development

Initially the applications for MOFs were focused on attempts to take advantage of their internal porosity and some of the earliest work was by Kitagawa's[60] and Yaghi's[61] groups. Early isotherm data suggested gas could be stored in MOFs.[62] Storage of natural gas, the main component of which is methane, has been attempted using MOFs and some genuine progress has been made.[63] Storage of natural gas at present requires the use of multi-stage compressors, high pressure tanks and complicated cryogenic cooling systems. A MOF that has a high electrostatic interaction with methane is M-MOF-74 (M = Mg, Mn, Co, Ni, Zn).[64] This affinity for methane is due to open metal sites in the MOF that become accessible after desolvation. Ni-MOF-74 has the highest total volumetric CH_4 capacity reported to date: (230 cm^3/cm^3 at 298 K and 35 bar).[65] Although the high polarizability of Ni^{2+} results in a high uptake, a considerable amount of methane remains bound within the MOF when the pressure is lowered, adversely affecting the working capacity of MOF-74 as a methane storage material.

It was discovered while researching the gas storage capacity for MOFs that the release of gas from the MOFs due to changes in temperature and pressure indicated that certain MOFs, due to their specific topology and open metal sites, had an affinity for particular gases over others and gas separation quickly became the focus of many research groups.[66]

The ability to separate greenhouse gases (CO_2) and energy-related gases (H_2 and CH_4) easily has been the focus of a large segment of MOF related research over the last two decades and significant progress has been made.[67] Mg-MOF-74 has an excellent CO_2 uptake at 5.28 mmol/g at 40°C and 150 mbar of pressure.[68] This is attributed to the high density of open metal sites for CO_2 to bind to. These same metal sites also have a high affinity for H_2O and the performance of MOF-74 as a low-pressure CO_2 scavenger seriously deteriorates on exposure to moisture. Notably, some CO_2 selective MOFs that are modified by

alkylamines[69] display very high CO_2 working capacities with excellent recyclabilities at the required capture conditions.

Another field which MOFs have played a major role in is that of host-guest chemistry.[70] Confined guest molecules fundamentally behave differently than free molecules dissolved in a solvent.[71] For this reason, extensive synthetic strategies that utilize the voids within MOFs have been explored over the past few decades. The types of pores present in these materials can be categorized into a number of different forms: cages,[72] channels,[73] hydrophobic,[74] hydrophilic,[75] among others. In particular, MOFs with 1D channels are of interest because they present a pathway through which guest molecules and reactants can travel.[76] Interaction potentials present on the walls of these channels can act to direct guest molecules in an ordered path facilitating a number of functionalities including catalysis[77] and ionic conduction.[78]

Catalysis has become a focus of many MOFs chemists as success in this field has the potential to have a significant impact on the chemical engineering sector.[79] The synthesis of many chemicals is costly due to the high temperatures and pressures required to drive the reaction forward. Despite the many achievements in catalysis, many of which are vital for modern industry, there is still a wide scope and necessity for catalysis solutions that address selective methane oxidation,[80] hydrogen production,[81] water splitting,[82] CO_2 reduction to methanol,[83] nitrogen fixation,[84] and water depollution[85] among others.

The latest generation of MOFs have become the preferred substrate for selective heterogeneous interactions and activations. One of the earliest reports of a MOF being used as a heterogeneous catalysis was in 1994 by Fujita *et al*.[86] Combination of $Cd(NO_3)_2$ and (4,4'-bpy) resulted in a 2D MOF that successfully and efficiently catalyzed the cyanosilylation of aldehydes. Since then a number of MOFs that are particularly stable, especially when exposed to water, have become the front runners in MOF catalysis. They include MOF-74,[87] ZIF-8,[88] CPO-27,[89] UiO-66,[90] CuBTC (HKUST-1),[91] MIL-53,[92] and MIL-101.[93]

Three categories that encompass the majority of heterogeneous catalytic reactions are photocatalysis,[94] electrocatalysis[95] and catalysis of organic reactions.[96] In the first two categories, electro and photo catalysis, the pyrolysis of MOFs[97] to form N and P doped graphitized MOF nanomaterials[98] has been found to result in efficient catalytic composite materials. Pyrolysis allows for the formation of nanocluster alloys consisting of multiple elements that can result in enhanced catalytic activity over single metal nano clusters.[99]

Photocatalysis presents a particularly convenient option with the direct conversion of solar energy to chemical energy. The photo induced water splitting properties of TiO_2[100] have been well known for several

decades and was one of the first well studied examples for photocatalysis. MOFs, with their variable composition, can be designed such that the linkers act as light harvesting molecules that can transfer charge to the metal nodes - process known as ligand to metal charge transfer.[101] The reduced metal node can then transfer the electron to the surface of a transition metal NP cocatalyst. This approach has been employed in the elusive process of H_2 production from water. Reported in 2018 by Stylianou *et al.*, MIL-125-NH_2 was used as the photocatalyst with Ni_2P nanoparticles as the cocatalyst in a solvent mixture composed of CH_3CN, NEt_3 (sacrificial electron donor), and water and used visible light irradiation (300 W Xe lamp). A H_2 generation rate as high as 894 µmol h^{-1} g^{-1} H_2 was attained.[102]

The types of reactions emerging that utilize electrocatalysis include the oxygen reduction,[103] oxygen evolution,[104] hydrogen evolution[105] and reduction of carbon dioxide.[106] The composition and strategies in designing electrocatalysts are similar to that of photocatalysts in that charge mobility within the material needs to be structurally enabled. Nanoparticles within the MOF are responsible for catalysis and traditionally Pt has become known as the ideal electrocatalytic metal.[107] Pt however is not a globally abundant element and its high price is driving researchers to find alternatives. Non-noble metals including Ti, Fe, Co, Ni, Cu, Zn, Mo, Cd, and In are being progressively introduced as alternatives to Pt.[108]

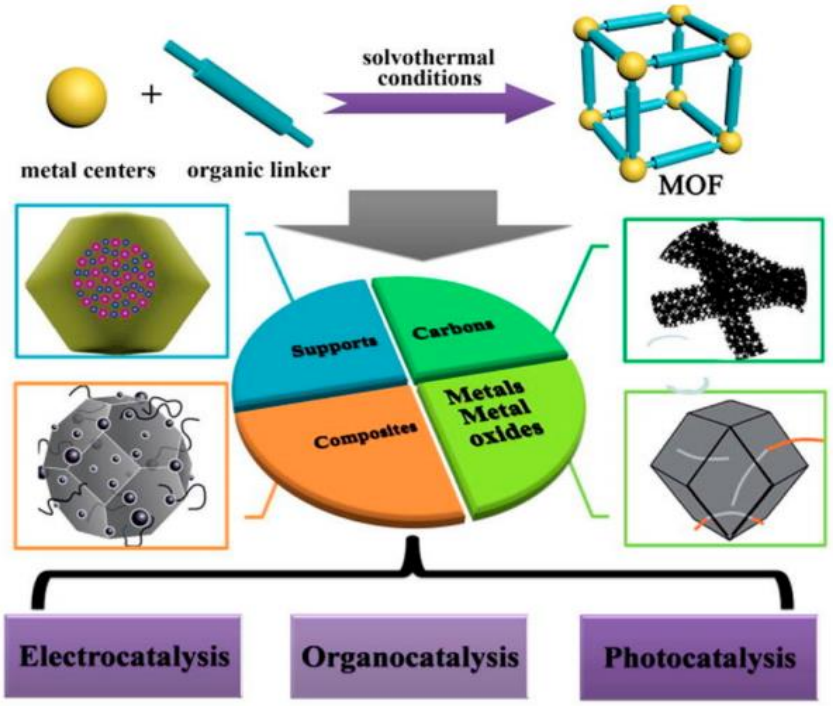

Fig. 7. MOF supports and their derived materials in heterogeneous catalysis. (*Coordination Chemistry Reviews,* 2017, **337**, 80-96).

Hydrolysis reactions that efficiently liberate H_2 are of particular interest in the field of energy production and storage.[109] A porous magnetic cobalt/carbon composite that displayed efficient catalysis for H_2 evolution from $NaBH_4$ was prepared using the cobalt-based ZIF-67 as a precursor (carbonized at 600 °C) by Lin *et al.*[110] The hydrogen source for these types of reactions can vary. Candidates need to have a high hydrogen content, low molecular weight, high solubility in common solvents and be highly stable under ambient conditions. In a number of instances H_2 release from methylamine borane ($CH_3NH_2BH_3$) hydrolysis has been reported.[111] MOF MIL-101 infused with copper nanoparticles catalyzes the reaction to induce 3 mol of H_2 from ammonia-borane hydrolysis. The stoichiometry is shown below:

$$H_3N{\cdot}BH_3 + 4H_2O \rightarrow NH_4{}^{+}B(OH)_4{}^{-} + 3H_2 \quad (1)$$

Despite the advances realized in the fields of gas storage/separation, host-guest chemistry and catalysis, more work needs to be done for these materials to cross over into industry on a large scale. The reasons MOF materials often lose out to non-crystalline materials is cost and stability.[112] The topological structure of a MOF rarely represents a global thermodynamic minimum and their synthesis tends to be an uphill battle against entropy. As a result, they are subject to degradation and the cost in terms of both energy and money to synthesis them must be justified if a MOF is to be applied over a non-crystalline alternative.

1.4 Design Strategies, Crystal Engineering and Reticular Synthesis

Reticular synthesis can be described as "the process of assembling judiciously designed rigid molecular building blocks into predetermined ordered structures".[113] It is this paradigm that is at the heart of modern crystal engineering. The ability to design and piece together molecules to form polymeric network materials is a relatively new concept in field of chemistry but one that has seen comprehensive advancement over the last three decades. Reticular chemistry[114] can be thought of as a subclass of crystal engineering, distinct however from supramolecular chemistry[115] which does not rely on periodic strong bonds throughout the crystal to preserve crystallinity.

For a long time, materials chemistry was conducted predominately by researchers working backwards from the serendipitous discovery of a material. Although some of the most important findings in chemistry have occurred in this manner, an ever-growing library of design strategies as they relate to crystalline framework materials will inevitably prove to invaluable to chemists looking to work in the other direction: inception to design to synthesis of functional materials.

The use of rigid molecular building blocks that retain their structure during the assembly process is key. Not only do the precursor elements and molecules need to be well-defined but the synthetic conditions that govern the kinetic and thermodynamic landscape that these materials interact within needs to be well studied and optimized. Different temperatures, pressures, solvents and reaction times can all influence the resultant topology of MOFs.[116] It is the synthetic conditions in which precursor MOF materials are placed which is still the difficult and unpredictable aspect of forcing particular topological nets. Trial and error in the form of systematic screening of conditions is commonplace and a necessary practice for the realization of new MOFs.[117] However much of the guess work can be removed and the process expedited heavily by a thorough grasp of reticular chemistry as it relates to synthesis and synthetic conditions.

Modern MOF design starts with a designer having a particular framework in mind and then attempting to deconstruct its components. Usually there are two components in a MOF that come together to form a structure. The organic (anionic) building unit can be just about any small molecule functionalized with the appropriate groups to form coordination bonds with cationic species. In the first series of MOFs these molecules were simple, often cyclic molecules such as benzene di-carboxylic acid (BDC). Over the years, in an attempt to make these materials increasingly functional and useful, the complexity and elemental variety of these organic units has vastly expanded. These components are preprepared and modified accordingly prior to coordination and ligand synthesis often comprises the bulk of the chemistry in forming MOFs.

Unlike the ligands, the geometry of the cationic SBU is heavily influenced by the reaction conditions and for the most part it is necessary to establish the exact chemical conditions that will yield a specific SBU *in situ.* The nature of the organic linker, in particular the number of and angle of the bonding groups relative to each other will in turn direct the dimensionality of the framework.

This can be illustrated by the use of what has become one of the most commonly used SBUs: the copper "paddle wheel".[118] Consisting of two copper ions coordinated with four carboxylate groups it is used in a variety of MOFs as the SBU. Depending on the organic linker it is coordinated with, several different dimensionalities result: a truncated cuboctahedron (0D), a linear rod (1D) the square grid (2D), and the NbO network (3D) based on linkage of paddle-wheel clusters by ditopic linkers (see Fig. 8).

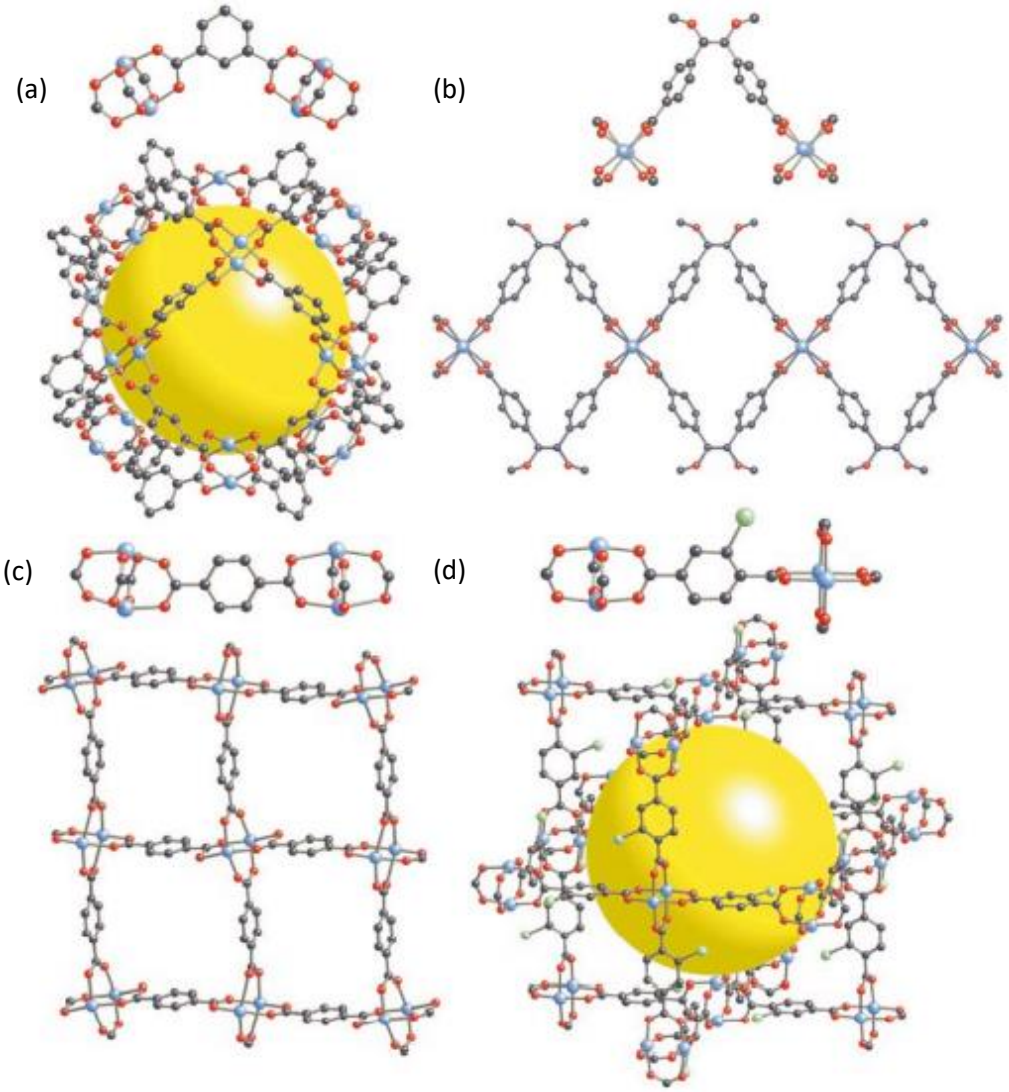

Fig. 8. The control of dimensionality of linked paddle-wheel units by use of precise linker geometry. Shown are fragments of the assembled structures of **(a)** MOP-161**, (b)** MOF-222, **(c)** MOF-242 and **(d)** MOF-10163. C, black; O, red; Br, green; metal, blue. Above each structure, one linker is shown joined to two paddle-wheel units. The yellow spheres are at the centers of large cavities in the structures of MOP-1 and MOF-101. (*Nature,* 2003*,* **423**, 705–714).

As MOF researchers continue to expand the catalogue of new structures, elements that have not traditionally been used as metal nodes are being examined by some researchers. Two potential areas of interest are the lanthanides and the s-block group 1 and 2 metals. Electronically distinct from the transition metals, both lanthanides and s-block metals have the potential to form MOF structures that may be inaccessible with d-block metals. Lanthanide based MOFs (Ln-MOFs)[119] are being explored for

displaying properties that are not often seen in more traditional MOFs such as chirality,[120] magnetism[121] and luminescence.[122] Although Ln-MOFs have been found to have a number of promising potential applications, almost all the lanthanide series of elements are expensive and toxic.[123] In an attempt to obtain novel materials some research groups are turning their attention towards the more ecologically sound s-block metals.[124] It is worth noting that some s-block metals are among the most toxic and rare elements on the planet. What is of interest in the field of green chemistry is a subset of the bio-compatible s-block metals that include sodium, potassium, magnesium and calcium. These elements are easily obtained, inexpensive and non-toxic making them ideal precursor elements for functional materials. Over recent years there has been somewhat of a renaissance of s-block metal organometallic chemistry.[125] In some fields, in particular but not limited to energy storage, many believe elements such as sodium and potassium are poised to play a major role.[126]

1.5 s-block MOFs: Metal Nodes for Ecologically Sound Porous Materials.

The overwhelming majority of MOFs are constructed with metal ions sourced from the transition metal series of elements. Highly utilized elements include copper, zinc, manganese, and zirconium. The use of s-block metal nodes to form coordination polymers is uncommon. Despite not having the d orbitals that are required to facilitate crystal field stabilization (lower energy configuration of the M-L complex), s-block metals have some distinct advantages over the transition metals when employed as metal nodes in MOFs.

In recent decades there has a been a paradigm shift in the direction of chemical research with an ever-increasing awareness and focus on developing principles and practices that are ecologically sound. An expanding list of published research detailing “green” synthetic methods and materials will ensure elements such as sodium and potassium continue to become more of a focus for organo-metallic chemists and researchers concerned with the well-being of the environment. The non-toxic subset of the s-block metals (Na, K, Mg, Ca) are not only biocompatible but are in fact required for many biological processes. Biocompatible MOFs (bioMOFs)[127] have been investigated for their potential use as drug delivery systems,[128] protein encapsulation,[129] release of biologically active gases,[130] bio-imaging,[131] biocatalysts,[132] antimicrobial materials,[133] and prolonged release of drugs.[134] Tuneability of hydrophilicity and acidity allow bioMOFs to be purposely designed to target different biological environments. For example, ‘MOFgen’ a nanotechnology company that was established in 2013, develops MOFs to release antimicrobial NO gas for medicinal purposes.[135]

Table 1. Tabular summary of co-ordination number (C.N.), polyhedra type, dimensionality (D), and synthesis solvents of sodium-based co-ordination networks.

MOF	C.N.	polyhedra	D	synthesis solvents
Na_2(1,4-BDC)	6	2D	3D	water/NaOH/ethanol
Na(HBDC)	6	1D	3D	water/DMF
Na(5-Ura)(H_2O)	6	1D	1D	Water
Na_2(3,5-PDC)(H_2O)4	6	2D	3D	water/NaOH/ethanol
Na(3-PC)	6	1D	3D	Acetonitrile
[Na_2(APZC)2(μH_2O)2(μ3-H_2O)]	6	2D	2D	water/NaOH
Na_2(TTF)(H_2O)3	6	1D	1D	water/acetonitrile

Most bioMOFs are manufactured with low toxicity transition metals such as iron, zinc and zirconium. However, the viability of the alkali and alkaline metals and their ability to form stable, porous, biocompatible framework materials is gaining interest.

When it comes to binding group 1 metals to carboxylate oxygen atoms there are large differences in electronegativity which leads to strong but non-directional ionic bonds. The coordination geometry of these metals and resultant topology are governed largely by location of functional groups and steric bulk of the ligands. Alkali metal ions such as lithium and sodium have a high charge density, making them perfectly suited to forming ionic bonds with a diverse range of negatively charged functional groups or counter ions. Unlike transition metals that tend to cluster and separate the linkers, s-block metals such as sodium and potassium often form 1-D metal oxide secondary building units (SBUs)[136] that run along a single axis. This allows for the close assembling of the organic ligands.

Non-directionality of the orbitals present in s-block metals can be seen as a challenging aspect of their design however frameworks that are flexible and respond to external stimuli have become sought after in particular for applications in sensing.[137] The isotropic ionic interactions that bind s-block MOFs can more easily facilitate structural change and distortion leading to a change in the properties of the materials. An example is a potassium-based MOF reported in 2018, constructed from perylene 3,4,9,10-tetracarboxylate for use as a sensing layer for humidity actuators.[138] Perylene, a known semiconducting a material, when integrated into the MOF, displays a reversible and reproducible response with a change of 5 orders of magnitudes in its impedance at about 40% relative humidity. In this case the researchers were able to

the advantage of subtle structural changes (afforded by the non-direction ionic metal ligand bonds) induced by the absorption of water that altered the distance and orientation of perylene moieties resulting in increased conductivity throughout the framework.

Another advantage of using s-block metals is their low atomic mass. Nowhere has this property been more exploited than in the field of battery technology. An element that a few decades ago no one paid much attention to is now known globally by the non-scientific community. Lithium-ion batteries have become commonplace for use in portable devices and electric vehicles. The realization of a sodium or potassium-based energy storage device is an intense area of research. Coordination polymers have been shown to have the capacity to transport ions, protons and electrical charge, all of which are key for battery and capacitor technology.[139] Charge transport in s-block MOFs is a concept we examine Chapter 2.

"Green chemistry" can be defined as the design of chemical products and processes that reduce or eliminate the use or generation of hazardous substances.[140] A broad perspective that includes the design and production to utilization and disposal of materials and the products made from them needs to be considered. Although chemistry has succeeded in delivering modern society innumerable technological advances it has also bought with it pollution and toxic byproducts that have destroyed ecosystems and the health of some of the world's poorest people. Hopefully in the future we will see both industry and government implement systematic changes in chemical production and manufacturing sectors that ensure sustainable practices are adopted. As researchers whose work may go on to be applied in industry, it is our responsibility to aim towards green chemistry practices. It is also important for schools and universities to ensure the next generation of chemists are aware of the environmental dilemmas facing the planet and encourage students to find solutions. An expanding list of published research detailing "green" synthetic methods and materials will ensure elements such as sodium and potassium continue to become more of a focus for organo-metallic chemists and researchers concerned with the well-being of the environment.

Finally, an area where s-block metals have a distinct advantage over many other metals used in coordination chemistry is their low cost. Often in materials chemistry the expense of scaling up novel materials is prohibitive and means the research may well be published but will never leave the lab. Unlike most metals used elements in co-ordination chemistry, sodium and potassium are some of the most globally abundant and low-cost elements on the planet. Mining and salt production of these metals are performed on huge industrial scales and the cost is orders of magnitude lower than those of most transition metals; an important consideration if a commercially viable solution is an objective.

1.6 Emerging Applications: Charge Transport and Luminescent Materials

In recent years MOF research has branched out to include the examination of applications not entirely reliant on the level of porosity. Charge transport mechanisms present within the crystalline lattice as well as interactions between carefully spaced functional groups are physical characteristics that may well be exploited for the next generation of optoelectronic and energy storage devices.

Most MOFs are insulators and display negligible electrical conductivity (less than 10^{-10} Scm^{-1}).[141] The low electrical conductivity is a direct consequence their composition: voids combined with hard metal ions are connected by organic ligands that bind via hard oxygen or nitrogen atoms. MOFs with intrinsic electrical conductivity have started to emerge as an area of interest for applications that include chemiresistive sensors,[142] batteries,[143] supercapacitors,[144] photovoltaics,[145] thermoelectrics,[146] solar cells[147] and field-effect transistors.[148] In order to engender conductivity in MOFs, several design principles have become evident and continue to evolve resulting in charge mobility, in some co-ordination polymers, approaching that of metallic conductivity (at lowered temperatures).[149]

The charge transport mechanism varies from MOF to MOF. Provided HOMO-LUMO energy levels overlap and there is favourable orbital symmetry, metal to ligand charge transfer (MLCC)[150] can occur. The unpaired electron of square-planar d^9 Cu^{II} centers or the minority-spin electron of high-spin octahedral d^6 Fe^{II} centers contain high energy electrons/holes and are good candidates for MLCC.[151] However the charge pathway in these MOFs can be hindered by differences in energy levels between the metals and ligands. As a result, MLCC is more often used to facilitate catalysis as opposed to creating conductive materials.

In some cases, conductivity is introduced to a system by the integration of guest molecules.[152] An example of this is described in a paper published in 2013 titled “Tunable Electrical Conductivity in Metal-Organic Framework Thin-Film Devices”.[153] In this work, using thin-films of MOF $Cu_3(BTC)_2$ (also known as HKUST-1) infiltrated with redox active, conjugated molecule 7,7,8,8-tetracyanoquinododimethane (TCNQ), researchers achieved an electrical conductivity as high as 7 siemens per meter. Although they were unable to prove it conclusively, they hypothesised the charge transport mechanism involved TCNQ molecules bridging the copper ions forming a molecular wire.

An alternate method to generate charge mobility is via a “though space” or “charge hopping” mechanism.[154] Sufficient spatial overlap between orbitals of appropriate symmetry is required for this process to function effectively. A zinc-based MOF, Zn(TTFTB), (TTFTB = tetrathiafulvalene tetrabenzoate),

with moderate conductivity that employs this method was first reported in 2015.[155] TTF moieties forming stacked 1D helical columns with relatively short S···S interactions between neighbouring TTF molecules running parallel to infinite metal carboxylate SBU (see Fig. 9) result in experimental conductivity measurements of 0.2 $cm^2V^{-1}s^{-1}$. Unlike pure metals there is an anisotropic nature of the electron delocalization in MOFs. This most likely will be a defining property of these materials when they are eventually integrated into the next generation of electronic devices.

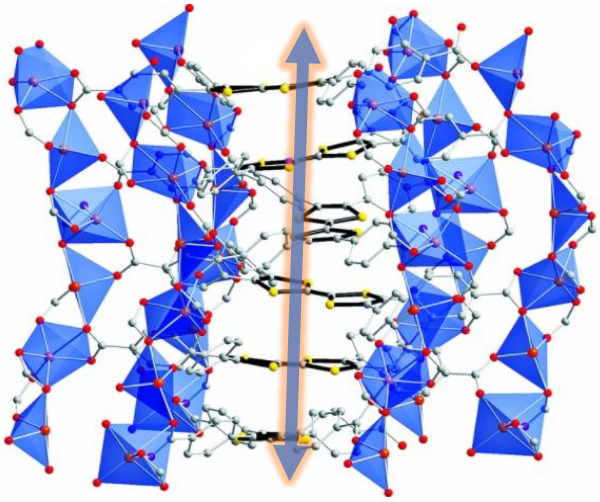

Fig. 9. Side view of a helical TTF stack with a depiction of the shortest intermolecular S···S contact in previously reported conductive MOF $[Zn_2TTFTB(H_2O)_2]\cdot H_2O\cdot 2DMF$ with the theoretical direction of charge mobility highlighted. (*J. Mater. Chem*. A. 2019, **7**, 16571).

In nature, photosynthetic processes rely heavily on the precise positioning of chromophores.[156] Light harvesting molecules and complexes such as chlorophyll and beta carotene are assembled at exact distances and orientations from neighbouring molecules to facilitate the energy transfer processes required to convert electromagnetic radiation into chemical energy.[157]

Recently there have been several MOF studies examining the nature of interchromophoric interactions as a function of their topology.[158, 159, 160] How the spatial arrangement of photo active linkers manifest distinct emission profiles provides an insight into how we can modulate and tune the photo emission of these materials to match specific targets. Planar aromatic molecules functionalized with groups that bond with metal SBUs are employed as the chromophore in these photo emissive MOFs. Porphyrins, naphthalene, anthracene and pyrene are frequently assimilated into porous materials resulting in highly fluorescent materials that often have an anisotropic quality to their absorption and emission.[161]

The overwhelming majority of photo-chemistry experiments are done in solution. Dissolving a chromophore in a solvent allows researchers to perform a variety fluorescence and absorption experiments however the interactions between chromophores are random events governed by diffusion kinetics. Varying the concentration of the chromophores in solution is the only effective tool for promoting of suppressing interchromophoric interactions. A significantly higher level of control over these interactions can be attained within a crystalline framework.

Locking chromophores in position in a solid framework can significantly amplify emission, a process referred to as aggregation induced emission.[162] With less conformation freedom, non-radiative pathways back to the ground state after excitation are limited, enhancing fluorescence considerably.

Made from traditional chromophore tetraphenylethylene (TPE), robust tetravalent zirconium MOF PCN-94, (where PCN stands for "porous coordination network") exhibits remarkably high fluorescence quantum yield in the solid state.

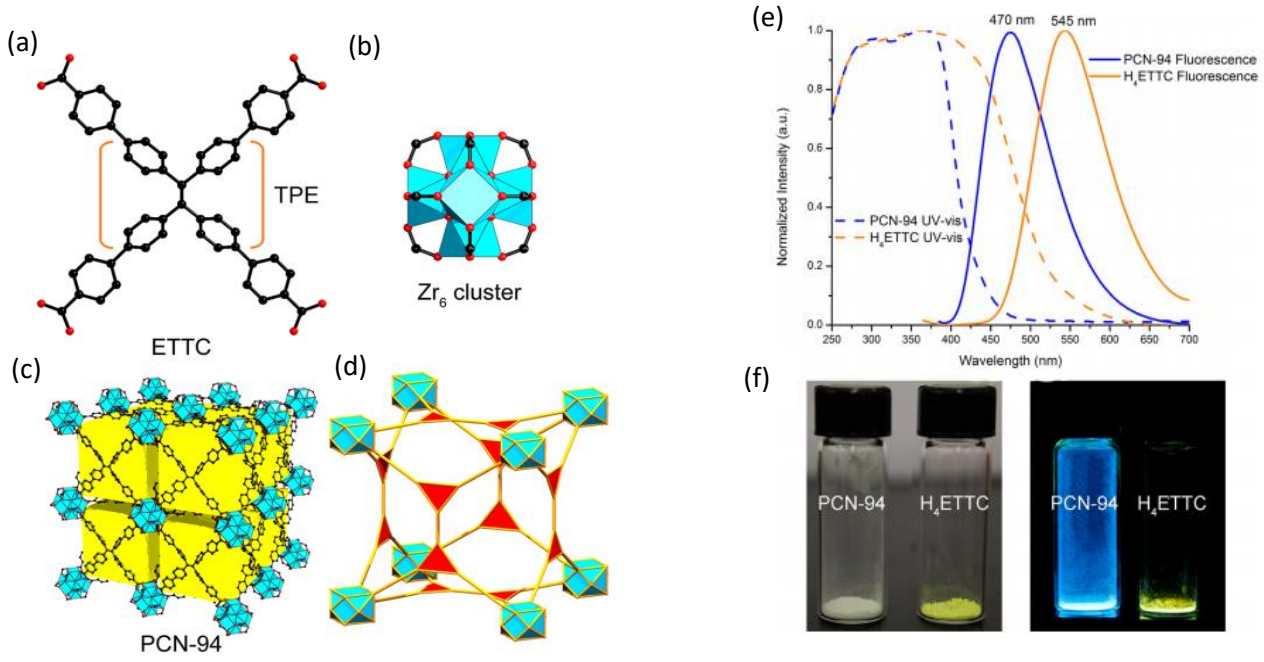

Fig. 10. Crystal structure views of PCN-94 showing: **(a)** ETTC in PCN-94 **(b)** Zr6 cluster; **(c)** PCN-94 framework; **(d)** topological representation of PCN-94. **e)** Solid-state absorption (via diffuse reflectance; dash lines) and emission spectra (solid lines) of PCN-94 (blue) and H4ETTC (orange) at room temperature (RT). Photos of PCN-94 and H4ETTC are shown under **(f)** ambient light and UV light. (*J. Am. Chem. Soc.* 2014, **136**, 8269−8276).

The quantum yield of PCN-94 is as high as unity (99.9 ± 0.5%), which comes from the reduced intra- and intermolecular interactions in addition to the chromophores being locked in a rigid position by the Zr_6 clusters. The quantum yield of the TPE chromophore in the solid state (which is a crystalline HOF made from TPE) is 30%. This is an excellent example of how the emissive properties of materials can be significantly altered, not by synthesizing a new version of the chromophore, but by simply coordinating it within a specific crystalline lattice. In this way luminescent properties can be enhanced, altered and even turned on and off.

One area that has potential to benefit from advances in luminescent framework material is solid state lighting. White light from LEDs is generally produced from either multiple chromophores excited by a common source[164] or more commonly, a blue emitting LED that excites a phosphor material that absorbs in the blue range and emits in the yellow or green part of the visible spectrum.[165] Producing a quality of white light that closely mimics that of natural light produced by the sun has been a challenge.

The porosity of MOFs means their photo/electroluminescent properties can be enhanced or modified further by the introduction of guest molecules. In 2013 a mesoporous blue-emitting MOF synthesized from Cd^{+} and 2,4,6-tris(2,5-dicarboxylphenylamino)-1,3,5-triazine (H_6TATPT) was prepared as host to encapsulate a yellow emitting iridium complex, [Ir(ppy)2(bpy)].[166] The resultant composite MOF emits white light with good color quality (Commission International de l'Eclairage coordinates, color-rendering index and correlated color temperature of (0.31, 0.33), 84.5 and 5409 K, respectively).

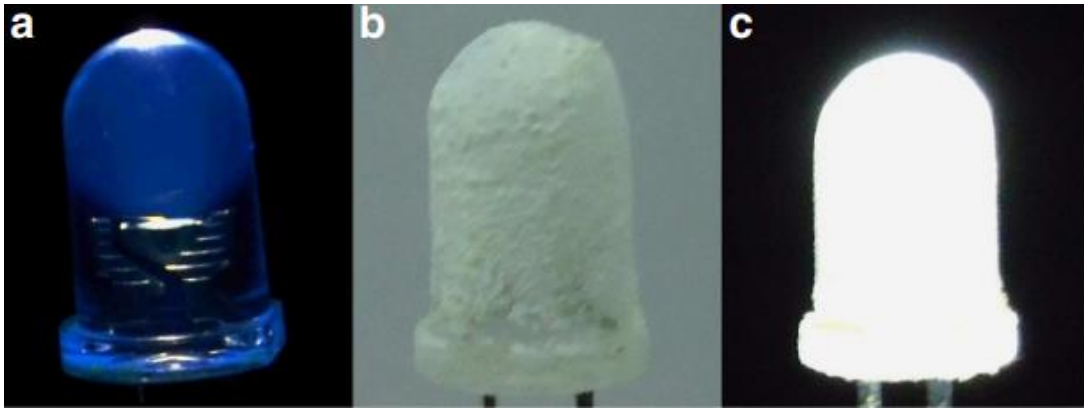

Fig. 11. Photographs of the LEDs**. (a)** An illuminating 3 mm reference ultraviolet LED (turned-on emission has a blue tinge). **(b)** The same LED coated with a thin layer of sample of 3.5 wt% [Ir(ppy)2(bpy)] @ Cd(TATPD) MOF (not turned on). **(c)** The coated LED was turned on and illuminates bright white light. (*Nat Commun*. 2013, **4**, 2717).

A major concern with the materials used for solid state light is that they often involve the use of expensive and/or toxic materials such as mercury, lead, rare earth elements and lanthanide complexes. A challenge for researchers in this field is create materials that have the same emissive properties as the ones mentioned above but are environmentally benign and globally abundant. Due to the increasing demand of rare earth elements in many other high-tech applications, their prices have increased significantly. Since 2001 the prices of yttrium, europium and terbium, the three essential ingredients of phosphors used in general lighting technologies, have increased by 400%, 600%, and 1600% respectively.[167] Now more than ever, rare earth element free phosphor and emissive materials are needed for the next generation of opto-electronic devices and lighting.

1.7 Contextual Statement

The work outlined in this thesis has been designed to explore the viability of using s-block metals to form functional framework materials. We explore design characteristics inherent in these materials that can be used as strategies for future research into s-block based MOFs. Although MOFs were synthesised initially from almost the entire series of group 1 s-block metals we focused our research on sodium and potassium-based frameworks due to their low toxicity and global accessibility. We were also interested in how removing the metal nodes all together would impact the photo emissive properties of the TBAPy chromophore utilized throughout this work.

Chapter 2, presented in the form of a recently published paper, introduces two novel MOFs that use ecologically sound and inexpensive s-block metals to form novel semi-conducting coordination polymers Na(TBAPy)(DMF) and K(TBAPy)(DMF). From a reticular design perspective, the use of the group 1 metals successfully resulted in the formation 1D columnar SBUs that allowed us to stack aromatic pyrene moieties less than 4 Å from each other. This provided significant π orbital overlap and electronic coupling leading to anisotropic charge mobility and enhanced stability. Supported by evidence from computational TD-DFT calculations we were able to fabricate a working device that integrates Na(TBAPy)(DFT) as a semiconducting hole transport layer in a functioning LED device. There are several aspects of this work that we hope will direct material researchers interested in coordination polymers towards the use nontoxic s-block metals such as sodium and potassium to form flexible yet stable MOFs that are responsive to external stimuli.

In Chapter 3, a previously reported material notable for being one of the few permanently porous HOFs reported to date is investigated with a focus on how the close positioning of TBAPy linkers give rise to a

broad emission profile significantly redshifted from both the TBAPy monomer and most other MOFs containing TBAPy. A variety of spectroscopic techniques were utilized to optimize this material with the introduction of a guest molecule. I integrated this composite HOF as a down-conversion phosphor material in a white LED. The result is a functional LED with warm white light production (CIE coordinates 0.29.33) that rivals that of commercially available devices that contain toxic and expensive phosphor materials.

References

1 A. Datta, Z. Zhong and S. Motakef, *Sci. Rep.*, 2020, **10**, 1–10.

2 F. Oviedo, Z. Ren, S. Sun, C. Settens, Z. Liu, N. T. P. Hartono, S. Ramasamy, B. L. DeCost, S. I. P. Tian, G. Romano, A. Gilad Kusne and T. Buonassisi, *npj Comput. Mater.*, 2019, **5**, 1–9.

3 T. Wittmann, C. B. L. Tschense, L. Zappe, C. Koschnick, R. Siegel, R. Stäglich, B. V. Lotsch and J. Senker, *J. Mater. Chem. A*, 2019, **7**, 10379–10388.

4 V. Pascanu, G. González Miera, A. K. Inge and B. Martín-Matute, *J. Am. Chem. Soc.*, 2019, **141**, 7223–7234.

5 X. Cui, W. Li, P. Ryabchuk, K. Junge and M. Beller, *Nat. Catal.*, 2018, **1**, 385–397.

6 Z. Lei, Y. Xue, W. Chen, W. Qiu, Y. Zhang, S. Horike and L. Tang, *Adv. Energy Mater.*, 2018, **8**, 1–31.

7 T. Wang, L. Gao, J. Hou, S. J. A. Herou, J. T. Griffiths, W. Li, J. Dong, S. Gao, M. M. Titirici, R. V. Kumar, A. K. Cheetham, X. Bao, Q. Fu and S. K. Smoukov, *Nat. Commun.*, 2019, **10**, 1–9.

8 Y. Wang and C. Wöll, *Catal. Letters*, 2018, **148**, 2201–2222.

9 P. Railey, Y. Song, T. Liu and Y. Li, *Mater. Res. Bull.*, 2017, **96**, 385–394.

10 Z. Zhou, X. Xing, C. Tian, W. Wei, D. Li, F. Hu and S. Du, *Sci. Rep.*, 2018, **8**, 1–8.

11 A. Bavykina, N. Kolobov, I. S. Khan, J. A. Bau, A. Ramirez and J. Gascon, *Chem. Rev.*, 2020, **120**, 8468–8535.

12 J. Grand, H. Awala and S. Mintova, *CrystEngComm*, 2016, **18**, 650–664.

13 M. Mańko, R. Chal, P. Trens, D. Minoux, C. Gérardin and W. Makowski, *Microporous Mesoporous Mater.*, 2013, **170**, 243–250.

14 P. J. Bereciartua, Á. Cantín, A. Corma, J. L. Jordá, M. Palomino, F. Rey, S. Valencia, E. W. Corcoran, P. Kortunov, P. I. Ravikovitch, A. Burton, C. Yoon, Y. Wang, C. Paur, J. Guzman, A. R. Bishop and G. L. Casty, *Science (80-.).*, 2017, **358**, 1068–1071.

15 E. M. Gallego, M. T. Portilla, C. Paris, A. León-Escamilla, M. Boronat, M. Moliner and A. Corma, *Science (80-.).*, 2017, **355**, 1051–1054.

16 C. S. Cundy and P. A. Cox, *Chem. Rev.*, 2003, **103**, 663–701.

17 R. M. Milton, *Molecular Sieve Science and Technology*, 1989, 1–10.

18 D. W. Breck, *Journ of Chem Ed,* 1964, **41**, 678.

19 X. Zhang, Z. Chen, X. Liu, S. L. Hanna, X. Wang, R. Taheri-Ledari, A. Maleki, P. Li and O. K. Farha, *Chem. Soc. Rev.*, 2020, **49**, 7406–7427.

20 S. R. Batten, N. R. Champness, X. M. Chen, J. Garcia-Martinez, S. Kitagawa, L. Öhrström, M. O'Keeffe, M. P. Suh and J. Reedijk, *CrystEngComm*, 2012, **14**, 3001–3004.

21 1999, **402**, 276–279.

22 A. K. Crane, B. O. Patrick and M. J. MacLachlan, *Dalt. Trans.*, 2013, **42**, 8026–8033.

23 Y. R. Lee, J. Kim and W. S. Ahn, *Korean J. Chem. Eng.*, 2013, **30**, 1667–1680.

24 V. M. V. and G. Nageswaran, *J. Electrochem. Soc.*, 2020, **167**, 155527.

25 D. Chen, J. Zhao, P. Zhang and S. Dai, *Polyhedron*, 2019, **162**, 59–64.

26 C. Vaitsis, G. Sourkouni and C. Argirusis, *Ultrason. Sonochem.*, 2019, **52**, 106–119.

27 J. Klinowski, F. A. Almeida Paz, P. Silva and J. Rocha, *Dalt. Trans.*, 2011, **40**, 321–330.

28 Y. Lin, H. Wan, D. Wu, G. Chen, N. Zhang, X. Liu, J. Li, Y. Cao, G. Qiu and R. Ma, *J. Am. Chem. Soc.*, 2020, **142**, 7317–7321.

29 G. Priyadarshana, N. Kottegoda, A. Senaratne, A. De Alwis and V. Karunaratne, *J. Nanomater.*, , DOI:10.1155/2015/317312.

30 G. Maurin, C. Serre, A. Cooper and G. Férey, *Chem. Soc. Rev.*, 2017, **46**, 3104–3107.

31 H. Li, K. Wang, Y. Sun, C. T. Lollar, J. Li and H. C. Zhou, *Mater. Today*, 2018, **21**, 108–121.

32 L. Zhu, X. Q. Liu, H. L. Jiang and L. B. Sun, *Chem. Rev.*, 2017, **117**, 8129–8176.

33 D. Saha and Z. Bao, *Environ. Sci. Technol.*, 2010, **44**, 1820–1826.

34 Z. Jin, H. Y. Zhao, X. J. Zhao, Q. R. Fang, J. R. Long and G. S. Zhu, *Chem. Commun.*, 2010, **46**, 8612–8614.

35 W. Xuan, C. Zhu, Y. Liu and Y. Cui, *Chem. Soc. Rev.*, 2012, **41**, 1677–1695.

36 Y. Zhang, S. Yu, G. Lou, Y. Shen, H. Chen, Z. Shen, S. Zhao, J. Zhang, S. Chai and Q. Zou, *J. Mater. Sci.*, 2017, **52**, 11201–11228.

37 K. A. Cychosz and M. Thommes, *Engineering*, 2018, **4**, 559–566.

38 K. Tan, S. Zuluaga, E. Fuentes, E. C. Mattson, J. F. Veyan, H. Wang, J. Li, T. Thonhauser and Y. J. Chabal, *Nat. Commun.*, 2016, **7**, 1–8.

39 C. Buttersack, *Phys. Chem. Chem. Phys.*, 2019, **21**, 5614–5626.

40 S. Rahman, A. Arami-Niya, X. Yang, G. Xiao, G. (Kevin) Li and E. F. May, *Commun. Chem.*, 2020, **3**, 3–8.

41 H. Jasuja, Y. G. Huang and K. S. Walton, *Langmuir*, 2012, **28**, 16874–16880.

42 B. Wang, R. B. Lin, Z. Zhang, S. Xiang and B. Chen, *J. Am. Chem. Soc.*, 2020, **142**, 14399–14416.

43 P. Li, M. R. Ryder and J. F. Stoddart, *Accounts Mater. Res.*, 2020, **1**, 77–87.

44 M. Martín-Arroyo, J. Castells-Gil, N. Bilbao, N. Almora-Barrios, C. Martí-Gastaldo and D. González-Rodríguez, *Chem. Commun.*, 2021, **57**, 1659–1662.

45 B. Wang, X. L. Lv, J. Lv, L. Ma, R. B. Lin, H. Cui, J. Zhang, Z. Zhang, S. Xiang and B. Chen, *Chem. Commun.*, 2019, **56**, 66–69.

46 N. Li, J. Xu, R. Feng, T. L. Hu and X. H. Bu, *Chem. Commun.*, 2016, **52**, 8501–8513.

47 X. Z. Luo, X. J. Jia, J. H. Deng, J. L. Zhong, H. J. Liu, K. J. Wang and D. C. Zhong, *J. Am. Chem. Soc.*, 2013, **135**, 11684–11687.

48 K. Ma, P. Li, J. H. Xin, Y. Chen, Z. Chen, S. Goswami, X. Liu, S. Kato, H. Chen, X. Zhang, J. Bai, M. C. Wasson, R. R. Maldonado, R. Q. Snurr and O. K. Farha, *Cell Reports Phys. Sci.*, 2020, **1**, 100024.

49 Z. Ju, G. Liu, Y. S. Chen, D. Yuan and B. Chen, *Chem. - A Eur. J.*, 2017, **23**, 4774–4777.

50 W. Gong, D. Chu, H. Jiang, X. Chen, Y. Cui and Y. Liu, *Nat. Commun.*, 2019, **10**, 1–9.

51 J. Luo, J. W. Wang, J. H. Zhang, S. Lai and D. C. Zhong, *CrystEngComm*, 2018, **20**, 5884–5898.

52 Y. Zou, X. Ji, J. Cai, T. Yuan, D. J. Stanton, Y. H. Lin, M. Naraghi and L. Fang, *Chem*, 2017, **2**, 139–152.

53 J. fei Feng, T. F. Liu and R. Cao, *Angew. Chemie - Int. Ed.*, 2020, **59**, 22392–22396.

54 F. Hu, C. Liu, M. Wu, J. Pang, F. Jiang, D. Yuan and M. Hong, *Angew. Chemie - Int. Ed.*, 2017, **56**, 2101–2104.

55 Q. Yin, P. Zhao, R. J. Sa, G. C. Chen, L. Jian, T. F. Liu and R. Cao, *Angew. Chemie - Int. Ed.*, 2018, **57**, 7691–7696.

56 S. B. Alahakoon, S. D. Diwakara, C. M. Thompson and R. A. Smaldone, *Chem. Soc. Rev.*, 2020, **49**, 1344–1356.

57 M. Bosch, M. Zhang and H.-C. Zhou, *Adv. Chem.*, 2014, **2014**, 1–8.

58 A. Karmakar, R. Illathvalappil, B. Anothumakkool, A. Sen, P. Samanta, A. V. Desai, S. Kurungot and S. K. Ghosh, *Angew. Chemie - Int. Ed.*, 2016, **55**, 10667–10671.

59 Q. Huang, W. Li, Z. Mao, L. Qu, Y. Li, H. Zhang, T. Yu, Z. Yang, J. Zhao, Y. Zhang, M. P. Aldred and Z. Chi, *Nat. Commun.*, 2019, **10**, 1–8.

60 H. C. J. Zhou and S. Kitagawa, *Chem. Soc. Rev.*, 2014, **43**, 5415–5418.

61 H. Furukawa, K. E. Cordova, M. O'Keeffe and O. M. Yaghi, *Science (80-.).*, , DOI:10.1126/science.1230444.

62 J. L. C. Rowsell and O. M. Yaghi, *Microporous Mesoporous Mater.*, 2004, **73**, 3–14.

63 Y. He, W. Zhou, G. Qian and B. Chen, *Chem. Soc. Rev.*, 2014, **43**, 5657–5678.

64 A. de Oliveira, G. F. de Lima and H. A. De Abreu, *Chem. Phys. Lett.*, 2018, **691**, 283–290.

65 H. Li, L. Li, R.-B. Lin, W. Zhou, Z. Zhang, S. Xiang and B. Chen, *EnergyChem*, 2019, **1**, 100006.

66 J. R. Li, R. J. Kuppler and H. C. Zhou, *Chem. Soc. Rev.*, 2009, **38**, 1477–1504.

67 C. A. Trickett, A. Helal, B. A. Al-Maythalony, Z. H. Yamani, K. E. Cordova and O. M. Yaghi, *Nat. Rev. Mater.*, 2017, **2**, 1–16.

68 J. A. Mason, K. Sumida, Z. R. Herm, R. Krishna and J. R. Long, *Energy Environ. Sci.*, 2011, **4**, 3030–3040.

69 Z. Li, P. Liu, C. Ou and X. Dong, *ACS Sustain. Chem. Eng.*, 2020, **8**, 15378–15404.

70 S. S. Wang, W. Bin Yang, M. Yang, X. Y. Wu, W. Wu, S. X. Wang, L. Lin and C. Z. Lu, *Chem. Commun.*, 2020, **56**, 2503–2506.

71 M. F. J. Mabesoone, A. R. A. Palmans and E. W. Meijer, *J. Am. Chem. Soc.*, 2020, **142**, 19781–19798.

72 E. Raee, Y. Yang and T. Liu, *Giant*, 2021, **5**, 100050.

73 C. Bao, M. Ma, F. Meng, Q. Lin and L. Zhu, *New J. Chem.*, 2015, **39**, 6297–6302.

74 L. H. Xie, M. M. Xu, X. M. Liu, M. J. Zhao and J. R. Li, *Adv. Sci.*, , DOI:10.1002/advs.201901758.

75 A. K. Chaudhari, S. Mukherjee, S. S. Nagarkar, B. Joarder and S. K. Ghosh, *CrystEngComm*, 2013, **15**, 9465–9471.

76 C. Volkringer, I. Mihalcea, J. F. Vigier, A. Beaurain, M. Visseaux and T. Loiseau, *Inorg. Chem.*, 2011, **50**, 11865–11867.

77 Y. Liu, Y. Shen, W. Zhang, J. Weng, M. Zhao, T. Zhu, Y. R. Chi, Y. Yang, H. Zhang and F. Huo, *Chem. Commun.*, 2019, **55**, 11770–11773.

78 S. Horike, D. Umeyama and S. Kitagawa, *Acc. Chem. Res.*, 2013, **46**, 2376–2384.

79 T. A. Goetjen, J. Liu, Y. Wu, J. Sui, X. Zhang, J. T. Hupp and O. K. Farha, *Chem. Commun.*, 2020, **56**, 10409–10418.

80 J. Zheng, J. Ye, M. A. Ortuño, J. L. Fulton, O. Y. Gutiérrez, D. M. Camaioni, R. K. Motkuri, Z. Li, T. E. Webber, B. L. Mehdi, N. D. Browning, R. L. Penn, O. K. Farha, J. T. Hupp, D. G. Truhlar, C. J. Cramer and J. A. Lercher, *J. Am. Chem. Soc.*, 2019, **141**, 9292–9304.

81 P. Wu, M. Jiang, Y. Li, Y. Liu and J. Wang, *J. Mater. Chem. A*, 2017, **5**, 7833–7838.

82 Y. H. Budnikova, *Dalt. Trans.*, 2020, **49**, 12483–12502.

83 F. N. Al-Rowaili, A. Jamal, M. S. Ba Shammakh and A. Rana, *ACS Sustain. Chem. Eng.*, 2018, **6**, 15895–15914.

84 Z. Ding, S. Wang, X. Chang, D. H. Wang and T. Zhang, *RSC Adv.*, 2020, **10**, 26246–26255.

85 X. Li, B. Wang, Y. Cao, S. Zhao, H. Wang, X. Feng, J. Zhou and X. Ma, *ACS Sustain. Chem. Eng.*, 2019, **7**, 4548–4563.

86 M. Fujita, S. Washizu, K. Ogura and Y. J. Kwon, *J. Am. Chem. Soc.*, 1994, **116**, 1151–1152.

87 S. Zuluaga, E. M. A. Fuentes-Fernandez, K. Tan, F. Xu, J. Li, Y. J. Chabal and T. Thonhauser, *J. Mater. Chem. A*, 2016, **4**, 5176–5183.

88 Y. Pan, Y. Liu, G. Zeng, L. Zhao and Z. Lai, *Chem. Commun.*, 2011, **47**, 2071–2073.

89 H. F. Yao, Y. Yang, H. Liu, F. G. Xi and E. Q. Gao, *J. Mol. Catal. A Chem.*, 2014, **394**, 57–65.

90 Y. Zhang, H. Chen, Y. Pan, X. Zeng, X. Jiang, Z. Long and X. Hou, *Chem. Commun.*, 2019, **55**, 13959–13962.

91 E. S. Larrea, R. Fernández de Luis, A. Fidalgo-Marijuan, E. M. Maya, M. Iglesias and M. I. Arriortua, *CrystEngComm*, 2020, **22**, 2904–2913.

92 Z. Wang, M. Babucci, Y. Zhang, Y. Wen, L. Peng, B. Yang, B. C. Gates and D. Yang, *ACS Appl. Mater. Interfaces*, 2020, **12**, 53537–53546.

93 E. Niknam, F. Panahi, F. Daneshgar, F. Bahrami and A. Khalafi-Nezhad, *ACS Omega*, 2018, **3**, 17135–17144.

94 J. D. Xiao and H. L. Jiang, *Acc. Chem. Res.*, , DOI:10.1021/acs.accounts.8b00521.

95 S. Jin, *ACS Energy Lett.*, 2019, **4**, 1443–1445.

96 M. Ranocchiari and J. A. Van Bokhoven, *Phys. Chem. Chem. Phys.*, 2011, **13**, 6388–6396.

97 A. Li, B. Qian, M. Zhong, Y. Liu, Z. Chang and X. H. Bu, *Mater. Chem. Front.*, 2019, **3**, 1398–1405.

98 X. Yang, H. Mi, X. Ren, P. Zhang and Y. Li, *Nanoscale Res. Lett.*, 2020, **15**, 4–15.

99 L. Liu and A. Corma, *Chem. Rev.*, 2018, **118**, 4981–5079.

100 J. Tang, J. R. Durrant and D. R. Klug, *J. Am. Chem. Soc.*, 2008, **130**, 13885–13891.

101 G. V. Loukova, W. Huhn, V. P. Vasiliev and V. A. Smirnov, *J. Phys. Chem. A*, 2007, **111**, 4117–4121.

102 S. Kampouri, T. N. Nguyen, C. P. Ireland, B. Valizadeh, F. M. Ebrahim, G. Capano, D. Ongari, A. Mace, N. Guijarro, K. Sivula, A. Sienkiewicz, L. Forró, B. Smit and K. C. Stylianou, *J. Mater. Chem. A*, 2018, **6**, 2476–2481.

103 H. F. Wang, L. Chen, H. Pang, S. Kaskel and Q. Xu, *Chem. Soc. Rev.*, 2020, **49**, 1414–1448.

104 K. Singh, J. D. J. Guillen Campos, F. Dinic, Z. Hao, T. Yuan and O. Voznyy, *ACS Mater. Lett.*, 2020, **2**, 798–800.

105 H. L. Tang, X. J. Sun and F. M. Zhang, *Dalt. Trans.*, 2020, **49**, 12136–12144.

106 H. Zhong, M. Ghorbani-Asl, K. H. Ly, J. Zhang, J. Ge, M. Wang, Z. Liao, D. Makarov, E. Zschech, E. Brunner, I. M. Weidinger, J. Zhang, A. V. Krasheninnikov, S. Kaskel, R. Dong and X. Feng, *Nat. Commun.*, 2020, **11**, 1–10.

107 S. Sui, X. Wang, X. Zhou, Y. Su, S. Riffat and C. jun Liu, *J. Mater. Chem. A*, 2017, **5**, 1808–1825.

108 C. Sealy, *Mater. Today*, 2008, **11**, 65–68.

109 C. Wang, J. Tuninetti, Z. Wang, C. Zhang, R. Ciganda, L. Salmon, S. Moya, J. Ruiz and D. Astruc, *J. Am. Chem. Soc.*, 2017, **139**, 11610–11615.

110 K. Y. A. Lin and H. A. Chang, *Chem. Eng. J.*, 2016, **296**, 243–251.

111 I. B. Baguc, I. E. Ertas, M. Yurderi, A. Bulut, M. Zahmakiran and M. Kaya, *Inorganica Chim. Acta*, 2018, **483**, 431–439.

112 A. U. Czaja, N. Trukhan and U. Müller, *Chem. Soc. Rev.*, 2009, **38**, 1284–1293.

113 O. M. Yaghi, M. O'Keeffe, N. W. Ockwig, H. K. Chae, M. Eddaoudi and J. Kim, *Nature*, 2003, **423**, 705–714.

114 O. M. Yaghi, *ACS Cent. Sci.*, 2019, **5**, 1295–1300.

115 S. I. Stupp and L. C. Palmer, *Chem. Mater.*, 2014, **26**, 507–518.

116 P. A. Julien, C. Mottillo and T. Friščić, *Green Chem.*, 2017, **19**, 2729–2747.

117 E. J. Garcia, D. Bahamon and L. F. Vega, *ACS Sustain. Chem. Eng.*, , DOI:10.1021/acssuschemeng.0c07797.

118 Y. Chen, B. Wang, X. Wang, L. H. Xie, J. Li, Y. Xie and J. R. Li, *ACS Appl. Mater. Interfaces*, 2017, **9**, 27027–27035.

119 C. Pagis, M. Ferbinteanu, G. Rothenberg and S. Tanase, *ACS Catal.*, 2016, **6**, 6063–6072.

120 D. Bejan, L. G. Bahrin, S. Shova, N. L. Marangoci, Ü. Kökcam-Demir, V. Lozan and C. Janiak, *Molecules*, , DOI:10.3390/molecules25133055.

121 C. Zhang, X. Ma, P. Cen, X. Jin, J. Yang, Y. Q. Zhang, J. Ferrando-Soria, E. Pardo and X. Liu, *Dalt. Trans.*, 2020, **49**, 14123–14132.

122 J. Rocha, L. D. Carlos, F. A. A. Paz and D. Ananias, *Chem. Soc. Rev.*, 2011, **40**, 926–940.

123 P. Tai, Q. Zhao, D. Su, P. Li and F. Stagnitti, *Chemosphere*, 2010, **80**, 1031–1035.

124 M. A. Alnaqbi, A. Alzamly, S. H. Ahmed, M. Bakiro, J. Kegere and H. L. Nguyen, *J. Mater. Chem. A*, 2021, **9**, 3828–3854.

125 S. Krieck and M. Westerhausen, *Inorganics*, 2017, **5**, 8–11.

126 B. John, V. Anoopkumar and T. D. Mercy, *ACS Appl. Energy Mater.*, 2020, **3**, 9478–9492.

127 H. Cai, Y. L. Huang and D. Li, *Coord. Chem. Rev.*, 2019, **378**, 207–221.

128 M. Cai, G. Chen, L. Qin, C. Qu, X. Dong, J. Ni and X. Yin, *Pharmaceutics*, , DOI:10.3390/pharmaceutics12030232.

129 T. H. Wei, S. H. Wu, Y. Da Huang, W. S. Lo, B. P. Williams, S. Y. Chen, H. C. Yang, Y. S. Hsu, Z. Y. Lin, X. H. Chen, P. E. Kuo, L. Y. Chou, C. K. Tsung and F. K. Shieh, *Nat. Commun.*, 2019, **10**, 1–8.

130 A. C. McKinlay, P. K. Allan, C. L. Renouf, M. J. Duncan, P. S. Wheatley, S. J. Warrender, D. Dawson, S. E. Ashbrook, B. Gil, B. Marszalek, T. Düren, J. J. Williams, C. Charrier, D. K. Mercer, S. J. Teat and R. E. Morris, *APL Mater.*, , DOI:10.1063/1.4903290.

131 H. S. Wang, Y. H. Wang and Y. Ding, *Nanoscale Adv.*, 2020, **2**, 3788–3797.

132 M. Bilal, M. Adeel, T. Rasheed and H. M. N. Iqbal, *J. Mater. Res. Technol.*, 2019, **8**, 2359–2371.

133 S. Rojas, T. Devic and P. Horcajada, *J. Mater. Chem. B*, 2017, **5**, 2560–2573.

134 C. Orellana-Tavra, R. J. Marshall, E. F. Baxter, I. A. Lázaro, A. Tao, A. K. Cheetham, R. S. Forgan and D. Fairen-Jimenez, *J. Mater. Chem. B*, 2016, **4**, 7697–7707.

135 N. J. Hinks, A. C. McKinlay, B. Xiao, P. S. Wheatley and R. E. Morris, *Microporous Mesoporous Mater.*, 2010, **129**, 330–334.

136 D. Banerjee and J. B. Parise, *Cryst. Growth Des.*, 2011, **11**, 4704–4720.

137 L. T. Zhang, Y. Zhou and S. T. Han, *Angew. Chemie - Int. Ed.*, 2020, 2–23.

138 J. M. Seco, E. San Sebastián, J. Cepeda, B. Biel, A. Salinas-Castillo, B. Fernández, D. P. Morales, M. Bobinger, S. Gómez-Ruiz, F. C. Loghin, A. Rivadeneyra and A. Rodríguez-Diéguez, *Sci. Rep.*, 2018, **8**, 1–10.

139 G. Xu, P. Nie, H. Dou, B. Ding, L. Li and X. Zhang, *Mater. Today*, 2017, **20**, 191–209.

140 H. C. Erythropel, J. B. Zimmerman, T. M. De Winter, L. Petitjean, F. Melnikov, C. H. Lam, A. W. Lounsbury, K. E. Mellor, N. Z. Janković, Q. Tu, L. N. Pincus, M. M. Falinski, W. Shi, P. Coish, D. L. Plata and P. T. Anastas, *Green Chem.*, 2018, **20**, 1929–1961.

141 L. S. Xie, G. Skorupskii and M. Dincă, *Chem. Rev.*, 2020, **120**, 8536–8580.

142 W.-T. Koo, J.-S. Jang and I.-D. Kim, *Chem*, 2019, **5**, 1938–1963.

143 J. P. Zhu, X. H. Wang and X. X. Zuo, *R. Soc. Open Sci.*, , DOI:10.1098/rsos.190634.

144 Y. Jiao, J. Pei, D. Chen, C. Yan, Y. Hu, Q. Zhang and G. Chen, *J. Mater. Chem. A*, 2017, **5**, 1094–1102.

145 C. C. Chueh, C. I. Chen, Y. A. Su, H. Konnerth, Y. J. Gu, C. W. Kung and K. C. W. Wu, *J. Mater. Chem. A*, 2019, **7**, 17079–17095.

146 Y. He, C. D. Spataru, F. Léonard, R. E. Jones, M. E. Foster, M. D. Allendorf and A. Alec Talin, *Phys. Chem. Chem. Phys.*, 2017, **19**, 19461–19467.

147 S. Wu, Z. Li, M. Q. Li, Y. Diao, F. Lin, T. Liu, J. Zhang, P. Tieu, W. Gao, F. Qi, X. Pan, Z. Xu, Z. Zhu and A. K. Y. Jen, *Nat. Nanotechnol.*, 2020, **15**, 934–940.

148 G. Wu, J. Huang, Y. Zang, J. He and G. Xu, *J. Am. Chem. Soc.*, 2017, **139**, 1360–1363.

149 A. J. Clough, N. M. Orchanian, J. M. Skelton, A. J. Neer, S. A. Howard, C. A. Downes, L. F. J. Piper, A. Walsh, B. C. Melot and S. C. Marinescu, *J. Am. Chem. Soc.*, 2019, **141**, 16323–16330.

150 M. Gutierrez, B. Cohen, F. Sánchez and A. Douhal, *Phys. Chem. Chem. Phys.*, 2016, **18**, 27761–27774.

151 J. Cherusseri, D. Pandey, K. Sambath Kumar, J. Thomas and L. Zhai, *Nanoscale*, 2020, **12**, 17649–17662.

152 M. Ko, L. Mendecki and K. A. Mirica, *Chem. Commun.*, 2018, **54**, 7873–7891.

153 A. A. Talin, A. Centrone, A. C. Ford, M. E. Foster, V. Stavila, P. Haney, R. A. Kinney, V. Szalai, F. El Gabaly, H. P. Yoon, F. Léonard and M. D. Allendorf, *Science (80-.).*, 2014, **343**, 66–69.

154 C. Hua, P. W. Doheny, B. Ding, B. Chan, M. Yu, C. J. Kepert and D. M. D'Alessandro, *J. Am. Chem. Soc.*, 2018, **140**, 6622–6630.

155 L. Sun, S. S. Park, D. Sheberla and M. Dincă, *J. Am. Chem. Soc.*, 2016, **138**, 14772–14782.

156 F. Fassioli, R. Dinshaw, P. C. Arpin and G. D. Scholes, *J. R. Soc. Interface*, , DOI:10.1098/rsif.2013.0901.

157 T. Zhang and W. Lin, *Chem. Soc. Rev.*, 2014, **43**, 5982–5993.

158 S. Patwardhan and G. C. Schatz, *J. Phys. Chem. C*, 2015, **119**, 24238–24247.

159 M. Gutiérrez, F. Sánchez and A. Douhal, *Chem. - A Eur. J.*, 2016, **22**, 13072–13082.

160 W. M. Liao, J. H. Zhang, S. Y. Yin, H. Lin, X. Zhang, J. Wang, H. P. Wang, K. Wu, Z. Wang, Y. N. Fan, M. Pan and C. Y. Su, *Nat. Commun.*, , DOI:10.1038/s41467-018-04833-1.

161 R. Haldar, M. Jakoby, A. Mazel, Q. Zhang, A. Welle, T. Mohamed, P. Krolla, W. Wenzel, S. Diring, F. Odobel, B. S. Richards, I. A. Howard and C. Wöll, *Nat. Commun.*, 2018, **9**, 1–8.

162 J. Dong, P. Shen, S. Ying, Z. J. Li, Y. Di Yuan, Y. Wang, X. Zheng, S. B. Peh, H. Yuan, G. Liu, Y. Cheng, Y. Pan, L. Shi, J. Zhang, D. Yuan, B. Liu, Z. Zhao, B. Z. Tang and D. Zhao, *Chem. Mater.*, 2020, **32**, 6706–6720.

163 Z. Wei, Z. Y. Gu, R. K. Arvapally, Y. P. Chen, R. N. McDougald, J. F. Ivy, A. A. Yakovenko, D. Feng, M. A. Omary and H. C. Zhou, *J. Am. Chem. Soc.*, 2014, **136**, 8269–8276.

164 M. L. Meretska, G. Vissenberg, A. Lagendijk, W. L. Ijzerman and W. L. Vos, *ACS Photonics*, 2019, **6**, 3070–3075.

165 W. P. Lustig, Z. Shen, S. J. Teat, N. Javed, E. Velasco, D. M. O'Carroll and J. Li, *Chem. Sci.*, 2020, **11**, 1814–1824.

166 C. Y. Sun, X. L. Wang, X. Zhang, C. Qin, P. Li, Z. M. Su, D. X. Zhu, G. G. Shan, K. Z. Shao, H. Wu and J. Li, *Nat. Commun.*, 2013, **4**, 1–8.

167 V. Balaram, *Geosci. Front.*, 2019, **10**, 1285–1303.

Chapter 2. Structural modulation of the photophysical and electronic properties of pyrene-based 3D metal–organic frameworks derived from s-block metals

Christopher N. Coleman, Patrick C. Tapping, Michael T. Huxley, Tak W. Kee, David M. Huang*, Christian J. Doonan* and Christopher J. Sumby*

Department of Chemistry and the Centre for Advanced Nanomaterials, School of Physical Sciences, The University of Adelaide, Adelaide, SA 5005, Australia

Journal Reference: *CrystEngComm*, 2021, **23**, 82-90. DOI:10.1039/d0ce01505a.

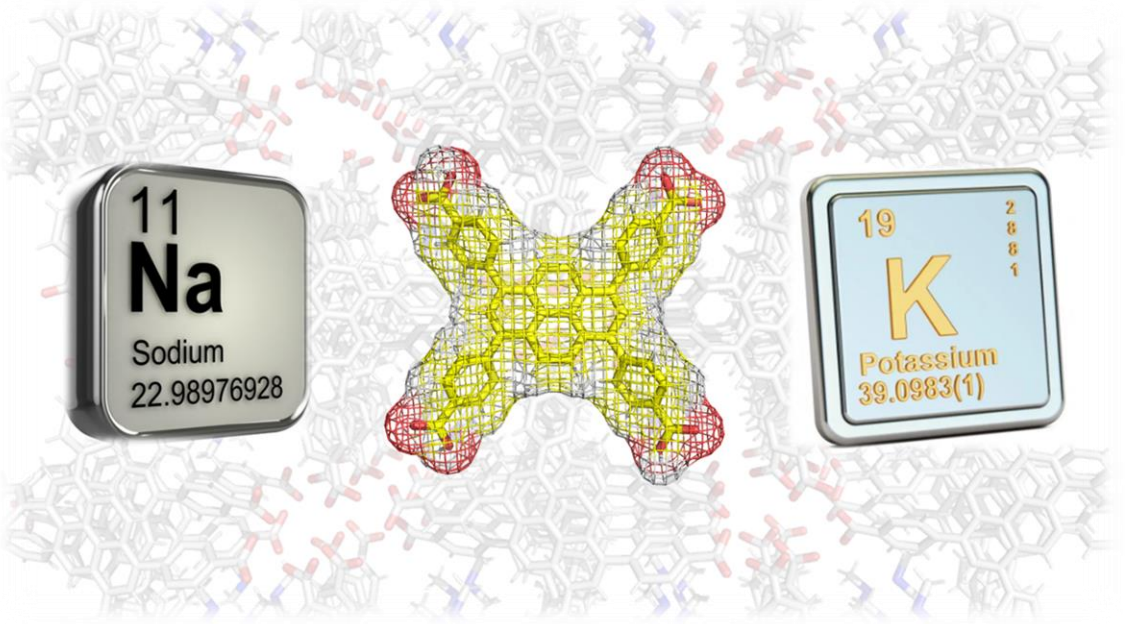

Statement of Authorship

Title of Paper	Structural modulation of the photophysical and electronic properties of pyrene-based 3D metal–organic frameworks derived from s-block metals
Publication Status	☑ Published ☐ Accepted for Publication ☐ Submitted for Publication ☐ Unpublished and Unsubmitted w ork w ritten in manuscript style
Publication Details	Coleman, C. N.; Tapping P. C.; Huxley, M. T.; Kee, T. W.; Huang, D. M.; Doonan, C. J.; Sumby, C. J. *CrystEngComm*, 2021, **23**, 82-90

Principal Author

Name of Principal Author (Candidate)	Christopher Coleman
Contribution to the Paper	Design and development of the synthesis and subsequent characterization of the novel materials described in the publication. Orchestrating the contributions of collaborators. Preparation, drafting and revision of the manuscript.
Overall percentage (%)	70%
Certification:	This paper reports on original research I conducted during the period of my Higher Degree by Research candidature and is not subject to any obligations or contractual agreements with a third party that would constrain its inclusion in this thesis. I am the primary author of this paper.
Signature	Date 30/4/21

Co-Author Contributions

By signing the Statement of Authorship, each author certifies that:

i. the candidate's stated contribution to the publication is accurate (as detailed above);

ii. permission is granted for the candidate in include the publication in the thesis; and

iii. the sum of all co-author contributions is equal to 100% less the candidate's stated contribution.

Name of Co-Author	Patrick C. Tapping
Contribution to the Paper	Collection and interpretation of all time resolved spectroscopy data. Preparation and revision of the manuscript.
Signature	Date 4/5/21

Name of Co-Author	Michael T. Huxley
Contribution to the Paper	Assisted in creating several figures featured in the manuscript and supporting information.
Signature	Date 4/5/21

Please cut and paste additional co-author panels here as required.

Name of Co-Author	Tak W. Kee		
Contribution to the Paper	Assisted in interpretation of time resolved spectral data and the revision of the manuscript.		
Signature		Date	4/5/21
Name of Co-Author	David M. Huang		
Contribution to the Paper	Responsible for quantum calculations and interpretation of the results. Preparation and revision of the manuscript including several figures in the paper and supporting information.		
Signature		Date	4/05/21
Name of Co-Author	Christian J. Doonan		
Contribution to the Paper	Assisted in with experiment design, drafting and revision of the manuscript.		
Signature		Date	5/05/21
Name of Co-Author	Christopher J. Sumby		
Contribution to the Paper	Assisted in analysis and refinement of x-ray crystallography data, drafting and revision of the manuscript.		
Signature		Date	5/05/21

2.1 Abstract

Materials in which charge delocalization and migration can be tuned are critical for electronic applications. Crystalline framework materials containing π-rich polycyclic aromatic moieties, such as pyrene, can provide a pathway for fast anisotropic charge transport. The extent of interchromophore interaction for structurally distinct assemblies of the π-conjugated aromatic ligand 4,4',4'',4'''-(1,3,6,8-pyrenetetrayl) tetrabenzoic acid (TBAPy) was studied within two novel metal–organic frameworks (MOFs), Na(TBAPy)(DMF) and K(TBAPy)(DMF), via steady-state and time-resolved spectroscopic techniques. Single-crystal X-ray diffraction was used to determine the structures of K(TBAPy)(DMF) and Na(TBAPy)(DMF), which both form 3D MOFs comprising 1D rod-like SBUs surrounded by columnar stacks of TBAPy that are aligned in an eclipsed and x-shaped (staggered) geometry, respectively. Spectroscopic and computational results indicate significant chromophore interactions and potentially fast charge transport. Furthermore, distinct transient emission decay profiles are observed and are attributed to significant differences in the stacking orientation of the organic ligands in the two MOFs. Lastly, the study identifies design principles that may be exploited in the rational construction of s-block based MOFs for microelectronic and sensing applications.

2.2 Introduction

Metal−organic frameworks (MOFs) are a class of porous materials that are synthesized via a "building-block" approach from organic links and metal-based nodes.[1] They have been investigated for their potential applications in catalysis,[2] gas storage/separation,[3] biotechnology[4] and sensing.[5] However, in recent years, there has been a growing interest in the synthesis of electrically active MOFs.[6] One strategy that has been employed in the exploration of charge transport in both MOF, and related COF (covalent-organic framework) materials,[7] is to construct networks that possess π-rich organic components.[8] A design imperative of this approach is to position the organic linkers close enough together within the framework to allow for through-space charge transport.[9]

This represents a significant challenge for MOFs synthesized from carboxylate-functionalized linkers as they typically react with transition metal salts to form discrete inorganic nodes that engender 3D net topologies[10] in which the organic units are separated on length scales that preclude orbital overlap. An instructive example is the Zr-based MOF NU-1000, which is constructed from π-rich 4,4',4'',4'''-(1,3,6,8-pyrenetetrayl) tetrabenzoic acid (TBAPy) linkers that are separated by a minimum of 10.94 Å (centroid to centroid) due to the eight-coordinate Zr_6O_8 secondary building units (SBUs).[11] To overcome the geometrical constraints imposed by 0D nodes, 1D rod-like SBUs can be employed to facilitate close

contact of the organic moieties. Although there are examples of infinite rod SBUs composed of transition metals (e.g. MIL-53[12] and MOF-74(M)[13]), we sought to synthesize TBAPy-based MOFs from s-block metals which are known to form 1D SBUs. The alkali metals sodium and potassium are particularly attractive precursor elements due to their availability, low cost and ecological compatibility.[14] Further, the network topologies of alkali metal MOFs are typically dominated by densely packed metal-O_n [n = 6–10] polyhedra, forming chains or layers, interconnected by organic linkers.[15] Nevertheless, the non-directional, ionic nature of s-block carboxylate bonds renders rational design of s-block MOFs a challenging task.

The net-topologies of the s-block MOFs are heavily influenced by the shape and steric bulk of the ligands, π orbital interactions, as well as solvent polarity.[16] Thus, we surmised that an organic linker that has a strong preference to form π-stacked structures[17] may drive the formation of a network architecture with closely spaced or "stacked" TBAPy moieties. This hypothesis is supported by recent work that shows TBAPy capable of forming a robust hydrogen-bonded organic framework (PFC-1)[18] that displays permanent porosity with a surface area of 2122 m^2g^{-1}, and exceptional chemical stability.

Previously reported MOFs based on TBAPy (NU-1000, NU-901, ROD-7)[19,20,21] have been studied for their solid-state photophysical properties with a focus on interchromophoric interaction.[22] However, in these examples the chromophore spacing is longer than optimal (<4 Å), with the closest being an 8.76 Å centroid-centroid distance in the case of ROD-7. Thus, despite the intrinsic photoactivity of TBAPy, these MOFs are insulators and provide limited capacity for exciton delocalization or charge transport. In this study we report the synthesis of two new 3D MOFs based on TBAPy organic linkers and the s-block metal ions Na^+ and K^+, Na(TBAPy)(DMF) and K(TBAPy)(DMF), respectively. Structure determination, by single crystal X-ray diffraction (SCXRD), reveals that in these materials the pyrene moieties are positioned <4 Å apart with distinct eclipsed and x-shaped (staggered) arrangements, allowing for significant amplification of the pyrene–pyrene electronic coupling. Thus, given the close stacking arrangement observed for Na(TBAPy)(DMF) and K(TBAPy)(DMF) we examined their photoemission and charge-transport properties. Furthermore, Na(TBAPy)(DMF) and K(TBAPy)(DMF) offer the unique opportunity to compare how the relative alignment of the chromophores, "eclipsed" in K(TBAPy)(DMF) and a novel "x-shape" or staggered arrangement in Na(TBAPy)(DMF), influence the photophysical properties of the material. Indeed, time-resolved fluorescence spectroscopy, supported by computational analysis, suggests that energy transfer is sensitive to the orientation of the chromophores. In addition, to assess the viability of using these materials as semi-conductors, we fabricated a light-emitting diode (LED) that successfully integrates Na(TBAPy)(DMF) as a hole-transport layer.

2.3 Experimental

General Details

All chemicals were obtained from commercial vendors (1,3,6,8 tetrabromopyrene, Sigma Aldrich, purity >97%; 4 ethoxycarbonylphenyl boronic acid, Boron Molecular, purity >97%) and used without further purification, unless otherwise stated. Dioxane was degassed with Ar prior to use. Tetraethyl 4,4′,4″,4‴-(pyrene-1,3,6,8-tetrayl) tetrabenzoate and the free carboxylic acid, TBAPy, were synthesized using previously reported method23 with some minor modification (see SI section 2). Powder X-ray diffraction data were collected on a Bruker Advance D8 diffractometer equipped with a capillary stage using Cu Kα radiation (λ = 1.5418 Å). NMR spectra were recorded on a Varian 500 MHz spectrometer operating at 23 °C and equipped with a 5 mm probe.

Single Crystal X-ray Diffraction (SCXRD). Diffraction data were collected for single crystals mounted on nylon loops in Paratone-N at 100 K on the MX1 beamline of the Australia Synchrotron using the BluIce software interface,[24] λ = 0.71073 Å. N_{tot} reflections were merged to N unique (R_{int} quoted) after a multi-scan absorption correction (proprietary software) and used in the full matrix least squares refinements on F^2, N_o with $F > 4\sigma(F)$ being considered 'observed'. The structure was solved using SHELXT[25] and refined using SHELXL[26], interfaced through the programs X-Seed[27] and Olex.[28] Unless otherwise stated, anisotropic displacement parameter forms were refined for the non-hydrogen atoms; hydrogen atoms were treated with a riding model [weights: $(\sigma^2(F_o)^2 + (aP)^2 + (bP))^{-1}$; $P = (F_o^2 + 2F_c^2)/3$]. Neutral atom complex scattering factors were used. Additional refinement details, crystallographic data and refinement parameters are found in the ESI (Section 4, Table S2).

Spectroscopy. Diffuse reflectance spectra were measured on solid samples using a Varian Cary 5000 spectrophotometer fitted with a Praying Mantis Diffuse Reflectance Accessory. Steady-state fluorescence measurements on solid samples were conducted on a Perkin Elmer LS 55 Spectrometer (slit widths: ex 2.5nm, em 2.5 nm) . Time-resolved fluorescence data were obtained using time-correlated single photon counting (TCSPC) on a commercial spectrometer (Halcyone, Ultrafast Systems). Solid MOF samples were mounted inside 0.8 mm glass capillaries and measured in reflection mode. The 400 nm excitation laser was generated by frequency doubling a portion of the output of a Ti-sapphire oscillator (Tsunami, Spectra Physics), with a pulse duration of ~100 fs and a pulse-picker used to reduce the repetition rate to 6.7 MHz. Multiexponential fits to the decay kinetics use a function of the form $I(t) = \sum_n A_n \exp(-t/\tau_n)$ convoluted with a Gaussian instrument response function of 0.65 ns. Amplitudes are normalized so that $\sum_n |A_n| = 1$ (see SI section 3).

Quantum-chemical calculations

Density functional theory (DFT) calculations were performed with Q-Chem version 5.1.1.29 Calculations of excited electronic states used time-dependent DFT (TD-DFT), while charge-transfer calculations used constrained density functional theory (CDFT)[30] and CDFT configuration interaction (CDFT-CI).[31,32] All geometries were optimized at the ωB97X-D/6-31G* level,[33] using DFT for ground states and TD-DFT for excited states. Single-point calculations were performed on optimized geometries at the ωB97X-D/6-31+G* level. All calculated electronic properties are at this level unless otherwise stated.

Carboxylate carbon and oxygen atom positions were constrained to their positions in the experimental crystal structure (carboxylate groups from the crystal structure were terminated by hydrogens to neutralize the charge). Ground-state geometry optimizations were initiated from the experimental crystal structure, while optimizations of excited states and charge-localized states were initiated from the optimized ground-state geometry.

MOF Synthesis

Preparation of Na(TBAPy)(DMF). TBAPy (50 mg, 73 µmol) and $NaHCO_3$ (25 mg, 0.29 mmol) were suspended in water (30 mL) and the solution was heated at reflux for 24 hours. The reaction mixture was allowed to cool, and the water was removed under vacuum. The yellow solid was then dissolved in a mixture of DMF (5 mL) and water (5 mL) which was allowed to slowly evaporate over several days resulting in the formation of needle-like yellow crystals of Na(TBAPy)(DMF), which were washed with DMF (see Fig. S10).

Crystals suitable for SCXRD were grown by slow vapor diffusion of acetone into a concentrated solution of Na(TBAPy)(DMF) in DMF/H_2O (1:1). The resulting yellow rod-shaped crystals (Na(TBAPy)(acetone) were suitable for SCXRD. These were then transferred to a solution of DMF and allowed to soak for several days in order to exchange the coordinated acetone for DMF and give Na(TBAPy)(DMF). IR (Vmax, cm-1): 1675 (s, CO), 1603 (m, CO), 1374 (s, C=C), 1269 (s, CO).

Preparation of K(TBAPy)(DMF). TBAPy (50 mg, 73 µmol) and K_2CO_3 (40 mg, 0.29 mmol) were dissolved in water (30 mL) and the solution was heated at reflux for 24 hours. The reaction mixture was allowed to cool, and the water was removed under vacuum. The yellow solid was then dissolved in a mixture of DMF (5 mL) and water (5 mL) and the solution was allowed to slowly evaporate over several days resulting in the formation of needle-like yellow crystals of K(TBAPy)(DMF) which were washed with DMF (see Fig. S10). Crystals suitable for SCXRD were grown by a solvothermal method. TBAPy (25 mg, 37 µmol) and K_2CO_3(20mg, 0.14 mmol) were added to DMF (4 mL), water (2 mL) and conc. HCl (80 µL)

in a 20 mL glass vial. The solution was heated at 100°C for 24 hours to give yellow rod-shaped crystals of K(TBAPy)(DMF). IR (Vmax, cm-1): 3290 (br, C-H), 1685 (m, CO), 1608 (s, CO), 1401 (s, C=C).

Preparation of LED Device

A glass indium-tin oxide (ITO) substrate was coated with Na(TBAPy)(DMF) and a light emitting copolymer (PDOF and MEH-PPV). Details of the device fabrication can be found in the ESI (Fig. S11).

2.4 Results and Discussion

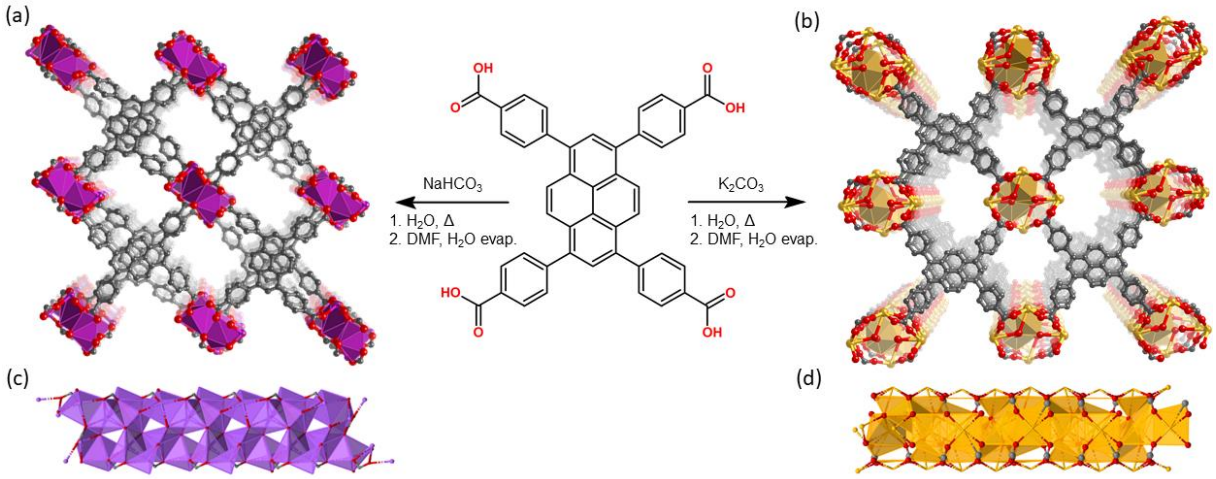

Fig. 1. Perspective views of the structures of the TBAPy-based MOFs obtained by single crystal X-ray diffraction ((hydrogen and solvent molecules omitted for clarity). The extended structures of **(a)** Na(TBAPy)(DMF) and **(b)** K(TBAPy)(DMF), and their 1D SBUs **(c)** and **(d)**, respectively, are provided. The materials used for all analyses were synthesised in the two-step procedures shown. Atoms are represented as: carbon (grey), oxygen (red), sodium (purple) and potassium (orange); hydrogen atoms and the non-coordinated atoms of solvate molecules are omitted.

2.4.1 MOF synthesis and structures

Na(TBAPy)(DMF) and K(TBAPy)(DMF) were synthesized by reacting an aqueous suspension of TBAPy with sodium carbonate or potassium carbonate, respectively, under reflux for 24 hours to form the TBAPy salts (Fig. 1). Removal of water afforded pale-yellow powders that were recrystallized via slow evaporation from DMF/H_2O to yield pure crystalline material (see Figs. S2 and S10). Single crystals for

an acetone-solvated form of the sodium MOF were obtained by vapor diffusion of acetone into a concentrated 1:1 DMF/H2O solution of Na(TBAPy)(DMF), followed by solvent exchange with DMF to form the DMF solvate, Na(TBAPy)(DMF) (see Fig. S4 for a structural comparison); single crystals of K(TBAPy)(DMF) were obtained by a solvothermal method.

Na(TBAPy)(DMF) crystallizes in the monoclinic space group P21/n. The ligand occupies two distinct chemical environments, with an asymmetric unit consisting of two partial ligands (one complete TBAPy molecule), four sodium atoms and two coordinated DMF molecules; this gives the formula $[Na_4(TBAPy)(DMF)_2]$. The structure of Na(TBAPy)(DMF) comprises a 1D SBU extending along the b axis (Fig. 1c), with the ligand acting as a four connecting centre. Within the linear SBU, the metal centres are present in trigonal prismatic and distorted octahedral coordination geometries. The coordination environment of the sodium SBU includes ionic bonding to oxygen atoms of carboxylate and solvent molecules, as well as bridging water molecules. The orientation by which the linkers stack is unique. As opposed to an eclipsed or "slip stacked" arrangement, the pyrene cores form an x-shape (see Figs. 1a and 4b) and the 4 benzoate groups on each ligand form two co-facial and two edge-to-face π-stacking interactions with neighboring ligands. Furthermore, subtle structural changes can be induced for the Na-based material by exchanging the solvent and altering the crystallization methods. Powder X-ray diffraction (PXRD) (Fig. S3) shows two distinct forms of the sodium-based MOF can be obtained, namely Na(TBAPy)(DMF) and Na(TBAPy)(acetone). Sodium is prone to coordinate a variety of solvents, and well-defined solvent molecules appear as integral features of the molecular composition, with Na(TBAPy)(acetone) featuring coordinated acetone in place of DMF but also coordinated water which subtly modifies the diameter of the SBU (see Fig. S4) and the unit cell.

K(TBAPy)(DMF) crystallizes in monoclinic space group P21/c. The asymmetric unit consists of two ligand molecules, nine potassium atoms, coordinated solvent (DMF and water), and a 50% occupied carbonate anion: $[K_9(TBAPy)_2(H_2O)_{8.25}(DMF)_{3.25}](CO_3)_{0.5}$. A salient feature of K(TBAPy)(DMF) is that, in contrast to Na(TBAPy)(DMF), the TPABY links are aligned in an eclipsed formation (Fig. 1b). This arrangement results in all carbon atoms in the stacked pyrene moieties separated by ca. 3.85 Å, with the ligands aligning in an extended H-aggregate configuration.[34,35] The larger unit cell in the potassium MOF is the result of disordered solvent molecules which alter the dihedral angles on adjacent TBAPy molecules (see Fig. S9). However, despite these crystallographic differences and in contrast to Na(TBAPy)(DMF), the linkers of K(TBAPy)(DMF) are stacked directly on top of each other with all ligands having almost identical chemical environments. This is an important consideration in the analysis of the spectral data. The SBU in K(TBAPy)(DMF) comprises 1D potassium oxide chains (Fig. 1d). The potassium ions co-ordinate with up to 7 oxygen atoms that include carboxylate groups, DMF and

water molecules. PXRD data for a sample of K(TBAPy)(DMF) obtained by slow evaporation matches the structure determined by single crystal diffraction, thus confirming bulk purity (see Fig. 2).

Due to the 1D rod-like SBUs that feature in Na(TBAPy)(DMF) and K(TBAPy)(DMF), close-packing of the pyrene moieties is observed. This, in theory, has the potential to facilitate charge transfer through π-orbital overlap as well as trigger noticeable interchromophoric interactions. The close packing of linkers also appears to confer some stability to the MOFs. The result is that both structures are stable and retain their crystallinity for months after being removed from solvent, provided they are kept in an environment devoid of excess moisture.

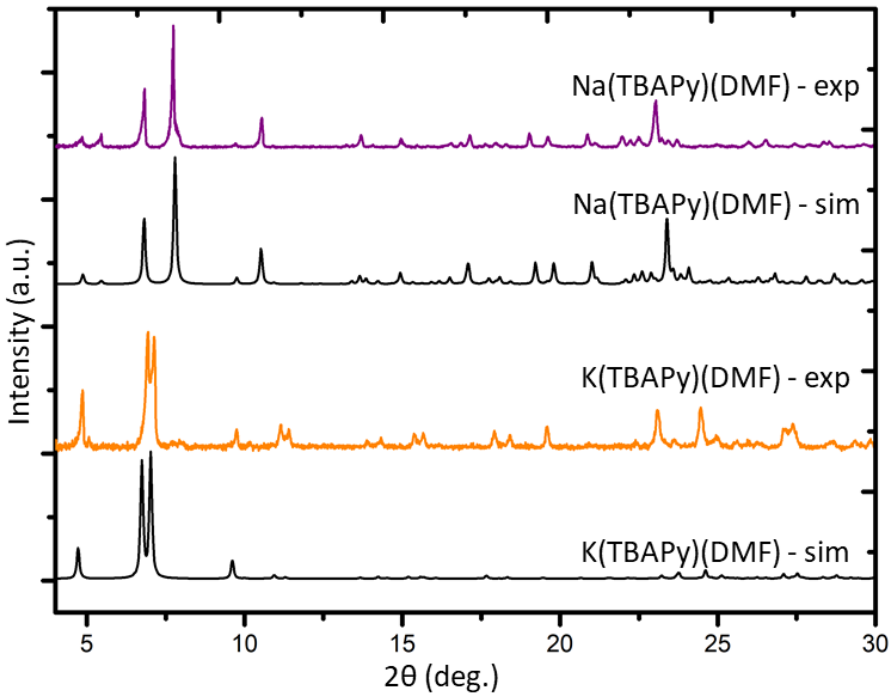

Fig. 2. Simulated (sim) and experimental (exp) PXRD patterns of Na(TBAPy)(DMF) and K(TBAPy)(DMF)

2.4.2 Photophysical properties

In terms of quantum yield and emissive lifetimes, pyrene ranks considerably higher than many well-known and commonly employed chromophores.[36] Additionally, its spectral signature is well known to be extremely sensitive to its environment.[37] Pyrene-based MOFs have been thoroughly investigated for their photophysical performance characteristics; however, Na(TBAPy)(DMF) and K(TBAPy)(DMF) provide unprecedented opportunity to examine the effects of chromophore alignment in two close-stacked systems. Thus, to understand the nature of the chromophoric interactions we carried out steady-state and time-resolved spectroscopic analysis on each MOF. We anticipated that the different

stacking arrangements present in Na(TBAPy)(DMF) and K(TBAPy)(DMF) would manifest distinct emission decay profiles as a function of their topology. Previously reported spectral data for the TBAPY ligand showed solvent-dependent emission peaks for the same materials.[38,39,40] To avoid the effects of solvent polarity on the transition energies we conducted spectroscopic analysis on dried material.

The high chromophore density in Na(TBAPy)(DMF) and K(TBAPy)(DMF) should result in effective photon absorption. The calculated molar density of TBAPy in each framework was found to be 1.62 mol/dm^3 for Na(TBAPy)(DMF) and 1.40 mol/dm^3 for K(TBAPy)(DMF). We note that both values are considerably higher than that of the zirconium-based MOF NU-1000 (0.41 mol/dm3).[39] Close positioning of photoactive ligands typically leads to nonradiative pathways that can quench fluorescence.[41] However, despite the proximity of the pyrene groups in Na(TBAPy)(DMF) and K(TBAPy)(DMF), both MOFs are fluorescent in the solid state. The solid-state absorption profile features distinct and well-defined peaks and troughs ranging from 225 to 450 nm (with a maximum at ca. 405 nm). Despite the different relative orientations of the TBAPy ligands in the two MOFs, both show almost identical absorption profiles.

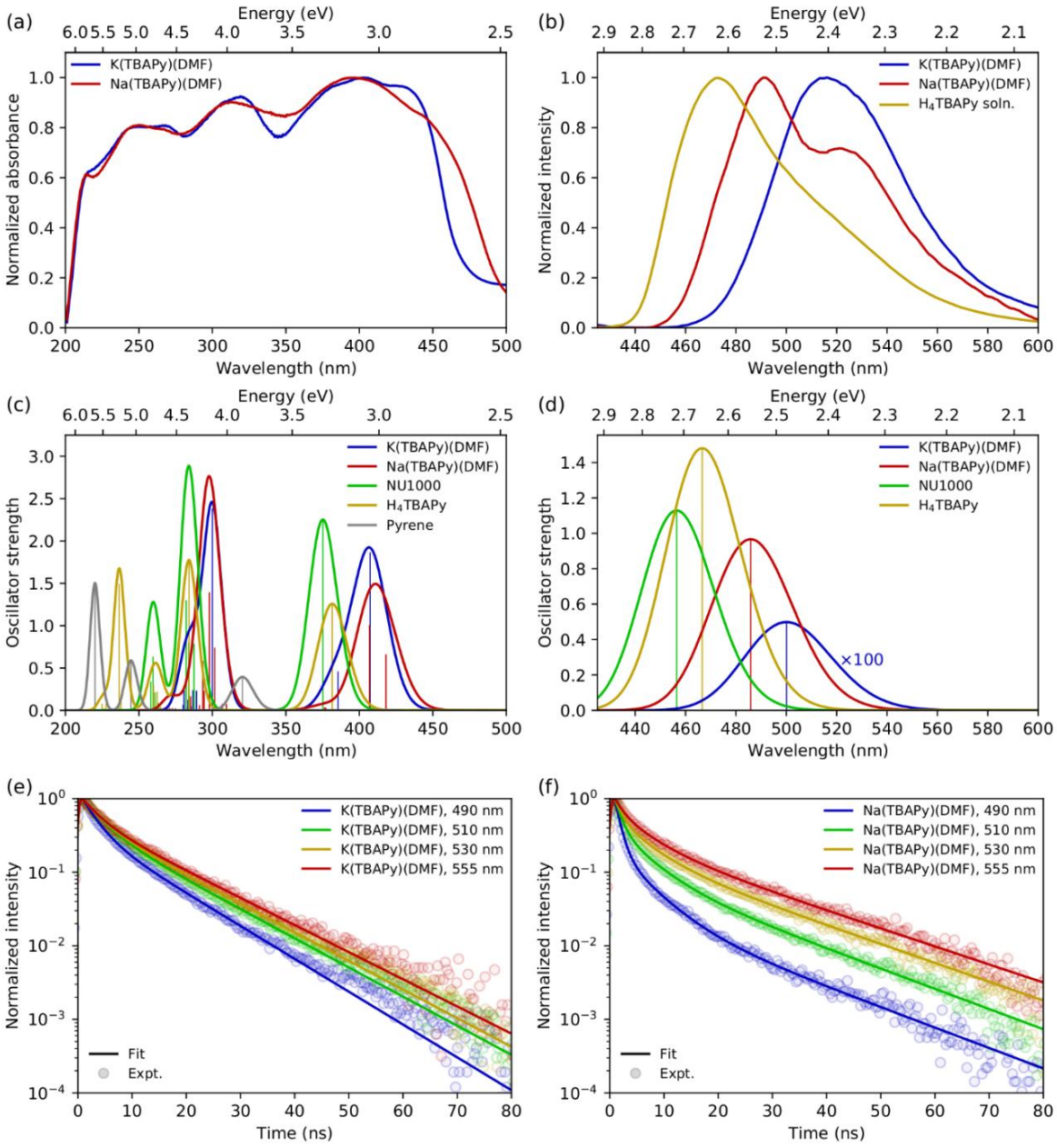

Fig. 3. **(a)** Solid-state diffuse reflectance spectra of K(TBAPy)(DMF) (blue) and Na(TBAPy)(DMF) (red). (b) Emission spectra for solid-state K(TBAPy)(DMF) (blue) and K(TBAPy)(DMF) (red) using 405 nm excitation, with the H_4TBAPy linker in DMF solution (yellow) for reference. Calculated **(c)** absorption and **(d)** emission spectra for the same species, with spectra for NU-1000 (green) and pyrene (grey) included for reference (computed spectra have been shifted by 0.4 eV and convoluted with a Gaussian of full width at half maximum (FWHM) of 0.2 eV in all cases). Time-resolved fluorescence kinetics at different detection wavelengths for **(e)** K(TBAPy)(DMF) and **(f)** Na(TBAPy)(DMF). Fits to a multiexponential decay model are shown with solid lines, with fitting parameters given in Table S1.

The solid-state emission spectra for K(TBAPy)(DMF) and Na(TBAPy)(DMF) are shown in Fig. 3b. The emission from K(TBAPy)(DMF) is centred at 515 nm and largely featureless but is significantly red shifted compared to that of the free H_4TBAPy linker in solution. In contrast, the Na(TBAPy)(DMF) emission exhibits distinct structure, with the main peak at 490 nm and a well-defined shoulder around 530 nm. The shift of the emission peaks to lower energies relative to the free H_4TBAPy linker in solution is indicative of strong electronic coupling between the chromophore units resulting from close packing of the aromatic pyrene cores of the TBAPy linkers in the solid-state. This molecular architecture allows significant π–π interactions, and thus delocalization of the excitation. The structure evident in the Na(TBAPy)(DMF) emission can be attributed to a vibronic progression. The shoulder is lower in energy than the main peak by approximately 1600 cm^{-1}, which can be assigned to the aromatic C=C bond vibration in the pyrene cores. The absence of structure in the K(TBAPy)(DMF) emission can be attributed to the distinct alignments of the pyrene units observed in the two MOFs. The packing of the linkers in K(TBAPy)(DMF) is effectively an ideal H-aggregate,[35,42] in which the eclipsed arrangement of the chromophore pairs suppresses the 0–0 vibronic transition, leaving the 0–1 peak to dominate the spectrum. The x-shaped stacking of the linkers in Na(TBAPy)(DMF) results in coupling that is intermediate between that of a J- and an H-aggregate , and thus the 0–0 and 0–1 vibronic peaks are both present. This aggregate behavior can also account for the differences between the absorption spectra of the MOFs (Fig. 3a), which show that absorption in the Na(TBAPy)(DMF) extends further into the low-energy region, while the lowest energy 0–0 vibronic absorption peak is attenuated in K(TBAPy)(DMF).

Fluorescence decay kinetics were obtained for the two MOFs at several emission wavelengths, shown in Figs. 3e and 3f. The curves were fit to a multiexponential decay model, with parameters given in Table S1. For K(TBAPy)(DMF), the kinetic profiles are almost identical at all detection wavelengths. The slightly faster decay at 490 nm is at the blue edge of the absorption peak and is indicative of spectral migration to lower energies due to excited-state structural relaxation or exciton migration. Na(TBAPy)(DMF), however, displays significantly different kinetics at each detection wavelength, with noticeably faster decays at shorter wavelengths, particularly at short times ($\lesssim$5–10 ns), which also indicates time-dependent spectral migration, but to a greater extent and at a faster rate than that observed in K(TBAPy)(DMF). The longer time ($\gtrsim$5–10 ns) decay, which occurs approximately uniformly across all wavelengths in both MOFs, can be attributed to relaxation to the ground state. The faster decays on both time scales in Na(TBAPy)(DMF) compared with K(TBAPy)(DMF) can again be attributed to the arrangement of the chromophores within the MOFs, as the H-aggregate[35] nature of K(TBAPy)(DMF) is expected to result in slower emission and reduced exciton migration by resonance energy transfer.

Although pyrene dimers stacked directly on top of each other have been observed and probed previously,[43] to the best of our knowledge the x-shaped or staggered configuration of pyrene present in Na(TBAPy)(DMF) (Fig. 4) has not been documented. To clarify how the configuration of ligands influences the electronic coupling and excited-state properties in the two s-block MOFs, we performed density functional theory (DFT) calculations on the two closest ligand pairs in each MOF, with which the carboxylate C and O atoms fixed at their positions in the experimental SCXRD structure to mimic the coordination constraints in the MOF. For comparison, analogous calculations were performed on the closest ligand pair in NU-1000 and similar calculations were performed on the TBAPy monomer and on pyrene without geometric constraints. Absorption and emission spectra were calculated using time-dependent DFT (TD-DFT) on the optimized geometry of the electronic ground state and first excited state, respectively. Details of the calculations are given in the ESI.

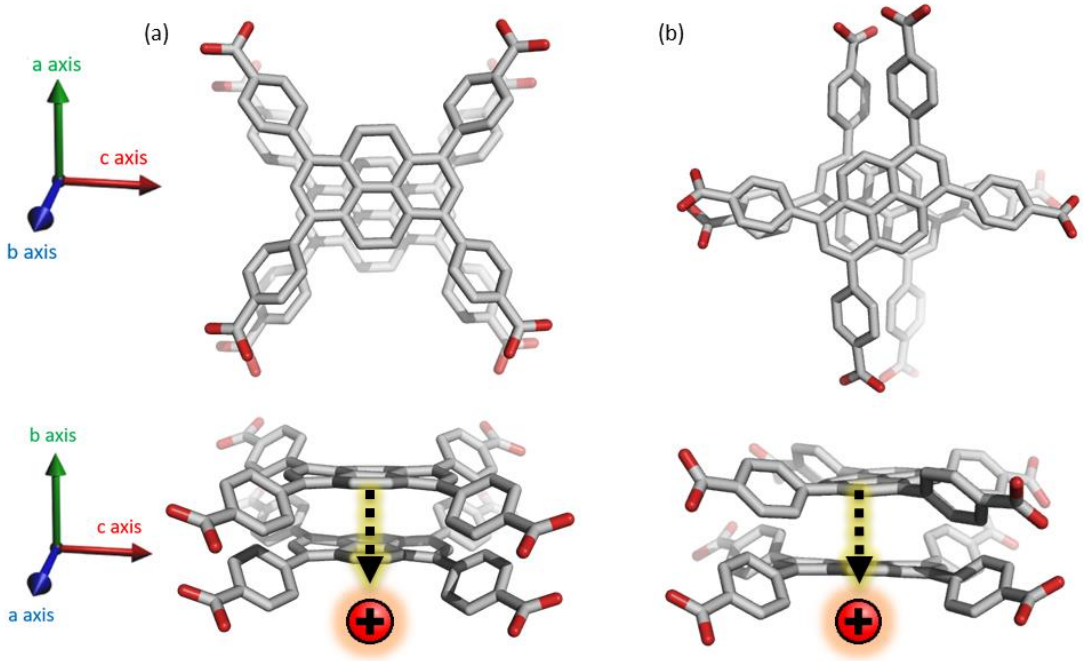

Fig. 4. Relative orientation of the TBAPy ligand in **(a)** K(TBAPy)(DMF), eclipsed, and **(b)** Na(TBAPy)(DMF), x-shaped. The TBAPy ligands are viewed along the crystallographic b axis (top) and a axis (below). Dashed lines represent the direction of charge transport.

Consistent with experiment, the absorption spectra of the K(TBAPy)(DMF) and Na(TBAPy)(DMF) MOFs calculated by TD-DFT on the optimized ground-state geometries of the constrained ligand dimers have similar peak positions but are blue-shifted (by ~0.4–0.6 eV) compared with experiment, as shown in

Fig. 3c. However, the lowest energy absorption transitions shifted to lower energy compared with those the NU-1000 MOF and the TBAPy monomer (by ~0.2 eV in both cases), indicating substantially stronger electronic coupling between the ligands in K(TBAPy)(DMF) and Na(TBAPy)(DMF) compared with NU-1000. The discrepancy between the calculations and experiment can be partly attributed to using a dimer model in the calculations, which neglects coupling between multiple ligands in the MOF. Also calculated is the absorption spectrum of pyrene, which is significantly blue shifted compared with the TBAPy monomer, indicating significant electron delocalization between the pyrene and phenyl groups in H_4TBAPy.

The calculations show that the transition dipole moment (TDM) of the lowest energy transition of the TBAPy monomer is aligned in the plane along the long axis of the pyrene core, as shown in Fig. S13a. The orientation of the ligands in the Na(TBAPy)(DMF) MOF dimer at an angle to one another (105°) results in an excited-state electronic coupling that is intermediate between a H and a J-type interaction, producing two almost degenerate lowest energy absorption transitions (separated by ~0.08 eV) with significant TDMs that are almost orthogonal to one another, as shown in Fig. S13b. On the other hand, confirming our interpretation of the spectroscopic data, the parallel orientation of the monomers in the K(TBAPy)(DMF) MOF dimer yields an H-type interaction, with the lowest energy absorption transition having negligible oscillator strength and the most intense transition being the second lowest, which has a TDM aligned in the same direction as that of the TBAPy monomer (Fig. S14c).

Also consistent with the experiment, the emission of the Na(TBAPy)(DMF) MOF dimer is red-shifted by ~0.4 eV with respect to absorption due to structural relaxation of the excited state (Fig. 3d), but the Stokes shift is about that observed experimentally. This discrepancy is likely due to the strong geometric constraints placed on the carboxylate atom positions in the calculations, which neglect flexibility of the MOF. As shown in Fig. S12, the atoms in the Na(TBAPy)(DMF) MOF dimer hardly move between the ground and excited-state geometries. The Stokes shift calculated for the TBAPy monomer, for which no geometric constraints were applied, is significantly larger, at ~0.6 eV. This larger shift appears to be related to the larger change in the dihedral angle between the pyrene core and phenyl substituents in the excited state of the monomer compared with the MOF dimers, which leads to greater electron delocalization due to the more planar geometry. Calculations on the K(TBAPy)(DMF) MOF dimer indicate that the purely electronic the S1→S0 transition does not occur, which is consistent with the presence of H-type coupling, with emission made possible by vibronic coupling that is neglected in our purely electronic calculations.

Unlike previous reports examining the topology-dependent emissive properties of MOFs containing the TBAPy ligand,[44,22] we were reluctant to classify the emission as resulting from excimer formation.

Although our model overestimates how rigidly the ligands are held in position, we see no strong evidence to suggest the experimentally observed steady-state or time-resolved emission are a result of significant geometric rearrangement of the ligands within the lattice that would be associated with excimer formation. The Stokes shift[45] and peak width of the steady-state emission of both s-block MOFs is much smaller than that associated with excimer formation in pyrene, and the emission is not substantially broadened compared with the isolated TBAPy ligand, as shown in Fig. 3. In addition, the shortest decay times measured in the time-resolved emission are an order of magnitude longer than that of excimer formation in crystalline pyrene.[45] Furthermore, the calculated changes in the excited-state geometry compared with the ground-state geometry are much smaller than those calculated for pyrene excimers.[46,43]

2.4.3 Charge-transport properties

Although most MOFs are insulators with no capacity for exciton delocalization between ligands, intrinsic charge transport within a MOF is still an area of emerging interest.[47] A design challenge for electrically conductive MOFs is that charge transport decreases exponentially with increased intermolecular distance between frontier orbitals.[48] We have shown that the two s-block MOFs presented in this work possess a close packed arrangement of π-rich chromophores and thus may facilitate exciton delocalization and charge mobility. However, conductivity experiments on microcrystalline materials are notoriously unreliable and can differ by orders of magnitude.[49] For this reason we decided to use quantum-chemical calculations to estimate the effect of the relative position and orientation of the ligands on charge-transfer rates in the s-block MOFs and a related pyrene-based MOF. Charge-transfer parameters for hole transfer in the K(TBAPy)(DMF) and Na(TBAPy)(DMF) MOFs were calculated and compared with those for NU-1000. Constrained density functional theory (CDFT) was used to localize a +1 charge on one of the monomers in each MOF dimer and CDFT-CI was used to calculate the electronic coupling V_{da} and reorganization energy λ for the process of transferring this +1 charge from one monomer to the other. The hole transfer rate constant k_h was also calculated using Marcus theory[50] according to

$$k_{\mathrm{h}} = \frac{2\pi}{\hbar}|V_{\mathrm{da}}|^2\sqrt{\frac{1}{4\pi k_{\mathrm{B}}T\lambda}}\exp\left[-\frac{(\Delta G^{\circ}+\lambda)^2}{4\lambda k_{\mathrm{B}}T}\right] \quad (1)$$

where ΔG° is the free-energy change for the process (which is zero here because the hole donor and acceptor are the same), T is the temperature, k_B is the Boltzmann constant and $\hbar$ is the reduced Planck's constant. As shown in Table S2, although the reorganization energy for all three MOFs is similar, the electronic couplings in the K(TBAPy)(DMF) and Na(TBAPy)(DMF) MOFs are both an order-

of-magnitude larger than that of NU-1000, as a result of the much closer spacing between the ligands in these MOFs (<4 Å). Consequently, the calculated hole-transfer rate constants for K(TBAPy)(DMF) and Na(TBAPy)(DMF) are two orders of magnitude larger than that of NU-1000, due to the quadratic dependence of the rate constant on the coupling (see Table 1). Furthermore, the different relative orientation of the ligands in the K(TBAPy)(DMF) and Na(TBAPy)(DMF) MOFs results in the electronic coupling and hole-transfer rate constant being respectively a factor of two and four larger for Na(TBAPy)(DMF) compared with K(TBAPy)(DMF). This suggests that charge-transfer properties can be strongly modulated by ligand configuration in these closely related MOFs.

Table 1: Calculated hole-transfer rate constants and measured inter-ligand distances for MOF TBAPy dimers.

MOF	hole transfer rate constant k_h (s^{-1})	two closest ligands (centroid to centroid)
Na(TBAPy)(DMF)	5.7×10^{12}	3.93 Å
K(TBAPy)(DMF)	1.5×10^{12}	3.86 Å
NU-1000	3.3×10^{10}	10.94 Å

Given the encouraging results from quantum-chemical calculations, coupled with the well documented ability of pyrene moieties to facilitate hole transfer in several electronically active polymers and composites,[51] we examined the semiconducting properties of Na(TBAPy)(DMF) by using it to construct a light emitting diode (LED). LEDs generally consist of a conductive substrate, a hole transport layer, and a light-emitting layer.[52] Poly(3,4-ethylenedioxythiophene) polystyrene sulfonate (PEDOT:PSS) can be used as an effective hole transport layer[53] that can prevent the LED from shorting, and transports positive charge to the active light emitting polymer layer.[54] While the PEDOT:PSS layer does not itself emit any light, such hole transport layers have been found to dramatically improve the efficiency of polymer-based LEDs.[55] To this end, we substituted PEDOT:PSS for Na(TBAPy)(DMF) to yield a functioning LED which emitted 580 nm (max) wavelength light at a voltage of 4.45 V (24 mA) (see Fig. S11). Control devices that consisted of just the conductive substrate and the light emitting layer, with no hole transport layer, failed to function. These immediately began to heat and did not emit any light. This device represents the first time a sodium-based MOF has been used as a semiconducting hole transport layer in a functioning LED.

2.5 Conclusion

We successfully synthesized two new, stable, non-interpenetrated s-block-based MOFs, Na(TBAPy)(DMF) and K(TBAPy)(DMF), containing a π-rich photoactive organic linker. As anticipated, the non-directional, ionic metal-ligand bonds yields MOFs possessing rod-like SBUs and close proximity of the pyrene moieties. Interestingly, the pyrene chromophores adopt different relative packing arrangements (eclipsed and x-shaped) that according to computational and spectral data give rise to significantly different electronic coupling. We note that this is the first time an x-shaped (staggered) alignment of pyrene cores has been examined in the solid-state. This work shows that there is broad scope for using s-block MOFs composed of π-rich chromophores for a variety of sensing and electronic applications. Furthermore, they are ideal candidates for fundamental studies on how the level of solvation, solvent polarity, ion exchange, guest molecules, chromophore packing and alignment, and photoinduced structural changes influence the electronic properties of a material. Non-directional, ionic metal-ligand bonds appear to result in an unusually flexible yet stable structure. We believe there is wide scope to examine the effects of external stimuli on these materials. Temperature, level of solvation, solvent polarity, ion exchange, guest molecules and photo induced structural changes are all factors that have the potential to alter the electronic properties of these s-block MOFs. Being spectroscopically and electronically active, these new s-clock MOFs make ideal candidates for a multitude of sensing and electronic applications.

2.6 Additional Information

2.6.1 Acknowledgments

This research was undertaken with the assistance of resources and services from the National Computational Infrastructure (NCI), which is supported by the Australian Government, and from The University of Adelaide's Phoenix High Performance Computing service. This research was undertaken in part using the MX1 and MX2 beamlines at the Australian Synchrotron, part of ANSTO.

2.6.2 Funding Statement

This research is supported by the Science and Industry Endowment Fund (SIEF). CJD and CJS would like to acknowledge the Australian Research Council for funding FT100100400 and FT0991910, respectively.

2.6.3 Data Accessibility

The Supplementary Material contains additional X-ray crystallographic details and powder X-ray diffraction data. Crystallographic information files (cif) have been deposited with the Cambridge Crystallographic Database (CCDC). Deposition numbers 2026823 (**Na(TBAPy)(DMF)**), 2026825 (**Na(TBAPy)(acetone)**), and 2026827 (**K(TBAPy)(DMF)**).

2.6.4 Competing Interests

We have no competing interests.

2.6.5 Author Contributions

CNC led the conception and design of the experiments and was primarily responsible for collecting crystal structures, drafting and revising the manuscript. PCT was involved in the acquisition of time resolved spectroscopic data, analysis and interpretation. DMH conducted the computational component of this work including the interpretation of the quantum calculations. CJD and CJS assisted in interpretation of structural data and were responsible for critically revising the manuscript and final approval of the version to be published.

References

1 O. M. Yaghi, M. O'Keeffe, N. W. Ockwig, H. K. Chae, M. Eddaoudi and J. Kim, *Nature*, 2003, **423**, 705–714; H. Furukawa, K. E. Cordova, M. O'Keeffe and O. M. Yaghi, *Science*, 2013, **341**, 1230444.

2 V. Pascanu, G. González Miera, A. K. Inge and B. Martín-Matute, *J. Am. Chem. Soc.*, 2019, **141**, 7223–7234; D. Yang and B. C. Gates, *ACS Catal.*, 2019, **9**, 1779–1798.

3 Z. Kang, L. Fan and D. Sun, *J. Mater. Chem. A*, 2017, **5**, 10073–10091; (b) X. Zhao, Y. Wang, D.-S. Li, X. Bu and P. Feng, *Adv. Mater.* 2018**, 30**, 1705189.

4 K. Liang, R. Ricco, C. M. Doherty, M. J. Styles, S. Bell, N. Kirby, S. Mudie, D. Haylock, A. J. Hill, C. J. Doonan and P. Falcaro, *Nat. Commun.*, 2015, **6**, 7240; (b) J. W. M. Osterrieth and D. Fairen-Jimenez, *Biotech. J.*, 2020**,** https://doi.org/10.1002/biot.202000005.

5 W. P. Lustig, S. Mukherjee, N. D. Rudd, A. V. Desai, J. Li and S. K. Ghosh, *Chem. Soc. Rev.*, 2017, **46**, 3242–3285.

6 L. Sun, M. G. Campbell and M. Dinca, *Angew. Chem. Int. Ed.*, 2016, **55**, 3566–3579.

7 H. Yang, S. Zhang, L. Han, Z. Zhang, Z. Xue, J. Gao, Y. Li, C. Huang, Y. Yi, H. Liu and Y. Li, *ACS Appl. Mater. Interfaces*, 2016, **8**, 5366–5375.

8 Y. Gao, H. Liu, S. Zhang, Q. Gu, Y. Shen, Y. Ge and B. Yang, *Phys. Chem. Chem. Phys.*, 2018, **20**, 12129–12137.

9 T. C. Narayan, T. Miyakai, S. Seki and M. Dincă, *J. Am. Chem. Soc.*, 2012, **134**, 12932–12935.

10 K. S. Lin, A. K. Adhikari, C. N. Ku, C. L. Chiang and H. Kuo, *Int. J. Hydrogen Energy*, 2012, **37**, 13865–13871.

11 T. Zhang, P. Wang, Z. Gao, Y. An, C. He and C. Duan, *RSC Adv.*, 2018, **8**, 32610–32620.

12 C. W. Ashling, D. N. Johnstone, R. N. Widmer, J. Hou, S. M. Collins, A. F. Sapnik, A. M. Bumstead, P. A. Midgley, P. A. Chater, D. A. Keen and T. D. Bennett, *J. Am. Chem. Soc.*, 2019, **141**, 15641–15648.

13 J. Wang, Y. Fan, H. W. Lee, C. Yi, C. Cheng, X. Zhao and M. Yang, *ACS Appl. Nano Mater.*, 2018, **1**, 3747–3753.

14 S. Krieck and M. Westerhausen, *Inorganics*, 2017, **5**, 8–11.

15 D. Banerjee and J. B. Parise, *Cryst. Growth Des.*, 2011, **11**, 4704–4720.

16 D. L. Reger, A. P. Leitner and M. D. Smith, *Cryst. Growth Des.*, 2016, **16**, 527–536.

17 C. G. Perkins, J. E. Warren, A. Fateeva, K. C. Stylianou, A. McLennan, K. Jelfs, D. Bradshaw and M. J. Rosseinsky, *Micropor. Mesopor. Mater.*, 2012, **157**, 24–32.

18 Q. Yin, P. Zhao, R.-J. Sa, G.-C. Chen, J. Lü, T.-F. Liu and R. Cao, *Angew. Chem. Int. Ed.*, 2018, **57**, 7691–7696.

19 T. Islamoglu, K. I. Otake, P. Li, C. T. Buru, A. W. Peters, I. Akpinar, S. J. Garibay and O. K. Farha, *CrystEngComm*, 2018, **20**, 5913–5918.

20 S. J. Garibay, I. Iordanov, T. Islamoglu, J. B. DeCoste and O. K. Farha, *CrystEngComm*, 2018, **20**, 7066–7070.

21 R. J. Li, M. Li, X. P. Zhou, D. Li and M. O'Keeffe, *Chem. Commun.*, 2014, **50**, 4047–4049.

22 J. Yu, J. Park, A. Van Wyk, G. Rumbles and P. Deria, *J. Am. Chem. Soc.*, 2018, **140**, 10488–10496.

23 T. C. Wang, N. A. Vermeulen, I. S. Kim, A. B. F. Martinson, J. F. Stoddart, J. T. Hupp and O. K. Farha, *Nat. Protoc.*, 2016, **11**, 149–162.

24 T. M. McPhillips, S. E. McPhillips, H. J. Chiu, A. E. Cohen, A. M. Deacon, P. J. Ellis, E. Garman, A. Gonzalez, N. K. Sauter, R. P. Phizackerley, S. M. Soltis and P. Kuhn, *J. Synchrotron Radiat.*, 2002, **9**, 401–406.

25 G. M. Sheldrick, *Acta Crystallogr. Sect. A Found. Crystallogr.*, 2015, **71**, 3–8.

26 G. M. Sheldrick, *Acta Crystallogr. Sect. C Struct. Chem.*, 2015, **71**, 3–8.

27 L. J. Barbour, *J. Supramol. Chem.*, 2001, **1**, 189–191.

28 O. V. Dolomanov, L. J. Bourhis, R. J. Gildea, J. A. K. Howard and H. Puschmann, *J. Appl. Crystallogr.*, 2009, **42**, 339–341.

29 Y. Shao, Z. Gan, E. Epifanovsky, A. T. B. Gilbert, M. Wormit, J. Kussmann, A. W. Lange, A. Behn, J. Deng, X. Feng, D. Ghosh, M. Goldey, P. R. Horn, L. D. Jacobson, I. Kaliman, R. Z. Khaliullin, T. Kuš, A. Landau, J. Liu, E. I. Proynov, Y. M. Rhee, R. M. Richard, M. A. Rohrdanz, R. P. Steele, E. J. Sundstrom, H. L. Woodcock, P. M. Zimmerman, D. Zuev, B. Albrecht, E. Alguire, B. Austin, G. J. O. Beran, Y. A. Bernard, E.

Berquist, K. Brandhorst, K. B. Bravaya, S. T. Brown, D. Casanova, C. M. Chang, Y. Chen, S. H. Chien, K. D. Closser, D. L. Crittenden, M. Diedenhofen, R. A. Distasio, H. Do, A. D. Dutoi, R. G. Edgar, S. Fatehi, L. Fusti-Molnar, A. Ghysels, A. Golubeva-Zadorozhnaya, J. Gomes, M. W. D. Hanson-Heine, P. H. P. Harbach, A. W. Hauser, E. G. Hohenstein, Z. C. Holden, T. C. Jagau, H. Ji, B. Kaduk, K. Khistyaev, J. Kim, J. Kim, R. A. King, P. Klunzinger, D. Kosenkov, T. Kowalczyk, C. M. Krauter, K. U. Lao, A. D. Laurent, K. V. Lawler, S. V. Levchenko, C. Y. Lin, F. Liu, E. Livshits, R. C. Lochan, A. Luenser, P. Manohar, S. F. Manzer, S. P. Mao, N. Mardirossian, A. V. Marenich, S. A. Maurer, N. J. Mayhall, E. Neuscamman, C. M. Oana, R. Olivares-Amaya, D. P. Oneill, J. A. Parkhill, T. M. Perrine, R. Peverati, A. Prociuk, D. R. Rehn, E. Rosta, N. J. Russ, S. M. Sharada, S. Sharma, D. W. Small, A. Sodt, T. Stein, D. Stück, Y. C. Su, A. J. W. Thom, T. Tsuchimochi, V. Vanovschi, L. Vogt, O. Vydrov, T. Wang, M. A. Watson, J. Wenzel, A. White, C. F. Williams, J. Yang, S. Yeganeh, S. R. Yost, Z. Q. You, I. Y. Zhang, X. Zhang, Y. Zhao, B. R. Brooks, G. K. L. Chan, D. M. Chipman, C. J. Cramer, W. A. Goddard, M. S. Gordon, W. J. Hehre, A. Klamt, H. F. Schaefer, M. W. Schmidt, C. D. Sherrill, D. G. Truhlar, A. Warshel, X. Xu, A. Aspuru-Guzik, R. Baer, A. T. Bell, N. A. Besley, J. Da Chai, A. Dreuw, B. D. Dunietz, T. R. Furlani, S. R. Gwaltney, C. P. Hsu, Y. Jung, J. Kong, D. S. Lambrecht, W. Liang, C. Ochsenfeld, V. A. Rassolov, L. V. Slipchenko, J. E. Subotnik, T. Van Voorhis, J. M. Herbert, A. I. Krylov, P. M. W. Gill and M. Head-Gordon, *Mol. Phys.*, 2015, **113**, 184–215.

30 Q. Wu and T. Van Voorhis, *Phys. Rev. A - At. Mol. Opt. Phys.*, 2005, **72**, 7–10.

31 Q. Wu and T. Van Voorhis, *J. Chem. Phys.*, 2006, **125**, 164105.

32 Q. Wu, C. L. Cheng and T. Van Voorhis, *J. Chem. Phys.*, 2007, **127**, 164119.

33 J. Da Chai and M. Head-Gordon, *Phys. Chem. Chem. Phys.*, 2008, **10**, 6615–6620.

34 T. Brixner, R. Hildner, J. Köhler, C. Lambert and F. Würthner, *Adv. Energy Mater.*, 2017, **7**, 1–33.

35 N. J. Hestand and F. C. Spano, *Chem. Rev.*, 2018, **118**, 7069–7163.

36 S. K. Chakraborty, *Geofis. Pura Appl.*, 1956, **33**, 17-22.

37 R. Casier and J. Duhamel, *Macromolecules*, 2018, **51**, 3450–3457.

38 A. Gładysiak, T. N. Nguyen, R. Bounds, A. Zacharia, G. Itskos, J. A. Reimer and K. C. Stylianou, *Chem. Sci.*, 2019, **10**, 6140–6148.

39 J. H. Qin, Y. D. Huang, Y. Zhao, X. G. Yang, F. F. Li, C. Wang and L. F. Ma, *Inorg. Chem.*, 2019, **58**, 15013–15016.

40 A. Nakajima, *Bull. Chem. Soc. Jpn.*, 1973, 46, 2602–2604.

41 A. Sharma, D. Kim, J. H. Park, S. Rakshit, J. Seong, G. H. Jeong, O. H. Kwon and M. S. Lah, *Commun. Chem.*, 2019, **2**, 39.

42 F. C. Spano and C. Silva, *Annu. Rev. Phys. Chem.*, 2014, **65**, 477–500.

43 J. Hoche, H. C. Schmitt, A. Humeniuk, I. Fischer, R. Mitrić and M. I. S. Röhr, *Phys. Chem. Chem. Phys.*, 2017, **19**, 25002–25015.

44 P. Deria, J. Yu, T. Smith and R. P. Balaraman, *J. Am. Chem. Soc.*, 2017, **139**, 5973–5983.

45 R. D. Pensack, R. J. Ashmore, A. L. Paoletta and G. D. Scholes, *J. Phys. Chem. C*, 2018, **122**, 21004–21017.

46 J. B. Birks and L. G. Christophorou, *Spectrochim. Acta*, 1963, **19**, 401–410.

47 D. Sheberla, L. Sun, M. A. Blood-Forsythe, S. Er, C. R. Wade, C. K. Brozek, A. Aspuru-Guzik and M. Dincă, *J. Am. Chem. Soc.*, 2014, **136**, 8859–8862.

48 S. Patwardhan and G. C. Schatz, *J. Phys. Chem. C*, 2015, **119**, 24238–24247.

49 L. Sun, S. S. Park, D. Sheberla and M. Dincă, *J. Am. Chem. Soc.*, 2016, **138**, 14772–14782.

50 R. A. Marcus, *Annu. Rev. Phys. Chem.*, 1964, **15**, 155-196.

51 H. Kuroda, T. Amano, I. Ikemoto and H. Akamatu, *J. Am. Chem. Soc.*, 1967, **89**, 6056–6063.

52 W. P. Lustig, Z. Shen, S. J. Teat, N. Javed, E. Velasco, D. M. O'Carroll and J. Li, *Chem. Sci.*, 2020, **11**, 1814–1824.

53 C. Hou and H. Yu, *J. Mater. Chem. C*, 2020, **8**, 4169–4180.

54 J. Lu, W. Feng, G. Mei, J. Sun, C. Yan, D. Zhang, K. Lin, D. Wu, K. Wang and Z. Wei, *Adv. Sci.*, , DOI:10.1002/advs.202000689.

55 Y. K. Seo, J. W. Han, K. T. Lim, Y. H. Kim, C. W. Joo, J. Lee, N. S. Cho, S. Yu, M. H. Kang, C. Yun and B. H. Choi, *Org. Electron.*, 2017, **42**, 348–354.

Chapter 3: Tuned Emission from Hydrogen Bonded Framework for White Light Production

3.1 Introduction

Incandescent bulbs are a particularly wasteful method of light production.[1] Less than 5% of the electrical current passed through the filament results in visible light.[2] Despite their inefficiencies, incandescent light bulbs have effectively remained unchanged since their invention and together with fluorescent lights they still dominate many of the market sectors today. Bulbs that contain light-emitting diodes (LEDs) however are far more energy efficient.[3] They produce comparatively little heat, are more robust and last much longer than traditional filament-based lighting. Notwithstanding the benefits of LEDs, there is still room for improvement, both in light quality as well as lowering the cost and toxicity of the materials used to construct them.[4] Because no single chromophore emits white light, the fabrication of white light LEDs provides a greater challenge than monochromic LEDs.[5]

The most commonly used method for commercially available devices involves light from a blue-emitting LED exciting a phosphor layer that absorbs a portion of the blue light and reemits a lower energy emission, a form of down conversion.[6] Blue and yellow light blend to make what our eyes perceive as white light (see Fig 1).

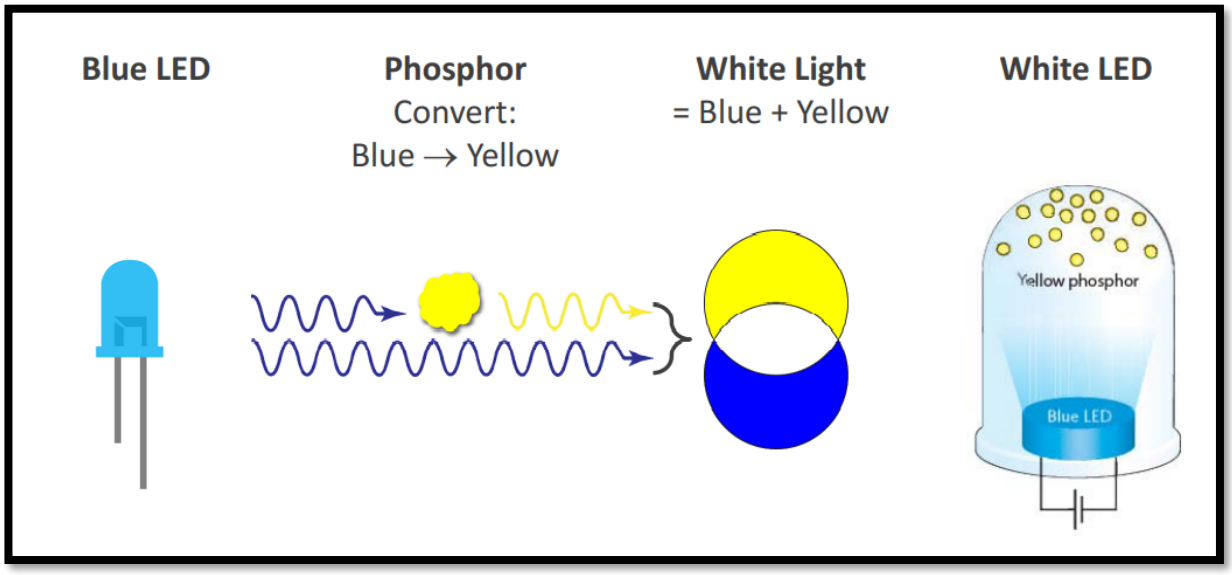

Fig. 1. Method for producing white LEDs. Blue-emitting LED exciting a down-conversion phosphor material to produce white light.

Materials used in these devices consist of a blue-emitting LED, usually made from indium gallium nitride (InGaN), coupled with a yellow phosphor powder, most commonly a yttrium aluminum garnet (YAG), such as $Y_3Al_5O_{12}$, doped with Ce^{3+}.[7] In another design, multiple chromophores that emit blue, green and red light are combined and excited to produce white light.[8] This approach however is more expensive and complicated than the first method and the overwhelming majority of commercially available white LEDs employ a blue LED combined with a yellow phosphor material to achieve white light emission.

Researchers are always developing new photo and electro-luminescent materials to produce white light that faithfully mimics natural light. The "color rendering index" (CRI),[9] Commission International de l'Eclairage coordinates (CIE)[10] and correlated color temperature[11] are metrics often used to quantify this property. The "quality" of white light is one area that incandescent bulbs outperform LEDs. The primary reason for this is that incandescent bulbs, like the sun, are black body radiators that emit a wide region of the visible spectrum.[12]

Considerable advances in the last two decades in organic light emitting diodes (OLEDs)[13] has seen this research move from the lab to the marketplace, particularly for use in high resolution displays. Current growth statistics predict OLED based devices will begin to dominate the next generation of consumer electronics by the end of the decade.[14] On a molecular level it is organic semiconductors consisting of π conjugated oligomers and polymers that produce the light in these devices.[15]

The use of porous crystalline frameworks as phosphor materials[16] is actively being explored due inherent advantages in relation to their tuneability[17] and ability to form composites.[18] Metal organic frameworks have been the focus of this research with over 1300 luminescent MOFs being reported by mid-2019.[19] A common theme with luminescent framework material based studies is the fact that their photo emission is a function not only of their composition but also of their structure.[20] The source of light emission in these materials is varied. It can originate from the linker,[21] from the metal nodes[22] or in many cases from a guest molecule or guest complex.[23] An example of the later for the production of white light was achieved by the encapsulation of a yellow emitting iridium complex within a porous blue-emitting MOF, $[(CH_3)2NH_2]_{15}[(Cd_2Cl)_3(TATPT)_4].12DMF.18H_2O$.[24] Optimization studies revealed that the use of a 3.5wt% of Ir^{III} complex confined in the pores of the MOF offered the highest value of quantum yield (20.4%), with exceptionally good white light quality (CIE coordinate values of 0.31, 0.33). In this case the desired optical properties were achieved but the key material used, iridium, is one of the rarest elements in the Earth's crust and its price has more than doubled over recent years.[25] The cost of materials in addition to the expense of the multiple step fabrication process (ligand synthesis, complex synthesis, MOF synthesis,

encapsulation process, device fabrication, etc.) may mean this method for white light production would prove difficult to scale up in a cost effective manner.

There is mounting evidence that suggests that the emissive properties MOFs offer, including a wide color gamut, negligible self-quenching (not in all cases but in many due to the relatively large intermolecular separations of fluorophores inside the porous structures), and distinct fluorescence energies (on account of the unique energy conformations inside the structures), could potentially see them replace the current generation of semiconducting materials such as silicon, germanium, and gallium arsenide.[26]

Compared with luminescent MOF research, which is a relatively new field that has now gained considerable traction, investigation into using hydrogen bonded frameworks (HOFs) as phosphor materials[27] is still in its infancy. Hydrogen bonded organic frameworks[28] are a class of crystalline material generally constructed from monomers containing electropositive hydrogen atoms as donors and electronegative oxygen or nitrogen atoms as hydrogen bond acceptors. Hydrogen bond formation resulting in crystalline materials has been well documented in supramolecular chemistry.[29] The topology of HOFs is heavily reliant on the shape and steric bulk of the ligands, π orbital interactions as well as solvent polarity. The simplicity of forming hydrogen bonded materials, the absence of toxic metals and their ability to easily regenerate from a simple recrystallization process has seen HOFs intensely studied for their potential applications in catalysis,[30] gas storage/separation[31] and biotechnology.[32] Their potential as tunable luminescent materials has been largely unexplored.

One of a handful of reported luminescent HOF materials is T12-apo.[33] Like many luminescent framework materials, the core of the ligand contains a flat, aromatic molecule (Nu-T12, see Fig 2a). Functionalized with 6 carboxylic acid groups the C_3-symmetric π-conjugated planar ligand can form isostructural H-bonded 2D hexagonal network sheets that then stack to form the HOF. Permanently porous with triangular voids, the resultant HOF displays interesting luminescent properties.

Time resolved fluorescence microscopy reveals the importance of π-π stacking of the aromatic core and of H-bonding interactions to form the HOF, and their relevance to its photobehaviour. The nature of the crystal packing is key in the photoemission for T12-apo. The S0 -> S1 transition of the building blocks which is forbidden when the monomer is dissolved in DMF becomes allowed in the HOF and in turn results in a high quantum yield value of 25% for the desolvated crystalline material.

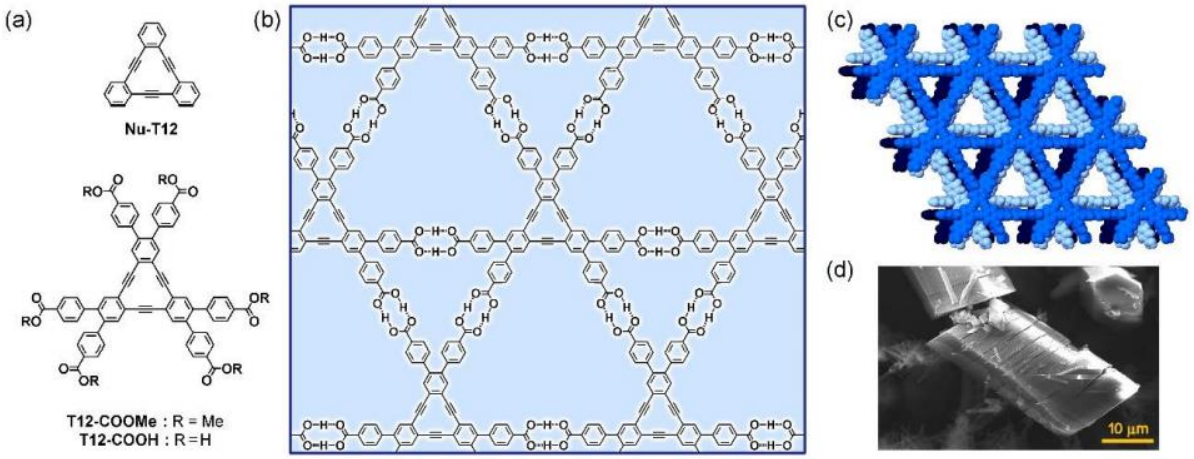

Fig 2. (a) Molecular structures of Nu-T12, T12-COOMe and T12-COOH that constitute the units of the studied materials. **(b)** Illustration of the H-bond interactions between the molecular units of T12-apo HOF. **(c)** Top view of three-layer packing of T12- apo**. (d)** SEM image of T12-apo. (*J. Mater. Chem. C*, 2018, **6**, 6929-6939).

The stability of a porous crystalline framework has always been an important feature in the advancement of new materials and with this in mind, hydrogen bonded frameworks (HOFs) have often been overlooked by some researchers reasoning that their novel materials would be far more robust with the use of metal centers to form MOFs. Recent work has shown however, the use of aromatic linkers can result in π orbital interactions that can considerably contribute to the overall stability of a 3D co-ordination polymer.[34]

An outstanding example that is considerably more stable than many MOFs is the previously reported HOF, PFC-1.[35] Relying solely on hydrogen bonding and π orbital interactions for its crystallinity, it exhibits permanent porosity, high surface area and excellent chemical stability. The crystallinity and porosity of PFC-1 maintain intact upon boiling in water for 10 days or following being soaked in methanol, acetone, and deionized water for 117 days. Computational analysis clearly indicates significant pyrene-pyrene π orbital interactions that are responsible for the exceptional stability of this material.

In this study, 4,4',4'',4'''-(1,3,6,8-Pyrenetetrayl) tetrabenzoic (TBAPy) was used as the organic linker to form previously reported HOF PFC-1. Although research about the structure and porosity of this HOF was published in 2018, no spectroscopic studies on this material had been undertaken to date. Based on its structure and composition I suspected that interchromophoric interactions and lattice induced red shift manifested by crystal packing may make it a suitable candidate for a yellow emitting phosphor layer for use in a white LED in the manner described above.

Utilizing crystal engineering to fine tune the emissive properties of materials as a function of their topological net as opposed to altering their chemical structure via synthesis provides an approach that has meaningful value in the field of optoelectronics. In the case of PFC-1 I suspected to find a considerable shift from the free linker in solution in the energy of the emission due to close positioning of pyrene locked within the framework (less than 4 Å). The close spacing of TBAPy also results in a very high chromophore density. Combined with reduced rotational and vibrational freedom as result of the close packing of 2D sheets, enhanced photo luminescence quantum yield (PLQY) for the dry material under ambient conditions should be evident in the experimental data.

The close stacking of the TBAPy physically prevents the benzoate groups being able to rotate. This is an important structural consideration as the steric impediment of rotational freedom has been documented in many cases to significantly enhance the quantum yield of chromophores that contain rotational groups.[36] A simple example is shown below in Fig. 3.

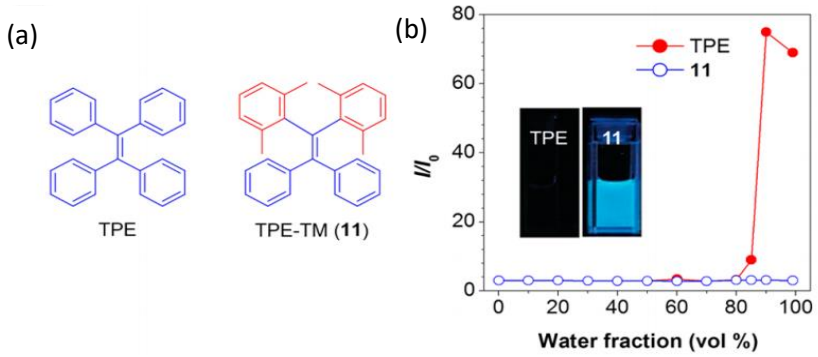

Fig 3. (a) Molecular structures of TPE and TPE-TM (11). **(b)** Plots of I/I_0 of TPE and TPE-TM (11) vs water fractions in THF/water mixtures (10 μM), where I_0 and I the PL intensities in THF solution and a THF/water mixture, respectively. Inset: photographs of TPE and 11 fluorescing in THF solutions. (*Chem. Rev.* 2015, **115**, 11718–11940).

Intramolecular steric hindrance prevents excited state energy from dissipating due phenyl ring rotation and promotes radiative decay pathways. This phenomenon helps to explain the results of quantum yield experiments discussed in the next section.

Another important consideration when examining the photo emission profile of desolvated materials is aggregation effects. Aggregated induced emission (AIE)[37] is a general term applied to solid luminescent materials that have a have a marked difference in optical properties compared to that of the monomer in solution. With AIE the intensity of the emission is enhanced. An example outlined in the chapter 1, PCN-

94, has a remarkable increase in PLQY (from 30% to 90%) when compared to its ligand in dilute solution.[38] The crystallizing of a luminescent monomer can act to lock freely rotating or vibrating molecules in position. With the molecule unable to dissipate excited state energy through heat (molecular vibration and rotation), photon emission is enhanced considerably.

Aggregation caused quenching (ACQ),[39] a phenomenon first reported in 1954 by Forster *et al,* is more likely to be the result of aggregating of luminescent molecules and is why most dry material has negligible quantum yield. ACQ occurs when the close spacing of chromophores in a crystal or aggregate, in particular flat aromatic molecules, results in π orbital overlap that provide non-radiative pathways for energy dissipation.

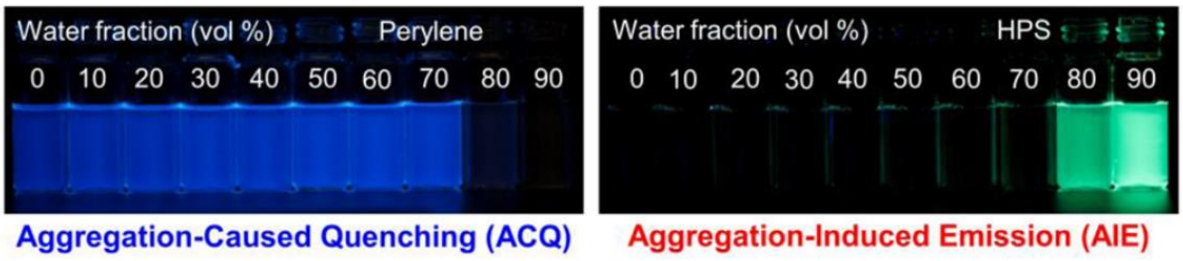

Fig. 4. Fluorescence photographs of solutions or suspensions of (left) perylene (20 μM) and (right) hexaphenylsilole (HPS; 20 μM) in THF/ water mixtures with different fractions of water (fw), with perylene and HPS showing typical ACQ and AIE effects, respectively. (*Chem. Rev.* 2015, **115**, 11718–11940).

The diversity of optically active ligands that can be functionalized with hydrogen bonding groups, should allow HOFs such as the one out-lined in this work to realize enhanced luminescence functionality in the areas in solid-state lighting,[40] luminescence-based sensors[41] and other electrochromic devices.[42]

Herein, I report on the unique photophysical properties of PFC-1 and introduce a method to achieve high quality white light from a LED or an organic LED (OLED) device using a purely organic luminescent HOF. To further fine tune the emissive properties of the device to the desired chromaticity co-ordinates I doped the HOF with naturally occurring beta-carotene (β-Carotene). The result: a quality of white light equivalent to that of commercially available devices but from a yellow phosphor material that contains no metals, lanthanides, rare earth or toxic materials. This is the first report of luminescent HOF being used as a yellow emitting down-conversion material in a working white light LED device.

3.2 Results and Discussion

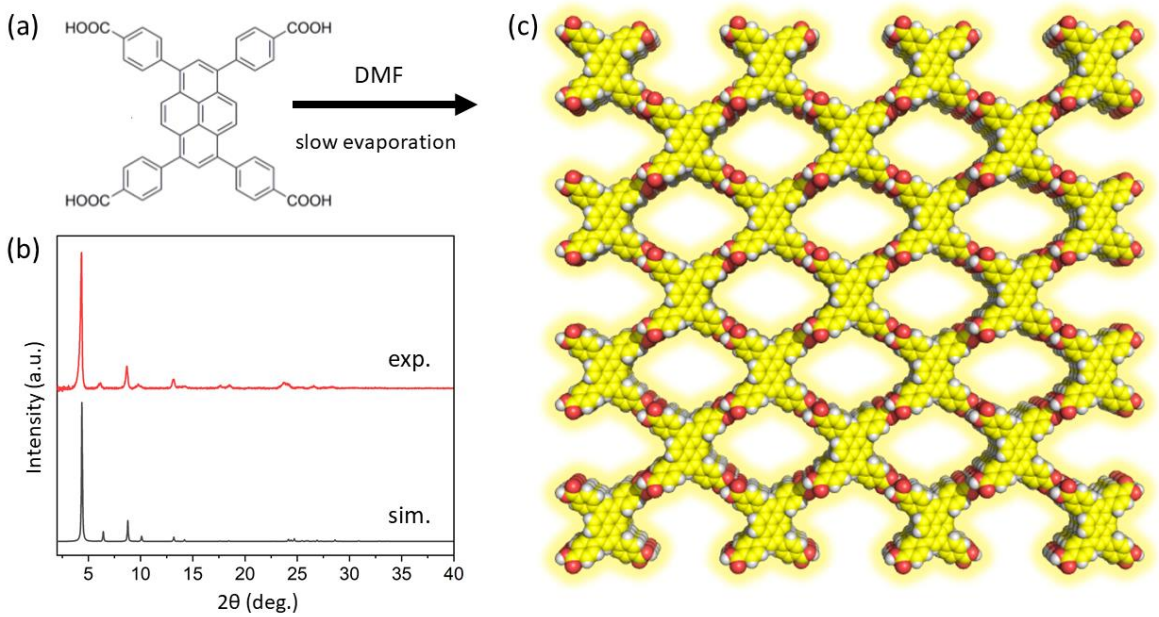

Fig. 5. (a) TBAPy ligand **(b)** PXRD pattern of PFC-1 simulated (red) and experimental (black) and **(c)** 3D molecular structure of PFC-1 obtained by single crystal x-ray diffraction (oxygen: red, carbon: yellow, hydrogen: white).

Structural Analysis

The structure of photoactive crystalline materials is relevant when trying to predict how the emissive nature of a chromophore contained within the lattice may behave. PFC-1 readily crystalizes from DMF via evaporation into a stable microcrystalline, non-interpenetrated HOF. SCXRD experiments conducted by the group that first reported this material reveals 2D sheets of hydrogen bonded TBAPy molecules stack at a distance of 3.34 Å (distance of two closest carbons atoms on adjacent pyrene moieties).[43] This was confirmed my own SCXRD structural analysis. Voids measuring 18Å by 23 Å (see Fig. 5) run the length of a single axis resulting in permanent porosity with a calculated BET surface are of 2122 m^2g^{-1}. PCF-1 crystalizes into the monoclinic space group I2/m and the asymmetric unit consists of a single benzoate group and four carbon atoms belonging to the pyrene centre.

At 2.603 Å (O-O) the lengths of the hydrogen bonds fall within the range of what would be considered strong hydrogen bonds. The intermolecular potentials of the 3 strongest interactions between ligands show that the π rich aromatic systems contribute significantly to the stability of this material. The two

closest ligands have an intermolecular potential of -206 kJ/mol, considerably more than that of the combined hydrogen bonds for each ligand (see Fig. 6). When combined with the other intermolecular potentials of neighbouring ligands the sum amounts to a substantial force that acts to bind the structure together. This is an important feature of the composition. If PFC-1 was to rely solely on hydrogen bonding interactions to retain its form, its structural stability would be severely compromised and it's unlikely it would survive desolvation. The phase purity of bulk microcrystalline and nanocrystalline PFC-1 was confirmed by powder X-ray diffraction (PXRD) analysis.

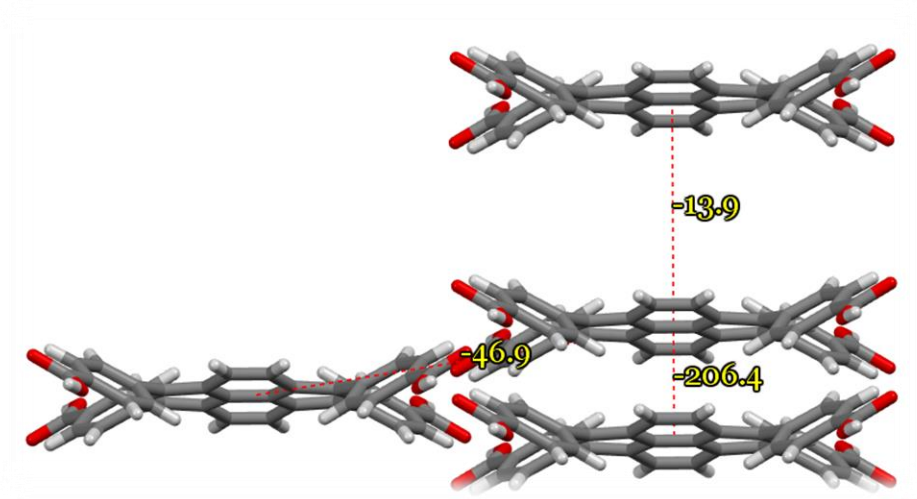

Fig. 6. The three strongest intermolecular potentials (in kJ/mol) between neighbouring ligands calculated using a UNI force field.

TBAPy occupies a single chemical environment with all four carboxylic acid functional groups retaining their hydrogen atom and hydrogen bonding to four other ligands. Each unit cell (3041.55 $Å^3$) contains four TBAPy molecules resulting in a calculated TBAPy density throughout the framework of 2.18 mol/dm^3, the highest recorded for any TBAPy based crystalline framework.

Because I was interested in the optical output of this material the last two structural features mentioned are of particular importance. If the ligand were to occupy multiple chemical environments within the lattice, various electronic configurations of the chromophores would be present and potentially a more complicated emission spectrum with overlapping absorption and emission profiles would arise. Secondly, the high chromophore density should help to enhance luminescence.

Spectroscopic Study PFC-1

Pyrene is one of the most well-known polycyclic aromatic hydrocarbons and its four fused rings result in a flat structure with a well-defined absorption and emission profile making it ideal for use as a fluorescent probe in bio-imaging applications.[44] Organic building units of H_4TBAPy synthesized through a Suzuki coupling reaction extend the aromaticity of pyrene and red shift both the solid-state absorption and emission spectrum. The self-assembly of H_4TBAPy chromophores into PFC-1 augments the spectral signature due to the proximity of the chromophores to each other. As a result, phenomena such as lattice induced energy transfer,[45] exciton delocalization[46] and strong intermolecular coupling[47] lead to broadening and a further red shifted emission.

Pyrene is well known for being extremely sensitive to its chemical environment.[48] I opted to run the spectroscopy experiments of PFC-1 on dry microcrystalline material to (a): remove the effects of solvent polarity on the transition energies of our optically active HOF and (b): gather data that more accurately reflects how the material would behave in a device in which the chromophore would not be solvated.

Solid-state absorbance shows well-defined peaks and troughs ranging from 225 nm to 450 nm with a max at approximately 405 nm. Strong absorption in the blue region of the spectrum results in the material appearing pale yellow under ambient light.

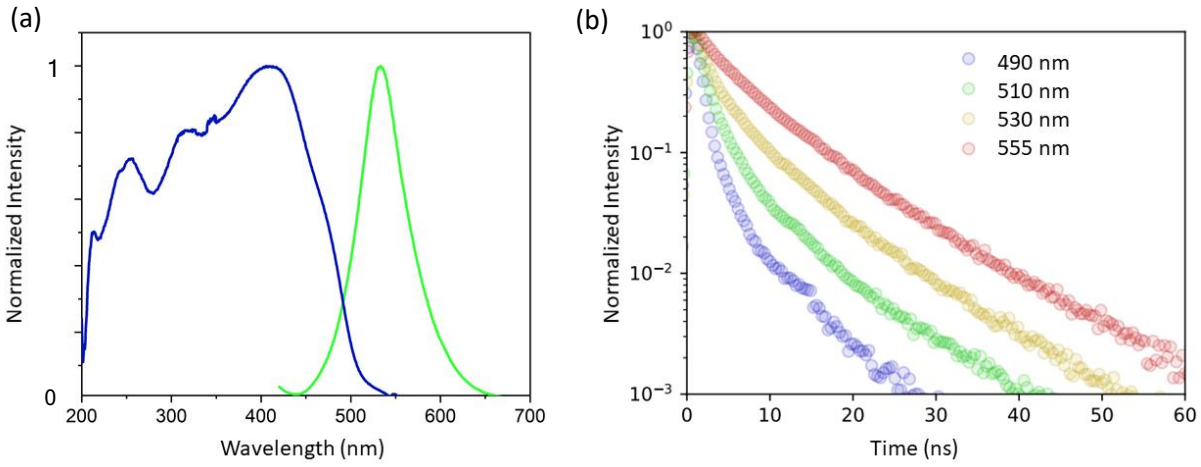

Fig. 7. (a) Normalized solid state absorption (blue) and emission (green) (ex. 405 nm) profiles for PFC-1**. (b)** Time-resolved fluorescence kinetics at different detection wavelengths for PFC-1 (ex.405 nm).

Solid-state excitation and emission spectra for PFC-1 reveal a peak centered at 535 nm (ex 405 nm), considerably red shifted from the free linker in solution (447 nm). With the max emission at 535 nm the unusually large Stokes shift (approx. 100 nm) results in minimal overlap between the excitation source and the fluorescent emission. The dry material fluoresces strongly under UV irradiation in the solid state (see Fig S5).

Recent work published by researchers interested in how topology dependant interactions augment the photophysical properties of MOFs indicate the strong link between crystal structure and optical properties.[49] They reveal changes in topology have significant effects on the emissive nature of these photoactive co-ordination polymers. As frontier orbital systems of adjacent linkers are both aligned and positioned closer together an increasingly red-shifted emission profile becomes evident. An example is the difference in maximum emission wavelength between previously reported NU-1000 which contains TBAPy linkers spaced on an angle at 10.94 Å,[50] producing max emission at 455 nm and ROD-7 containing TBAPy stacked in an eclipsed orientation at 8.76 Å,[51] resulting in a considerably redshifted emission at 525 nm (max).

The time resolved spectral data for PFC-1 reveals substantially different kinetics at each detection wavelength, with noticeably faster decays at shorter wavelengths; however, there is no simple first order decay component to the traces. The varying decay rates at different wavelengths are indicative of energy transfer within the lattice, a result of very closely positioned and overlapping π orbitals. Exciton migration and charge transfer as result of closely stacked aromatic molecules that contain extensive π orbital systems is well documented.[52] Computational work outlined in Chapter 2 clearly indicates this process is active in similar TBAPy based materials.

An important structural feature that has the potential to influence the spectral signature of PFC-1 is the orientation of the ligands with respect to one another. The parallel, eclipsed alignment of the pyrene in PFC-1 can result in destructive interference of the transition dipoles in the first excited state (the transition dipole in the ligand points along the long axis of pyrene, which results in the first-excited state being non-emissive). This is typical behaviour for a H-aggregate where the chromophores are positioned in a parallel, eclipsed orientation.[53] With the eclipsed arrangement of the chromophore pairs suppressing the 0–0 vibronic transition and leaving the 0–1 peak to dominate, it serves to reveal further why the emission of the HOF is so significantly red shifted.

Finally, we conducted quantum yield measurements on the HOF. It was discovered that PFC-1 has a relatively high quantum yield compared to similar materials. Photo luminescent quantum yield (PLQY) measurement were conducted on dry, nano crystalline PFC-1 using an integrating sphere with a laser excitation source. This experiment examining quantum yield in the solid state found it to have a PLQY of 22%. For comparison, zirconium-based MOF NU-1000, that employs TBAPy as the linker has a quantum yield of 5% in the dry state.[54] The reason for the high PLQY we attribute to (a); the very high chromophore density and (b); the increased rigidity and reduced rotational freedom of the linkers as a result of being incapsulated within a crystalline lattice. In addition to multiple hydrogen bonds locking the ligands in position, repulsion between H atoms on adjacent phenyl groups decreases the thermal motion of the rings and allowing the excited linker to release the energy through fluorescence. In fact, in the case of PFC-1 the proximity to adjacent linkers makes it physically impossible for the benzoate groups to rotate.

The results of our spectroscopy experiments when referenced against structural data suggest that both AIE and ACQ are occurring simultaneously. There is a significant drop in the PLQY in dry PFC-1 from that of TBAPy in solution from 85% to 22% (a result of non-radiative pathways within the lattice, confirmed by time resolved spectroscopy and SCXRD); however, there does seem to be some form enhancement when compared to NU-1000 which has a particularly low quantum yield (5%) with its ligands spaced such that phenyl ring rotation is not obstructed.

Photoluminescence quantum efficiency is one of the key parameters of phosphors for use in white LEDs. Particle size is also an important consideration and is ideally in the nanoscale to help reduce scattering, increase quantum yield, and improve processability when mixed with dopants or encased in resins. While typical fluorescent materials do not undergo as significant O_2 quenching as phosphorescent materials do (due to the spin-forbidden energy transfer from the former to the triplet ground state of O_2), we suspect the fact that PFC-1 is a porous material results in some level of quenching by O_2 and other potential quenchers present in ambient air (e.g., CO_2 and H_2O). Although we did not conduct our experiments in an O_2 free environment, previously work published on luminescent porous crystalline frameworks, report up to a 24% increase on PLQY upon N_2 de-aeration.[55] Further studies in oxygen free environments may have seen an increase in PLQY for PFC-1.

3.3 Device Fabrication and Optimization

The value of the maximum emission (535nm) in addition to the broad emission spectrum (~450nm to 650 nm) and relatively high PLQY prompted us to investigate the viability of PFC-1 for use as a phosphor in a white LED. There are many reported porous crystalline frameworks formed from TBAPy.[56,57,58] The majority of these are MOFs that use a variety of metal nodes to engender a multitude of different topologies. Spectroscopic studies have found that the distance and orientation of the chromophores relative to each has marked impact on the spectral signature of the material. The ability to alter the electrical and optical properties of a chromophore, such as TBAPy, by deliberately inducing interchromophoric interactions within a crystalline lattice is the technique that can be applied to achieve the desired emission spectrum. It was found in the work published in Chapter 2 that the close spacing or "stacking" of pyrene in a co-facial orientation less than 4Å significantly redshifted the emission of the material. Although no detailed spectroscopic studies had been done on PFC-1 prior to this work, I hypothesized that the very close spacing of the TBAPy ligands relative to each other would result in a considerably red-shifted emission profile that combined with its absorption profile would make it a suitable candidate as a yellow phosphor material when excited by blue light. The spectroscopy experiments confirmed this.

As can be seen in Table 1, previously reported crystalline materials containing TBAPy fluoresce at considerably different wavelengths. Although they all contain the same chromophore, by using crystal engineering, distinct optical properties can be generated without the need for chemically modifying the chromophores.

Undoubtedly the nature of the metal nodes has an impact on the optoelectronic properties of MOFs containing luminescent ligands. However, it is obvious that an important consideration in predicting the spectral profile of crystalline materials containing chromophores is the distance and orientation of the chromophores from each other. Chromophores stacked closely (<4 Å) in a co-facial "eclipsed" orientation result in interchromophoric interactions that include but are not limited to the suppression of vibronic transitions due to alignment of transition dipoles, excimer like coupling of chromophores, exciton delocalization and energy transfer that can all have a marked impact on the energy of the emission profile.

Table 1: Max emission of previously reported crystalline porous frameworks containing TBAPy (red stars indicate this work).

MOF/HOF	Maximum Emission (nm)	Distance (Å)	Orientation (*)
NU-1000	455	10.94	NE
NU-901	518	9.52	NE
ROD-7	525	8.76	E
Cd-TBAPY	480	4.28	NE
Bi-TBAPY	490	11.08	NE
K-TBAPY ★	515	3.86	E
Na-TBAPY ★	490	3.93	NE
PFC-1 ★	535	3.34	E

(*) **E**=ligands are in eclipsed orientation **NE**=ligands are not eclipsed.

Initially I constructed a device made from a UV LED emitting at 405nm coated in PFC-1. The process for the fabrication involved dip coating then drying a commercially available LED in a suspension of the nano PFC-1 (see SI for more details about device fabrication). When a voltage is applied, a portion of the UV light emitted by the LED is absorbed by the HOF which then reemits a lower energy broad band emission spanning a large portion of the visible spectrum. The UV powered device functioned well and an emission centred at 535nm (ex. 405nm) subsequent from PFC-1 excitation was clearly evident (see Fig 8). Although the emission max (535nm) of the nano-PFC-1 used in the UV powered device is identical to that of the micro crystalline PFC-1 examined in the initial study, the emergence of more well-defined bands the lattice can clearly be seen in Fig 8 at 570nm and 625nm.

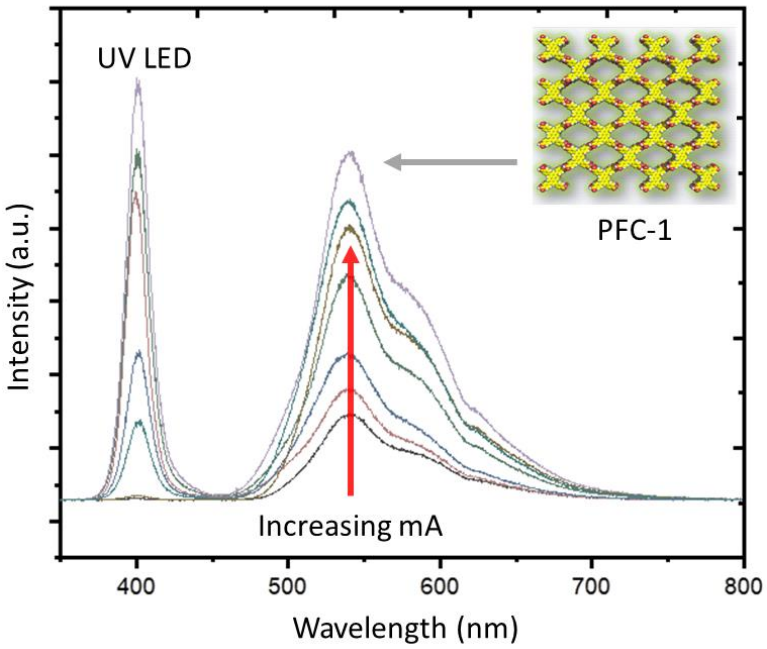

Fig. 8. Emission spectrum of a test device fabricated by coating a commercially available UV (405nm) LED with PFC-1. Recorded with increasing amperage.

With our proof-of-concept successful I constructed another device consisting of a standard blue emitting LED with a maximum emission centred at 468nm. I then coated the blue LED in PFC-1. I set about optimizing the device by changing the amount of PFC-1 used to coat the LED (see Fig S3). For pure white light, the chromaticity co-ordinates should be as close as possible to (0.31, 0.31). Despite the wavelength of light being easily tuned simply by increasing or decreasing the amount of HOF, I was unable to tune the CIE coordinates to match those of commercially available white LED devices by this method. Our devices measured a spectrum deficient at longer wavelengths resulting in a "cold" white light (white light with a blueish tinge – see Fig S4). The max emission of the HOF at 535nm is ideal; however, the spectrum quickly drops off and limited emission at the red end of the spectrum means regardless of the amount of optimization relating to the ratio of blue light to HOF emission, there is not enough longer wavelength light to produce a warm white light.

PFC-1 is one of the very few permanently porous HOFs reported to date. It has large open pores (18x23Å) lined entirely with slightly positively charged hydrogen atoms running the length of a single axis. With this

in mind I decided to dope the material to augment the spectrum in order to generate a higher quality "warm" white light (closer to CIE coordinates 0.31, 0.31). I evaluated several options for a dopant. Complexes containing rare earth elements such as iridium and rubidium are well known for emitting in the lower energy end of the visible spectrum and have been successfully encapsulated into the pores of MOFs.[59] I dismissed this option because these elements are not ecologically sound. Organic polymers such as MEV-PHH are commonly used as the red-light emitting component of OLEDs,[60] however, these materials are expensive (>$800 per gram). Another option was red emitting quantum dots. Quantum dots have been successfully infused into the pores of porous coordination polymers previously,[61] however, most quantum dots are made from rare earth elements, are particularly toxic and too large to fit within the pores of PFC-1.

To find the simplest, and most eco-friendly solution I decided the naturally occurring molecule beta-carotene (β-Carotene) may possess the attributes I were looking for. β-Carotene is an organic, strongly coloured red-orange pigment abundant in fungi, plants, and fruits.[62] It is a member of the carotenes, which are terpenoids, synthesized biochemically from eight isoprene units and thus having 40 carbons. Among the carotenes, β-Carotene is distinguished by having beta-rings at both ends of the molecule.

The absorption profile of β-Carotene is well documented[63] (obtained by us experimentally and presented in Fig. S5). It shows strong absorption in the lower wavelengths with a sharp drop off at 550nm and negligible absorption above 600nm. Its emission profile, like may chromophores, varies depending on the environment of the molecule. In solution, β-Carotene has a low quantum yield due to the fact almost all the absorbed light can be converted into vibrational energy due to its flexibility and conformational freedom. I hoped β-Carotene would absorb some of the PFC-1 emission in the 500-550nm region augmenting the spectrum to present a relatively stronger emission at the red end of the spectrum (550-700nm) without having a marked impact on the overall luminosity.

In terms of combining PFC-1 with β-Carotene several methods were evaluated and then attempted including co-crystallization[64] and incipient wetness impregnation.[65] Both of these methods were an attempt to take advantage of the porosity of the HOF and have β-Carotene encapsulated into the pores where potentially (a): its conformational freedom may be reduced leading to enhanced optical properties and (b): it would be protected from oxidation. The successful of encapsulation of β-Carotene into carbon nanotubes served as partial inspiration for examining this approach.[66] In terms of augmenting the emissive spectrum of the HOF however these methods proved not to produce the desired properties. The best

results were achieved by simply mixing the HOF and β-Carotene in solution and then evaporating the solvent into a composite material. To what extent the β-Carotene may have encapsulated into the pores of the HOF was not explored in detail as the methods that would promote encapsulation seemed to have the least impact on the spectrum. The effect on the spectrum which can be seen in Fig 9 is to reduce the strength of the emission in the 500-570nm range (the result of β-Carotene absorbing at this wavelength). The band at 600nm now becomes the prominent emission wavelength.

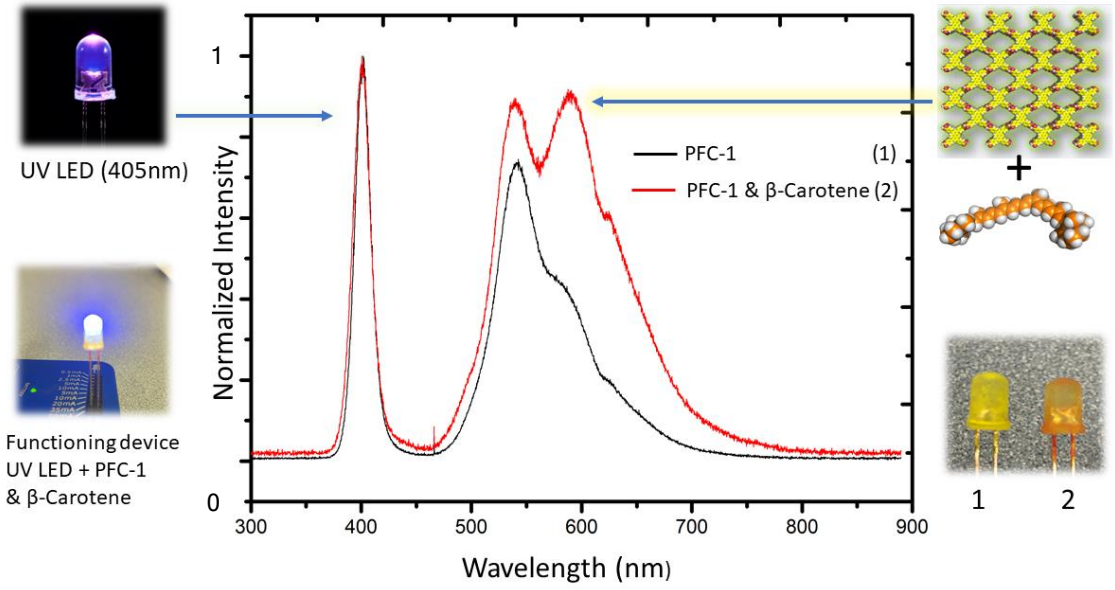

Fig. 9. Normalized emission spectrum of a test device fabricated by coating a commercially available UV (405nm) LED with PFC-1 (black) (1) and not yet optimized PFC-1(β-Carotene) (red) (2).

With a greater portion of the spectrum now emitting in the 570-750nm range of the spectrum the chromaticity co-ordinates, when combined with that the blue LED light (468nm), are shifted to very close to that of commercially available white LED devices (see Fig 10b).

For our final optimized device, I was able to achieve (CIE 1931) chromaticity co-ordinates and correlated colour temperature of (0.29, 0.33) and 7832K, respectively. The composite material PFC-1(β-Carotene) performed exceedingly well at achieving the light emission at the desired wavelengths. Further refinements in the fabrication process and the amount of HOF/dopant could see these properties improve.

Although the white LED fabricated in this work using PFC-1(β-Carotene) uses a commercially available indium gallium nitride blue LED, a purely organic device made from a blue emitting organic polymer could certainly be used to produce the appropriate wavelength light for an organic white LED made solely from carbon, oxygen and hydrogen.

An anomaly that appeared in the spectrum of the final fabricated device can be seen in Fig. 10a as an emission peak 495nm (ex. 468nm). Although this emission does not adversely affect the performance of the device its origin is unclear. More puzzling is that emission vanishes when the excitation wavelength is lowered to 400nm.

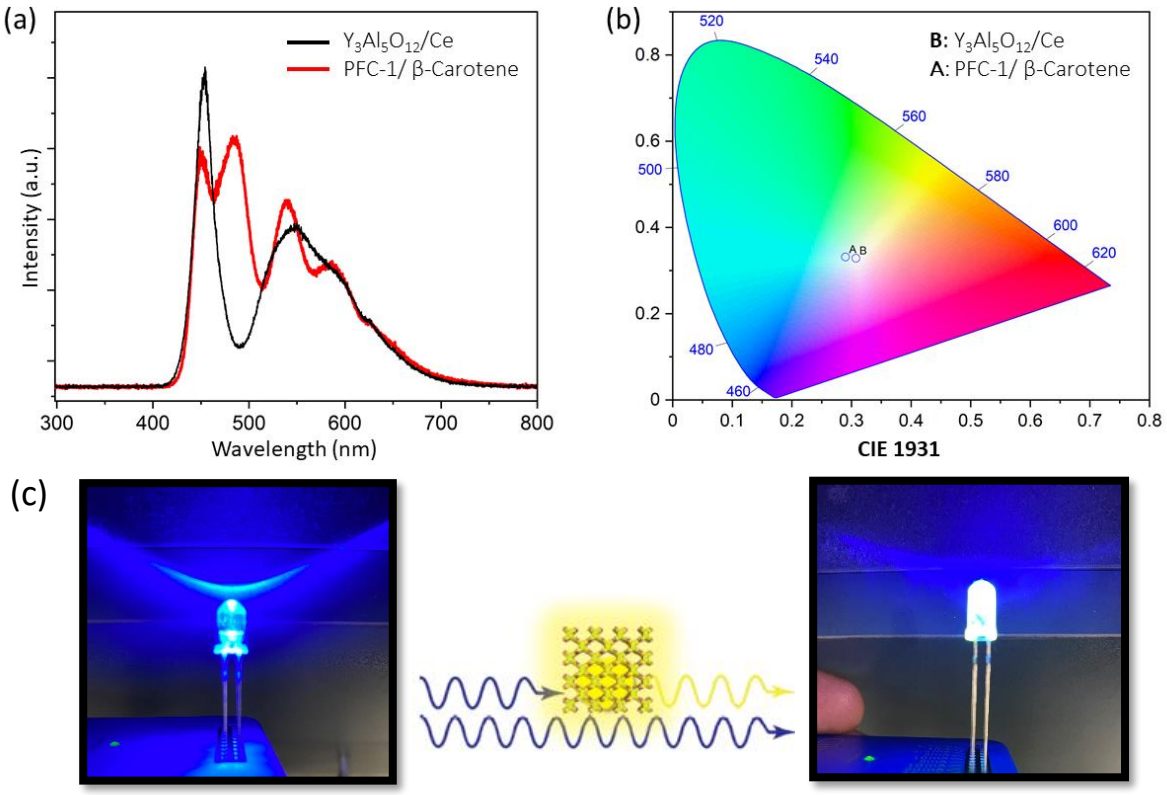

Fig. 10. **(a)** Experimental spectrum of commercially available white LED (black) and our device: PFC-1(β-Carotene) doped LED (red) and **(b)** CIE-1931 chromaticity diagram. The CIE coordinates (marked by circles for the various devices) are *A*: our device (PFC-1/β-carotene phosphor) 0.29, 0.33 for *B*: commercially available white LED, ($Y_3Al_5O_{12}$/Ce phosphor material) 0.31, 0.33. **(c)** Functioning blue LED before and after treatment with PFC-1(β-Carotene).

Experiments performed on PFC-1 contained in a glass capillary at the same excitation wavelength (468nm) do not result in the emission at 495nm. This peak appears to be a result of the LED device fabrication process. Although the nano-PFC-1 formed in solution is used to coat the LED, it is likely that uncrystallized ligand also exists in solution which when dried quickly under in the coating process forms a layer of TBAPy that may be responsible for emission at 495nm. Attempts to create an amorphous dry powder made from TBAPy in order to compare the spectrum was unsuccessful. The crystalline structure of PFC-1 appears to represent a global thermodynamic minimum and regardless of the conditions used (close to 100 attempts conducted over several years) to remove solvent from a solution of TBAPy no other structures were able to be reproduced. The origin of this emission is currently under investigation.

3.4 Conclusion and Future Directions

In this work have successfully taken advantage concepts relating to crystal engineering to engender a desired topology leading to a specific emission profile: (CIE 1931) chromaticity co-ordinates and of (0.29, 0.33) for the optimized device with the organic yellow phosphor material exhibiting a PLQY of 22% under ambient conditions. The structural and spectroscopic data indicate that the optical properties of a chromophore, in this case TBAPy, can be significantly altered for specific applications by its crystallization into a closely stacked hydrogen bonded framework (PFC-1). By examining in detail how the structure of framework materials alters the optoelectronic properties of luminescent molecules, a methodology can be developed that uses crystal engineering as opposed to synthesis to achieve desired optical attributes.

Research that follows on from this work has the potential, in the future, to produce low cost, non-toxic luminescent materials for the next generation of white light LEDs. Although PFC-1 contains environmentally benign elements (carbon, oxygen and hydrogen) the synthesis of the TBAPy molecule used to form PFC-1 does use rare and precious metal catalysts to couple to benzoate groups to the pyrene and further work needs to be done to ensure green synthetic methods are employed. The development of efficient, environmentally benign solid-state lighting with long-operational lifetimes could have a crucial impact on energy consumption and the sustainability of LED manufacturing.

Although the beta carotene dopant I used as a proof of concept to augment the spectral profile of our device worked well it is unlikely this would be a suitable material for a long-lived device. Beta carotene is known to undergo oxidation on exposure to UV light and although the excitation wavelength of our device

is not in the UV region of the spectrum, longevity experiments may well reveal a spectral shift over time if the beta carotene is not protected from oxidation.

In our prototype device the doped HOF is exposed to atmospheric O_2 which has the potential to both lower quantum yield and oxidize the beta carotene. Further device development would see the phosphor material encapsulated in a transparent resin to protect it from degradation (like commercially available LEDs). Overall luminosity experiments on the fabricated devices would also help quantify to what extent the beta carotene effects the overall output of the LED. This is the first time a porous fluorescent HOF has been used in the fabrication of a functioning white light LED.

Additional Information

For the work presented in Chapter 3 CNC led the conception and design of the experiments and was primarily responsible for collecting crystal structures, solid state absorption and emission data, device fabrication and optimization, drafting and revising the manuscript. PCT was involved in the acquisition of time resolved spectroscopic data, analysis and interpretation. TDP was responsible for the collection PLQY data.

3.5 References

1 B. Gayral, *Comptes Rendus Phys.*, 2017, **18**, 453–461.

2 J. H. Jou, H. H. Yu, F. C. Tung, C. H. Chiang, Z. K. He and M. K. Wei, *J. Mater. Chem. C*, 2017, **5**, 176–182.

3 H. Sasabe and J. Kido, *Chem. Mater.*, 2011, **23**, 621–630.

4 S. R. Lim, D. Kang, O. A. Ogunseitan and J. M. Schoenung, *Environ. Sci. Technol.*, 2011, **45**, 320–327.

5 D. Di Martino, L. Beverina, M. Sassi, S. Brovelli, R. Tubino and F. Meinardi, *Sci. Rep.*, 2014, **4**, 1–5.

6 Z. Wang and A. Meijerink, *J. Phys. Chem. Lett.*, 2018, **9**, 1522–1526.

7 L. C. Chen, W. W. Lin and J. W. Chen, *Adv. Mater. Sci. Eng.*, 2015, **2015**, 1–6.

8 C. C. Lin and R. S. Liu, *J. Phys. Chem. Lett.*, 2011, **2**, 1268–1277.

9 Y. Ma, L. Zhang, T. Zhou, B. Sun, Y. Wang, J. Kang, P. Gao, J. Huang, F. A. Selim, C. Wong, M. Li and H. Chen, *J. Mater. Chem. C*, 2020, **8**, 4329–4337.

10 J. Long, Y. Wang, C. Ma, X. Yuan, W. Dong, R. Ma, Z. Wen, M. Du and Y. Cao, *RSC Adv.*, 2017, **7**, 19223–19230.

11 J. Yu, H. Lin, F. Wang, Y. Lin, J. Zhang, H. Zhang, Z. Wang and B. Wei, *J. Mater. Chem.*, 2012, **22**, 22097–

22101.

12 J. C. Zwinkels and C. Canada, *Encycl. Color Sci. Technol.*, , DOI:10.1007/978-3-642-27851-8.

13 S. J. Zou, Y. Shen, F. M. Xie, J. De Chen, Y. Q. Li and J. X. Tang, *Mater. Chem. Front.*, 2020, **4**, 788–820.

14 H. W. Chen, J. H. Lee, B. Y. Lin, S. Chen and S. T. Wu, *Light Sci. Appl.*, 2018, **7**, 17168.

15 A. Donat-bouillud, I. Le and Y. Tao, *Chem. Mater*, 2000, **12**, 1931–1936.

16 W. P. Lustig, F. Wang, S. J. Teat, Z. Hu, Q. Gong and J. Li, *Inorg. Chem.*, 2016, **55**, 7250–7256.

17 C. X. Chen, Q. F. Qiu, M. Pan, C. C. Cao, N. X. Zhu, H. P. Wang, J. J. Jiang, Z. W. Wei and C. Y. Su, *Chem. Commun.*, 2018, **54**, 13666–13669.

18 I. Ahmed and S. H. Jhung, *Mater. Today*, 2014, **17**, 136–146.

19 M. D. Allendorf, C. A. Bauer, R. K. Bhakta and R. J. T. Houk, *Chem. Soc. Rev.*, 2009, **38**, 1330–1352.

20 S. Wang, L. Ma, Q. Wang, P. Shao, D. Ma, S. Yuan, P. Lei, P. Li, X. Feng and B. Wang, *J. Mater. Chem. C*, 2018, **6**, 5369–5374.

21 Y. Hao, S. Chen, Y. Zhou, Y. Zhang and M. Xu, *Nanomaterials*, , DOI:10.3390/nano9070974.

22 Y. Pan, H. Q. Su, E. L. Zhou, H. Z. Yin, K. Z. Shao and Z. M. Su, *Dalt. Trans.*, 2019, **48**, 3723–3729.

23 D. Yan, Y. Tang, H. Lin and D. Wang, *Sci. Rep.*, 2014, **4**, 4–10.

24 C. Y. Sun, X. L. Wang, X. Zhang, C. Qin, P. Li, Z. M. Su, D. X. Zhu, G. G. Shan, K. Z. Shao, H. Wu and J. Li, *Nat. Commun.*, 2013, **4**, 1–8.

25 F. Xie, T. A. Zhang, D. Dreisinger and F. Doyle, *Miner. Eng.*, 2014, **56**, 10–28.

26 M. Usman, S. Mendiratta and K. L. Lu, *Adv. Mater.*, , DOI:10.1002/adma.201605071.

27 J. Luo, J. W. Wang, J. H. Zhang, S. Lai and D. C. Zhong, *CrystEngComm*, 2018, **20**, 5884–5898.

28 R. B. Lin, Y. He, P. Li, H. Wang, W. Zhou and B. Chen, *Chem. Soc. Rev.*, 2019, **48**, 1362–1389.

29 D. B. Amabilino, D. K. Smith and J. W. Steed, *Chem. Soc. Rev.*, 2017, **46**, 2404–2420.

30 W. Gong, D. Chu, H. Jiang, X. Chen, Y. Cui and Y. Liu, *Nat. Commun.*, 2019, **10**, 1–9.

31 K. Ma, P. Li, J. H. Xin, Y. Chen, Z. Chen, S. Goswami, X. Liu, S. Kato, H. Chen, X. Zhang, J. Bai, M. C. Wasson, R. R. Maldonado, R. Q. Snurr and O. K. Farha, *Cell Reports Phys. Sci.*, 2020, **1**, 100024.

32 X. T. He, Y. H. Luo, D. L. Hong, F. H. Chen, Z. Y. Zheng, C. Wang, J. Y. Wang, C. Chen and B. W. Sun, *ACS Appl. Nano Mater.*, 2019, **2**, 2437–2445.

33 E. Gomez, M. Gutiérrez, B. Cohen, I. Hisaki and A. Douhal, *J. Mater. Chem. C*, 2018, **6**, 6929–6939.

34 Q. Huang, W. Li, Z. Mao, L. Qu, Y. Li, H. Zhang, T. Yu, Z. Yang, J. Zhao, Y. Zhang, M. P. Aldred and Z. Chi, *Nat. Commun.*, 2019, **10**, 1–8.

35 Q. Yin, P. Zhao, R. J. Sa, G. C. Chen, L. Jian, T. F. Liu and R. Cao, *Angew. Chemie - Int. Ed.*, 2018, **57**, 7691–7696.

36 Y. Lin, L. Yu, H. Wang and J. Li, *CrystEngComm*, 2020, **22**, 5946–5948.

37 Y. Hong, J. W. Y. Lam and B. Z. Tang, *Chem. Commun.*, 2009, 4332–4353.

38 Z. Wei, Z. Y. Gu, R. K. Arvapally, Y. P. Chen, R. N. McDougald, J. F. Ivy, A. A. Yakovenko, D. Feng, M. A. Omary

and H. C. Zhou, *J. Am. Chem. Soc.*, 2014, **136**, 8269–8276.

39 L. Le Bras, K. Chaitou, S. Aloïse, C. Adamo and A. Perrier, *Phys. Chem. Chem. Phys.*, 2019, **21**, 46–56.

40 J. Zhu, J. Wang, H. Lu and L. Qiu, *J. Mater. Chem. C*, 2020, **8**, 9147–9162.

41 S. E. Miller, M. H. Teplensky, P. Z. Moghadam and D. Fairen-Jimenez, *Interface Focus*, , DOI:10.1098/rsfs.2016.0027.

42 I. Mjejri, C. M. Doherty, M. Rubio-Martinez, G. L. Drisko and A. Rougier, *ACS Appl. Mater. Interfaces*, 2017, **9**, 39930–39934.

43 K. Ma, P. Li, J. H. Xin, Y. Chen, Z. Chen, S. Goswami, X. Liu, S. Kato, H. Chen, X. Zhang, J. Bai, M. C. Wasson, R. R. Maldonado, R. Q. Snurr and O. K. Farha, *Cell Reports Phys. Sci.*, 2020, **1**, 100024.

44 J. Chao, H. Wang, Y. Zhang, C. Yin, F. Huo, J. Sun and M. Zhao, *New J. Chem.*, 2018, **42**, 3322–3333.

45 G. E. Gomez, R. Marin, A. N. Carneiro Neto, A. M. P. Botas, J. Ovens, A. A. Kitos, M. C. Bernini, L. D. Carlos, G. J. A. A. Soler-Illia and M. Murugesu, *Chem. Mater.*, 2020, **32**, 7458–7468.

46 G. D. Scholes, *Faraday Discuss.*, 2019, **221**, 265–280.

47 R. Damari, O. Weinberg, D. Krotkov, N. Demina, K. Akulov, A. Golombek, T. Schwartz and S. Fleischer, *Nat. Commun.*, 2019, **10**, 1–8.

48 F. P. Kinik, A. Ortega-Guerrero, D. Ongari, C. P. Ireland and B. Smit, *Chem. Soc. Rev.*, 2021, **50**, 3143–3177.

49 S. S. Rajasree, X. Li and P. Deria, *Commun. Chem.*, 2021, **4**, 1–14.

50 T. E. Webber, S. P. Desai, R. L. Combs, S. Bingham, C. C. Lu and R. L. Penn, *Cryst. Growth Des.*, 2020, **20**, 2965–2972.

51 P. Deria, J. Yu, T. Smith and R. P. Balaraman, *J. Am. Chem. Soc.*, 2017, **139**, 5973–5983.

52 R. J. Magyar and S. Tretiak, *J. Chem. Theory Comput.*, 2007, **3**, 976–987.

53 W. Yao, C. Ma, H. Ma, L. Fu, S. Lu, A. Lv, S. Cai, X. Hang, M. Singh, H. Shi, Z. An and W. Huang, *Giant*, 2020, **1**, 100007.

54 J. Yu, J. Park, A. Van Wyk, G. Rumbles and P. Deria, *J. Am. Chem. Soc.*, 2018, **140**, 10488–10496.

55 M. Oldenburg, A. Turshatov, D. Busko, M. Jakoby, R. Haldar, K. Chen, G. Emandi, M. O. Senge, C. Wöll, J. M. Hodgkiss, B. S. Richards and I. A. Howard, *Phys. Chem. Chem. Phys.*, 2018, **20**, 11564–11576.

56 T. N. Tu, H. T. T. Nguyen, H. T. D. Nguyen, M. V. Nguyen, T. D. Nguyen, N. T. Tran and K. T. Lim, *RSC Adv.*, 2019, **9**, 16784–16789.

57 Y. D. Huang, J. H. Qin, X. G. Yang, H. R. Wang, F. F. Li and L. F. Ma, *J. Solid State Chem.*, 2020, **285**, 121252.

58 I. Hod, P. Deria, W. Bury, J. E. Mondloch, C. W. Kung, M. So, M. D. Sampson, A. W. Peters, C. P. Kubiak, O. K. Farha and J. T. Hupp, *Nat. Commun.*, 2015, **6**, 1–9.

59 A. Abhervé, T. Grancha, J. Ferrando-Soria, M. Clemente-León, E. Coronado, J. C. Waerenborgh, F. Lloret and E. Pardo, *Chem. Commun.*, 2016, **52**, 7360–7363.

60 X. Cai, X. Li, G. Xie, Z. He, K. Gao, K. Liu, D. Chen, Y. Cao and S. J. Su, *Chem. Sci.*, 2016, **7**, 4264–4275.

61 S. Jin, H. J. Son, O. K. Farha, G. P. Wiederrecht and J. T. Hupp, *J. Am. Chem. Soc.*, 2013, **135**, 955–958.

62 D. C. Liebler and T. D. McClure, *Chem. Res. Toxicol.*, 1996, **9**, 8–11.

63 M. Meinhardt-Wollweber, C. Suhr, A. K. Kniggendorf and B. Roth, *AIP Adv.*, , DOI:10.1063/1.5025788.

64 X. Kang and M. Zhu, *ACS Mater. Lett.*, 2020, **2**, 1303–1314.

65 X. Zhang, B. Shen, X. Zhang, F. Wang, G. Chi and M. Si, *RSC Adv.*, 2017, **7**, 5928–5936.

66 P. Horn and M. Kertesz, *J. Phys. Chem. C*, 2010, **114**, 12139–12144.

Chapter 4. Conclusion and Future Outlook

Though the application of crystal engineering principles we were able to successfully position pyrene based organic molecule, TBAPy, in several different orientations within a crystal lattice. Resultant topology induced properties that we could assign to specific applications were realized. A semiconducting metal organic framework and a broad range emitting hydrogen bonded framework were both integrated into functional devices. It was the ability to alter the distance and relative locations of the TBAPy ligands using s-block metals and also by the crystallization of TBAPy in the absence of metals that made these functional materials possible. In general, the ability to precisely position functional groups is at the heart of nanotechnology and I hope that the work outlined in this thesis highlights in particular two strategies that have often been overlooked by researchers examining porous crystalline materials; (1) the use of s-block metals as the inorganic component of MOFs and (2) HOFs that can be considerably stabilized and/or functionalized by π orbital staking.

There is a wide scope to explore how s-block metals can be substituted for more commonly used transition metals in a variety of previously reported coordination polymers. Inexpensive, ecologically sound, and biocompatible, there is strong incentive to use metals like sodium and potassium as precursor elements in functional materials.

Our results indicate that s-block MOFs may be more structurally flexible than d-block based MOFs and could be sensitive to a wide range of external stimuli. Temperature, pH, level of solvation, solvent polarity, ion exchange, guest molecules and photo induced structural changes are all factors that have the potential to alter the electronic and structural properties of s-block MOFs making them good candidates for applications in sensing.

The biocompatibility of sodium and potassium and resultant s-block MOFs means there is scope for them to be used in biological applications such as drug delivery and enzyme encapsulation. This also holds true for HOFs, that contain no metals at all. Hopefully this work inspires researchers interested in the aforementioned fields to explore both s-block MOFs and HOFs as potential alternatives to more established and conventional MOFs.

Chapter 5: Appendices

5.1: Supplementary Information for Chapter 2

Structural modulation of the photophysical and electronic properties of pyrene-based 3D metal–organic frameworks derived from s-block metals

Christopher N. Coleman, Patrick C. Tapping, Michael T. Huxley, Tak W. Kee, David M. Huang, Christian J. Doonan and Christopher J. Sumby

Department of Chemistry and Centre for Advanced Nanomaterials, The University of Adelaide, Adelaide, South Australia 5005, Australia.

Contents

1. MOF synthesis and characterisation

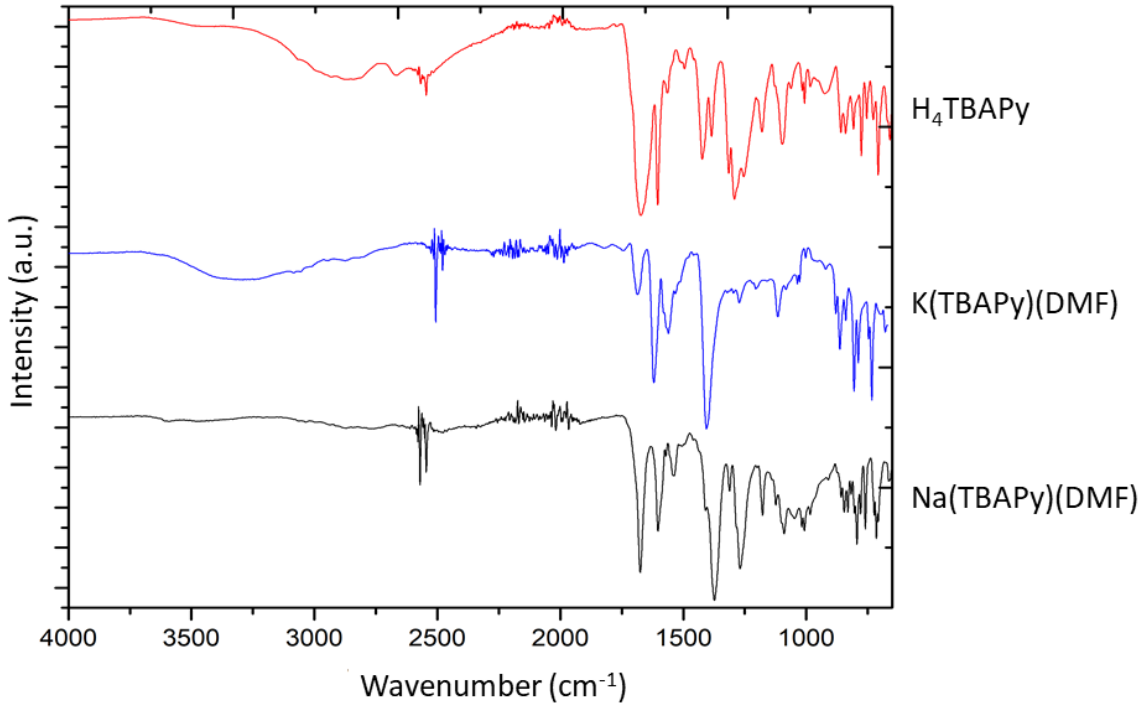

Fig. S1. Fourier-transform infrared (FTIR) spectroscopy. IR spectra of the free linker TBAPy (red), K(TBAPy)(DMF) (blue) and Na(TBAPy)(DMF) (black). Spectra were obtained on a PerkinElmer Spectrum 100 FTIR spectrometer using approximately 0.5 mg of ground sample.

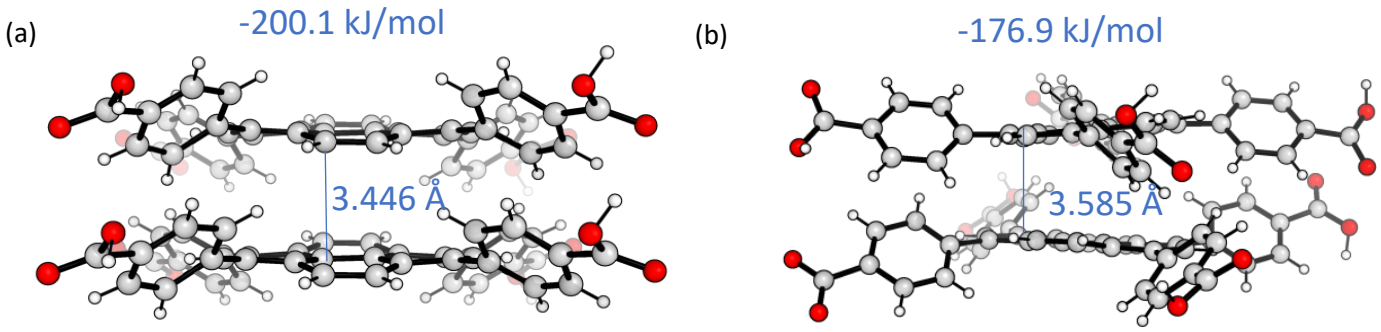

Fig. S2. Perspective views obtained from SCXRD of the distinct dimers in **(a)** K(TBAPy)(DMF) and **(b)** Na(TBAPy)(DMF) showing the respective distances in ångstroms (Å) and intermolecular potentials intermolecular potentials calculated using the "UNI" force field, between the two closest ligands. The distance stated is for the two closest carbon atoms located on adjacent pyrene moieties (not centroid to centroid).

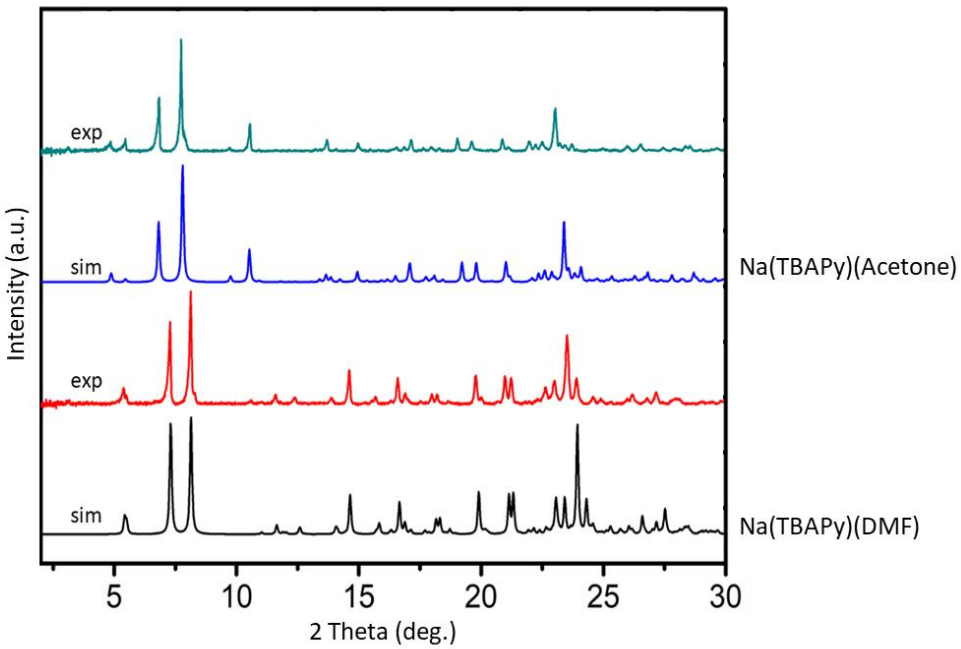

Fig. S3. Powder X-ray diffraction (PXRD) data for the sodium-based MOFs, Na(TBAPy)(acetone) and Na(TBAPy)(DMF). Single crystals of Na(TBAPy)(DMF) were obtained by soaking crystals of Na(TBAPy)(acetone) in DMF, which causes a phase change (details shown in Fig. S4).

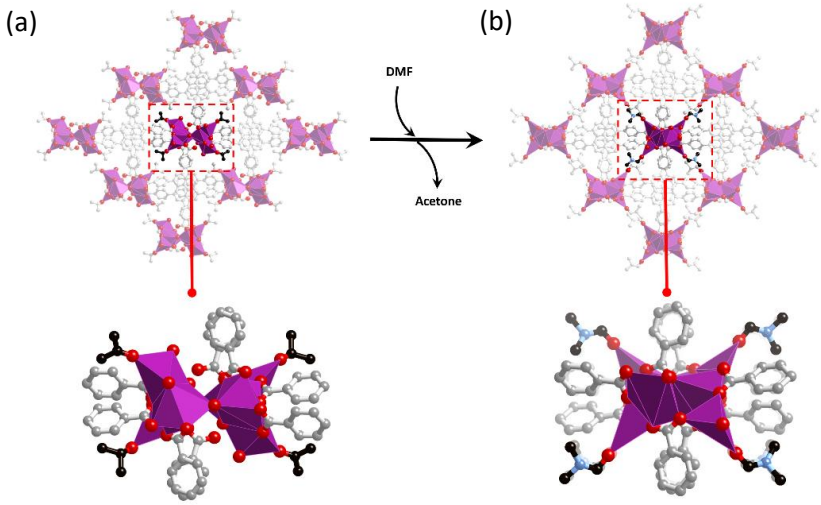

Fig. S4. The overall structure and the coordination environment around the rod-like secondary building unit of **(a)** Na(TBAPy)(acetone) and **(b)** Na(TBAPy)(DMF). Single crystals of Na(TBAPy)(DMF) were obtained by soaking crystals of Na(TBAPy)(acetone) in DMF.

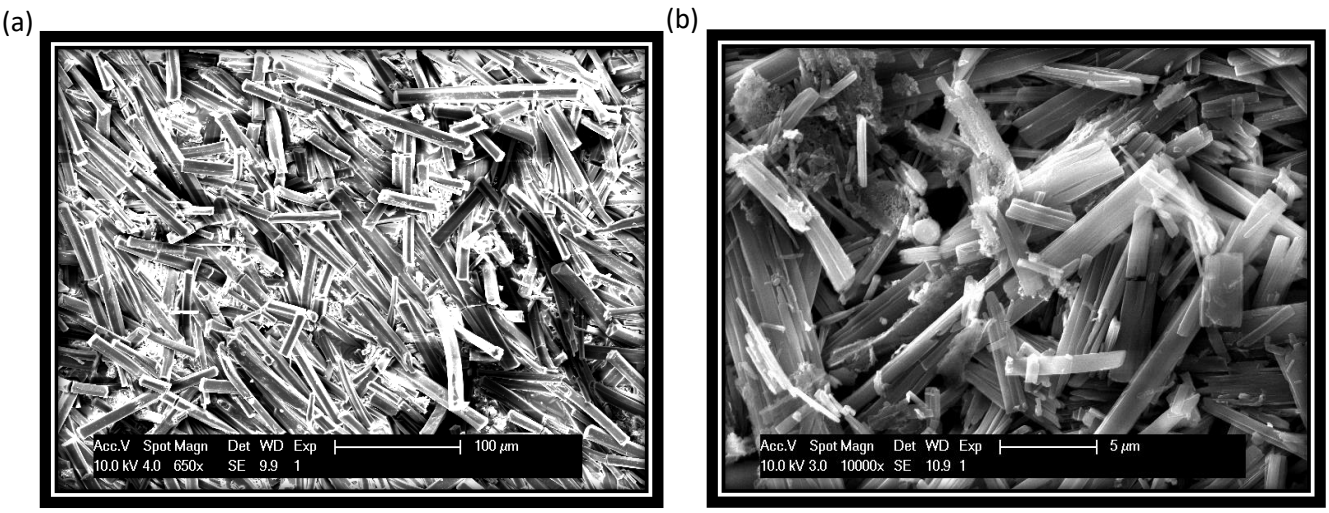

Fig. S5. Scanning electron micrograph (SEM) of microcrystalline **(a)** Na(TBAPy)(DMF) and **(b)** K(TBAPy)(DMF). SEM images were collected using a Philips XL30 field-emission scanning electron microscope (FESEM).

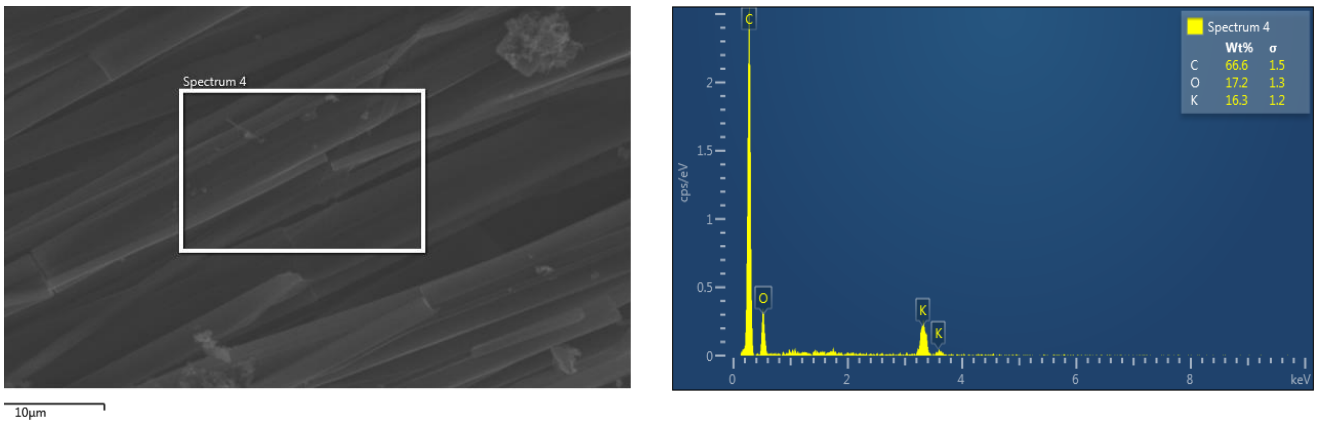

Fig. S6. Energy-dispersive X-ray (EDX) spectrum (right) taken from the identified area in the SEM image (left) of K(TBAPy)(DMF) indicating the primary components of the MOF as being K, C and O. Energy-dispersive X-ray spectroscopy (EDX) was performed on a Philips XL30 field emission scanning electron microscope.

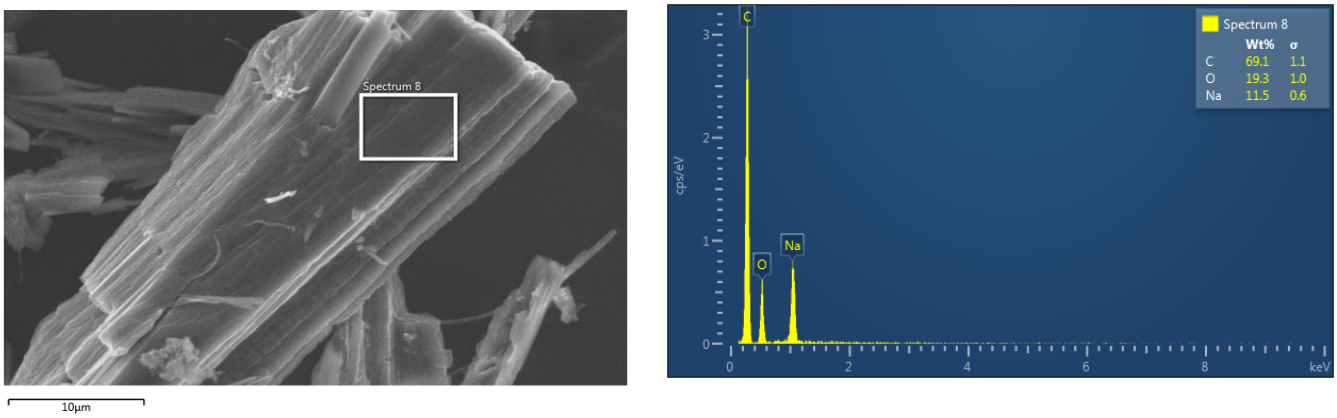

Fig. S7. Energy-dispersive X-ray (EDX) spectrum (right) taken from the identified area in the SEM image (left) of Na(TBAP)(DMF) indicating the primary components of the MOF as being Na, C and O.

2. Ligand (TBAPy) synthesis and characterisation

Synthesis of tetraethyl 4,4′,4″,4‴-(pyrene-1,3,6,8-tetrayl)tetrabenzoic acid or H_4TBAPy. Dioxane (250 mL) was degassed with argon for 1 hour. Tetrabromopyrene (4 g, 7.72 mmol), 4-ethoxycarbonylphenylboronic acid (6.6 g, 36.04 mmol), potassium phosphate (13.08 g, 6.16 mmol) and tetrakis(triphenylphosphine)palladium(0) (0.6 g, 0.53 mmol) were added to the dioxane. The reaction mixture was placed under reflux at 90°C and stirred for 72 hours. The reaction mixture was removed from the heat, water (200 mL) was added, and the mixture was allowed to cool to room temperature. A yellow precipitate was collected by filtration and washed with water (200 mL) and acetone (200 mL). The yellow solid was then dried under a constant flow of nitrogen, crushed to a fine powder in a mortar and pestle and added to a solution of boiling chloroform (300 mL). Once the majority of the solid was dissolved the mixture was removed from heat and filtered whilst still hot. The volume of the chloroform solution was reduced by half by blowing nitrogen over it at room temperature. Methanol (300 mL) was then added that resulted in the formation of a yellow precipitate. After standing 2 hours the yellow solid was collected by filtration and dried overnight.

The yellow solid of the ester was added to a solution of dioxane (100mL). Potassium hydroxide (1.4 g, 25 mmol) was added to water (80 mL) and the aqueous solution was combined with the dioxane solution. The reaction mixture was heated under reflux for 24 hours, allowed to cool and then concentrated HCl was slowly added to until a yellow precipitate formed. The mixture was stirred for another hour and allowed to sit for 3 hours before the yellow solid was filtered and washed with water (200 mL x 3). The yellow solid was dried under a flow nitrogen

for 3 hours. The dried solid was then dissolved in boiling DMF and filtered while hot. The DMF solution was allowed to cool and dichloromethane was added until a yellow precipitate formed. The yellow solid was collected by filtration and washed with dichloromethane (100 mL). The product was further dried in under vacuum for 24 hours to afford H_4TBAPy as a pale-yellow powder (5.20 g, 85% yield). ^{1}H NMR: 13.09 (s, 4H), 8.20 (s, 4H), 8.17 (d, 8H), 8.07 (s, 2H), 7.86 (d,8H).

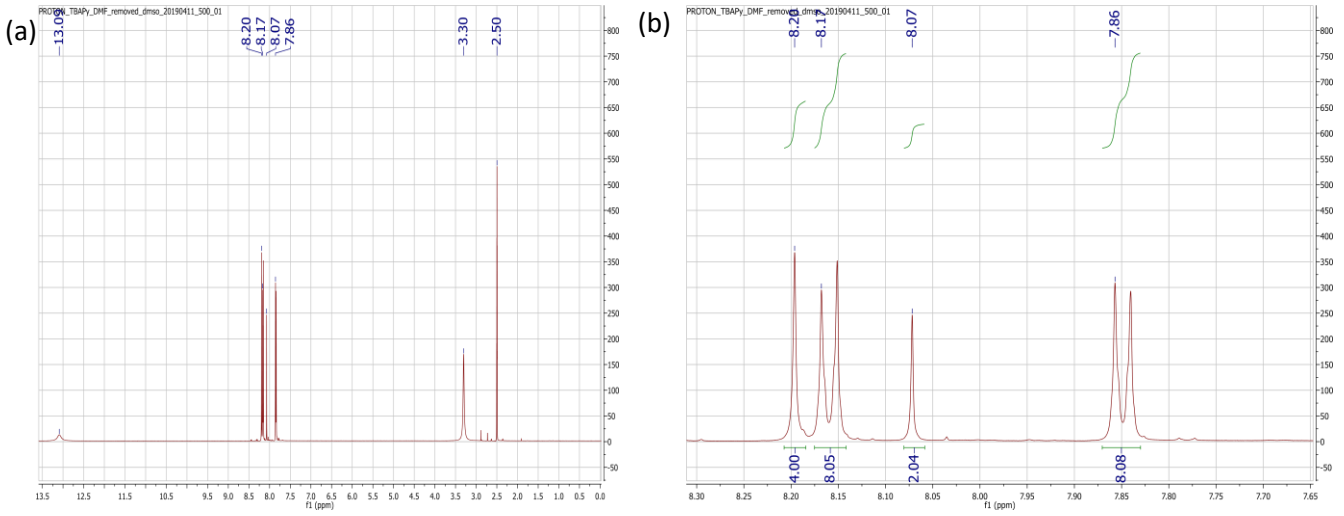

Fig. S8. (a) Full ^{1}H NMR spectrum of TBAPy in DMSO-d_6 (residual solvent at 2.50 ppm and water at 3.30 ppm are indicated). The COOH signal at 13.09 ppm is shown. **(b)** Enlargement of the aromatic region of the spectrum providing the chemical shift and integration pertaining specifically to TBAPy ligand core and phenyl substituents.

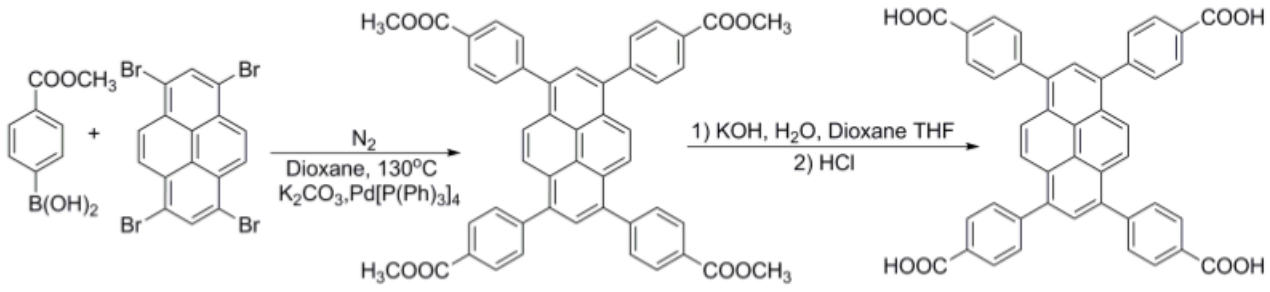

Scheme S1. Procedure used to synthesis TBAPy over two steps from commercially available starting materials.

3. Fitting of time-resolved fluorescence data

Table S1. Multiexponential fitting parameters for the time-resolved fluorescence kinetics of K(TBAPy)(DMF) and Na(TBAPy)(DMF) shown in Figs. 3e and 3f.

Name	λ (nm)	A_1	τ_1 (ns)	A_2	τ_2 (ns)	A_3	τ_3 (ns)
K(TBAPy)(DMF)	490	0.68 ± 0.02	2.63 ± 0.09	0.32 ± 0.02	9.7 ± 0.3	–	–
	510	0.59 ± 0.02	3.4 ± 0.2	0.41 ± 0.03	11.0 ± 0.4	–	–
	530	0.54 ± 0.01	3.2 ± 0.1	0.46 ± 0.02	11.2 ± 0.2	–	–
	555	0.51 ± 0.02	3.1 ± 0.1	0.49 ± 0.02	11.8 ± 0.2	–	–
Na(TBAPy)(DMF)	490	0.88 ± 0.01	1.02 ± 0.03	0.10 ± 0.01	4.9 ± 0.7	0.02 ± 0.01	16 ± 3
	510	0.73 ± 0.01	1.16 ± 0.04	0.21 ± 0.01	4.9 ± 0.4	0.07 ± 0.01	16 ± 1
	530	0.59 ± 0.01	1.31 ± 0.06	0.28 ± 0.01	5.1 ± 0.4	0.13 ± 0.01	17.0 ± 0.7
	555	0.43 ± 0.03	1.5 ± 0.1	0.36 ± 0.03	5.2 ± 0.5	0.21 ± 0.02	17.7 ± 0.6

4. Additional crystallographic details and structural data.

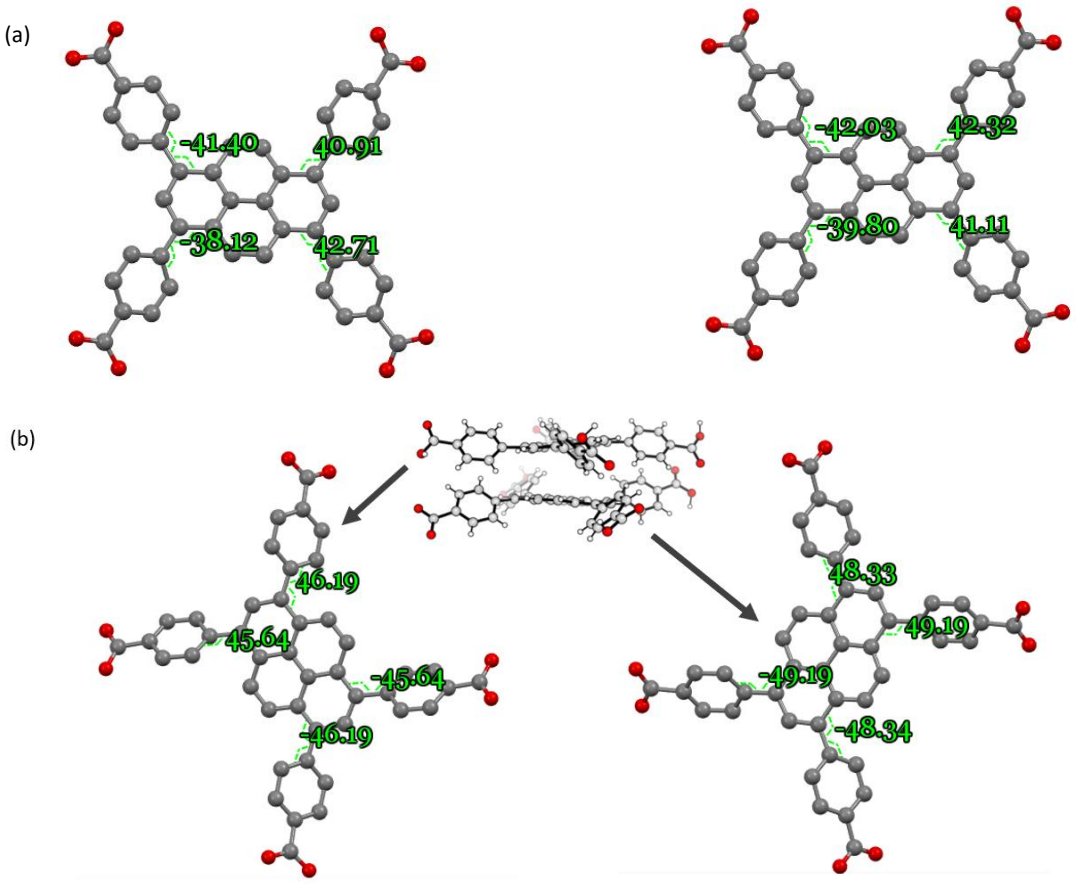

Fig. S9. Pyrene–benzoate dihedral angles (in degrees) for the two structurally distinct ligands contained within each unit cell for (a) K(TBAPy)(DMF) and (b) Na(TBAPy)(DMF).

Fig. S10. Photograph of crystallisation via evaporation of DMF:H_20 (50:50) to give microcrystalline samples of Na(TBAPy)(DMF) (left) and K(TBAPy)(DMF) (right).

Additional refinement details

For Na(TBAPy)(DMF). The crystals of Na(TBAPy)(DMF) were small and poorly diffracting as they are obtained by solvent exchange of a related structure, Na(TBAPy)(acetone), which causes a single crystal-to-single crystal phase change (they could not be obtained directly). The data was omitted above $2\theta = 50^\circ$ to improve the data quality.

For Na(TBAPy)(acetone). There was disorder of the coordinated acetone in the structure and DFIX restraints were used to maintain chemically sensible bond lengths and angles. SIMU and EADP restraints were also used to sensibly refine the acetone molecule.

For K(TBAPy)(DMF). The solvent molecules that coordinate the rod-like SBU in K(TBAPy)(DMF) are heavily disordered, possibly due to a need to accommodate a mixture of DMF, water and a coordinated carbonate anion. DFIX and ISOR restraints were used to refine the most well behaved DMF molecule but the other solvates were truncated to the coordinated oxygen atoms as the data was not of sufficient quality to allow refinement. The formula of the MOF was determined by considering the non-squeezed structure; a mixture of DMF, water and carbonate anion was included in the formula to accurately describe the structure.

Crystallographic information files (cif) have been deposited with the Cambridge Crystallographic Database (CCDC). Deposition numbers 2026823 (Na(TBAPy)(DMF)), 2026825 (Na(TBAPy)(acetone)), and 2026827 (K(TBAPy)(DMF)).

Table S2. Crystal data and structure refinement for Na(TBAPy)(DMF), Na(TBAPy)(acetone), and K(TBAPy)(DMF).

Identification code	**Na(TBAPy)(DMF)**	**Na(TBAPY)acetone**	**K(TBAPy)(DMF)**
Empirical formula	$C_{50}H_{36}N_2O_{10}Na_4$	$C_{50}H_{46.5}O_{16.25}Na_4$	$C_{98.25}H_{83.25}N_{3.25}O_{38.5}K_9$
Formula weight	916.77	999.33	2277.33
Temperature/K	150(2)	150(2)	100(2)
Crystal system	monoclinic	monoclinic	monoclinic
Space group	$P2_1/n$	$P2_1/n$	$P2_1/c$
a/Å	21.7180(13)	22.8138(11)	17.329(4)
b/Å	7.8066(6)	7.9496(4)	36.085(7)
c/Å	24.1817(17)	26.0910(11)	15.194(3)
β/°	90.887(6)	96.564(4)	94.59(3)
Volume/Å^3	4099.4(5)	4700.9(4)	9471(3)
Z	4	4	4
ρ_{calc}g/cm^3	1.485	1.412	1.597
μ/mm^{-1}	0.139	0.136	0.505
F(000)	1896.0	2082.0	4698.0
Crystal size/mm^3	0.2 × 0.07 × 0.06	0.4 × 0.1 × 0.1	0.43 × 0.15 × 0.07
Radiation	MoKα (λ = 0.71073)	MoKα (λ = 0.71073)	Synchrotron (λ = 0.71073)
2θ range for data collection/°	6.474 to 50.118	6.746 to 58.722	2.258 to 57.978
Index ranges	-25 ≤ h ≤ 25, -9 ≤ k ≤ 9, -28 ≤ l ≤ 28	-31 ≤ h ≤ 30, -10 ≤ k ≤ 10, -35 ≤ l ≤ 35	-23 ≤ h ≤ 23, -47 ≤ k ≤ 47, -20 ≤ l ≤ 19
Reflections collected	115555	159057	119477
Independent reflections	7259 [R_{int} = 0.3294, R_{sigma} = 0.1651]	12168 [R_{int} = 0.1544, R_{sigma} = 0.1193]	20002 [R_{int} = 0.0282, R_{sigma} = 0.0175]
Data/restraints/parameters	7259/0/599	12168/34/690	20002/16/1205
Goodness-of-fit on F^2	1.119	1.029	1.053
Final R indexes [I>=2σ (I)]	R_1 = 0.1321, wR_2 = 0.3476	R_1 = 0.0698, wR_2 = 0.1399	R_1 = 0.0722, wR_2 = 0.2254
Final R indexes [all data]	R_1 = 0.2167, wR_2 = 0.3874	R_1 = 0.1475, wR_2 = 0.1690	R_1 = 0.0829, wR_2 = 0.2364
Largest diff. peak/hole / e Å^{-3}	0.72/-0.47	0.43/-0.38	1.92/-0.53

5. Preparation of LED device

A glass indium-tin oxide (ITO) substrate was cleaned using isopropanol and distilled water then dried thoroughly. 50 mg of Na(TBAPy)(DMF) was ground into a fine powder and added to 20 mL of acetone to create a suspension. The suspension was spin-coated (4000rpm for 30secs) on to the conductive side of the glass substrate. Several MOF layers were added (10-15) until an even coating had been achieved. Next, a single layer of light-emitting copolymer poly[(9,9-dioctyl-2,7divinylenefluorenylene)-alt-co-(2-methoxy-5-(2-ethylhexyloxy)-1,4-phenylene)] (PFO-co-MEH-PPV), which had been pre-dissolved in dichloromethane at a concentration of 10 mg/mL, was added using the same spin coating process. Once dried, a cotton swab dipped in chloroform was used to expose the ITO on one of the corners of the glass substrate. The exposed corner was connected the negative terminal of a power source and a gallium/indium eutectic was used to connect the light-emitting layer to the positive terminal (see Fig. S11).

(a) (b) (c)

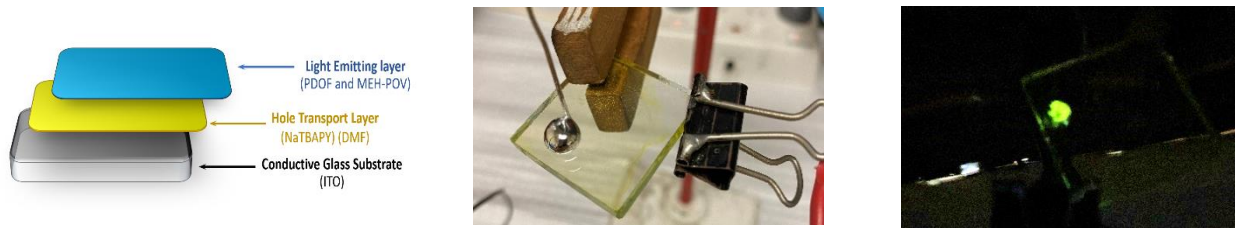

Fig. S11. **(a)** Schematic of light-emitting diode fabricated using Na(TBAPy)(DMF) as a hole transport layer, **(b)** photograph of coated substrate connected to a DC power source and **(c)** photograph of active LED emitting light at 4.45 V (26 mA).

6. Density functional theory (DFT) calculations

For each MOF, DFT calculations were performed using Q-Chem version 5.1.1[1] on a fragment comprising TBAPy ligands extracted from the experimental X-ray crystal structure (in each case, the closest ligand pair in the framework was chosen). To mimic the geometric constraints in the MOF framework, the carboxylate carbon and oxygen atoms in the ligands were fixed at their positions in the experimental crystal structure during geometry optimizations. For calculations of an isolated TBAPy ligand, no geometric constraints were applied. In all case, each carboxylate group in the TBAPy ligands was terminated by H^+ to enforce charge neutrality in the neutral systems and a +1 charge in the cationic systems used for the charge-transfer calculations. Geometry optimizations in the ground state were initiated from the experimental crystal structure, while optimizations of excited states and charge-localized states were initiated from the optimized ground-state geometry.

To calculate the electronic absorption spectrum of each system, the 30 lowest energy singlet transitions were computed in the ground-state (S0) geometry. Since Kasha's rule dictates that emission occurs only from the lowest excited state, the electronic emission spectrum was calculated from the lowest energy singlet transition computed in the geometry of the first (S_1) excited singlet state.

To calculate the rate constant for hole transfer between the TBAPy ligands in each MOF dimer, the geometry was optimized with the net +1 charge of the system constrained to one of the ligands using CDFT. The electronic coupling V_{da} between diabatic states in which the +1 charge is localised on one or the other ligand and the reorganization energy λ was calculated using CDFT-CI, with the V_{da} given by either off-diagonal element and λ given by the difference between the diagonal elements of the CDFT-CI Hamiltonian matrix the orthogonalized basis. As such, the calculated reorganisation energy only includes the inner-sphere component due to relaxation of the molecules directly involved in the charge transfer and excludes the outer-sphere component due to relaxation of the environment, but the latter contribution is expected to be small compared with the inner-sphere component in a rigid MOF framework. This level of approximation is also expected to be sufficient for comparison of relative hole-transfer rates for the different MOFs. The hole-transfer rate constant k_h was calculated with Marcus electron-transfer theory using[2]

$$k_{\mathrm{h}} = \frac{2\pi}{\hbar}|V_{\mathrm{da}}|^2\sqrt{\frac{1}{4\pi k_{\mathrm{B}}T\lambda}}\exp\left[-\frac{(\Delta G^{\circ}+\lambda)^2}{4\lambda k_{\mathrm{B}}T}\right] \quad (1)$$

where the free-energy change ΔG° for the hole transfer process is zero because the donor and acceptor ligands are identical.

Most calculations used default values of parameters in Q-Chem version 5.1.1, but to obtain SCF convergence in calculations using the 6-31+G* basis set, BASIS_LIN_DEP_THRESH (which sets the threshold for determining linear dependence in the basis set) was set to 5 to reduce the threshold for linear dependence, XC_GRID (which specifies the type of grid to use in DFT calculations) was set to 3 to increase the number of grid points, and THRESH (which sets the cutoff for neglect of two electron integrals) was set to 12 (or 14 for CDFT-CI calculations) to reduce the threshold.

(a) (b) (c)

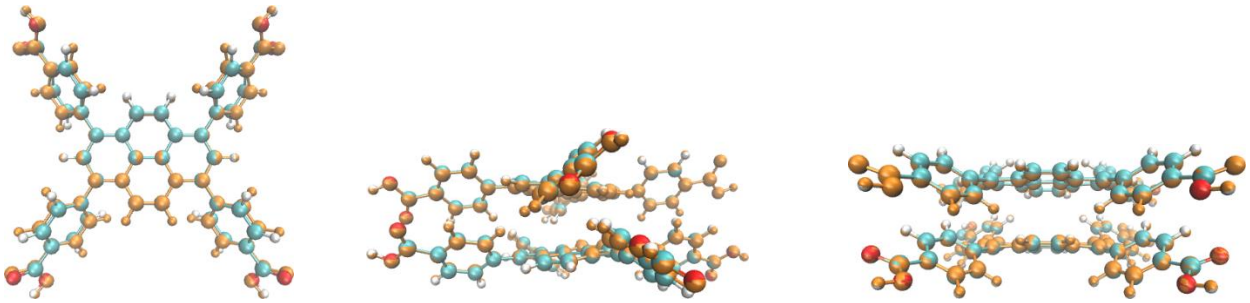

Fig. S12. Overlay of optimised ground-state (S0) and lowest energy excited-state (S1) structures (with atoms in excited-state structures in orange) for **(a)** TBAPy monomer, **(b)** Na(TBAPy)(DMF) MOF dimer, and **(c)** K(TBAPy)(DMF) MOF dimer. The most significant change in the geometry of the TBAPy monomer is the reduction in the pyrene – benzoate dihedral angle by an average of 12.1° (from 57.2° to 45.1°) from the S0 to S1 structures. The MOF dimers hardly change between the S0 and S1 structures due to the geometric constraints on the positions of carboxyl atoms, with the corresponding dihedral decreasing on average by 1.7° (from 47.4° to 45.6°) and 1.9° (from 42.1° to 40.2°) for Na(TBAPy)(DMF) and K(TBAPy)(DMF), respectively. The calculated dihedral angles are the same ones as shown in Fig. S9 and show reasonable agreement with experiment for the S0 structures.

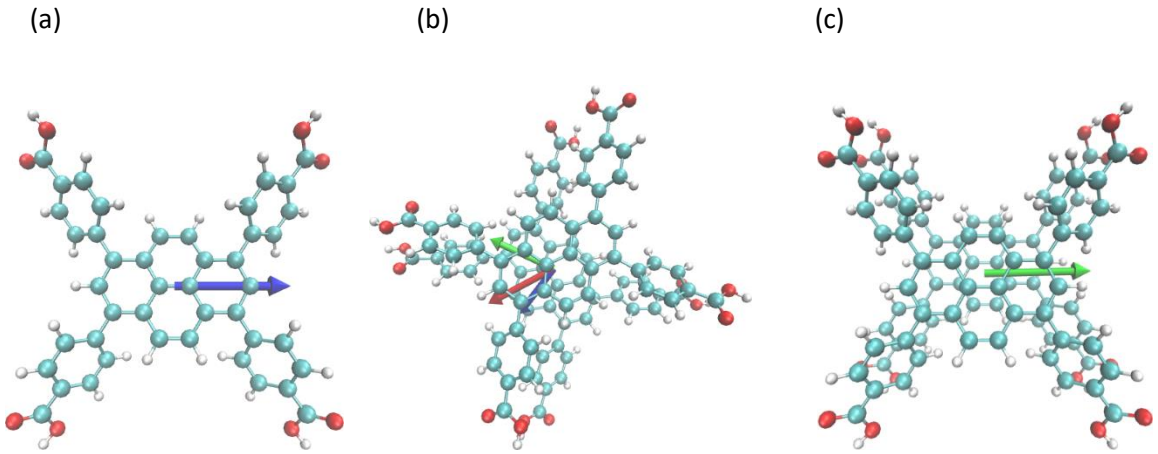

Fig. S13. Calculated transition dipole moments (TDMs) for **(a)** TBAPy monomer, **(b)** Na(TBAPy)(DMF) MOF dimer, and **(c)** K(TBAPy)(DMF) MOF dimer. The TDM for the S0→S1 and S0→S2 transitions in the S0 geometry are in blue and green, respectively, and that for the S0→S1 transition in the S1 geometry is shown in red. Only the S0→S1 transitions in the S0 geometry is shown in **(a)** and only the S0→S2 transitions in the S0 geometry in **(c),** since the S0→S1 transition has negligible TDM for K(TBAPy)(DMF) and the TDMs do not change direction noticeably in the S1 geometry for the TBAPy monomer or K(TBAPy)(DMF) MOF dimer. In both **(b)** and **(c)**, the TDMs shown are aligned in the plane of the stacked pyrene cores.

Charge-transfer rate constants

Table S3. Calculated electronic couplings, reorganisation energies, and hole-transfer rate constants for MOF TBAPy dimers.

MOF	electronic coupling V_{da} (meV)	reorganisation energy λ (meV)	hole transfer rate constant k_h (s^{-1})
Na(TBAPy)(DMF)	45.6	256	5.7×10^{12}
K(TBAPy)(DMF)	19.8	230	1.5×10^{12}
NU-1000	3.6	262	3.3×10^{10}

The calculated electronic coupling and reorganisation energy for NU-1000 are comparable (2.7 and 280 meV, respectively) to those calculated previously by Patwardhan and Schatz[3] for the same ligand dimer in NU-1000 but using a different density functional, basis set, and charge-transfer calculation method to that used here.

7. References

1 Y. Shao, Z. Gan, E. Epifanovsky, A. T. B. Gilbert, M. Wormit, J. Kussmann, A. W. Lange, A. Behn, J. Deng, X. Feng, D. Ghosh, M. Goldey, P. R. Horn, L. D. Jacobson, I. Kaliman, R. Z. Khaliullin, T. Kuš, A. Landau, J. Liu, E. I. Proynov, Y. M. Rhee, R. M. Richard, M. A. Rohrdanz, R. P. Steele, E. J. Sundstrom, H. L. Woodcock, P. M. Zimmerman, D. Zuev, B. Albrecht, E. Alguire, B. Austin, G. J. O. Beran, Y. A. Bernard, E. Berquist, K. Brandhorst, K. B. Bravaya, S. T. Brown, D. Casanova, C. M. Chang, Y. Chen, S. H. Chien, K. D. Closser, D. L. Crittenden, M. Diedenhofen, R. A. Distasio, H. Do, A. D. Dutoi, R. G. Edgar, S. Fatehi, L. Fusti-Molnar, A. Ghysels, A. Golubeva-Zadorozhnaya, J. Gomes, M. W. D. Hanson-Heine, P. H. P. Harbach, A. W. Hauser, E. G. Hohenstein, Z. C. Holden, T. C. Jagau, H. Ji, B. Kaduk, K. Khistyaev, J. Kim, J. Kim, R. A. King, P. Klunzinger, D. Kosenkov, T. Kowalczyk, C. M. Krauter, K. U. Lao, A. D. Laurent, K. V. Lawler, S. V. Levchenko, C. Y. Lin, F. Liu, E. Livshits, R. C. Lochan, A. Luenser, P. Manohar, S. F. Manzer, S. P. Mao, N. Mardirossian, A. V. Marenich, S. A. Maurer, N. J. Mayhall, E. Neuscamman, C. M. Oana, R. Olivares-Amaya, D. P. Oneill, J. A. Parkhill, T. M. Perrine, R. Peverati, A. Prociuk, D. R. Rehn, E. Rosta, N. J. Russ, S. M. Sharada, S. Sharma, D. W. Small, A. Sodt, T. Stein, D. Stück, Y. C. Su, A. J. W. Thom, T. Tsuchimochi, V. Vanovschi, L. Vogt, O. Vydrov, T. Wang, M. A. Watson, J. Wenzel, A. White, C. F. Williams, J. Yang, S. Yeganeh, S. R. Yost, Z. Q. You, I. Y. Zhang, X. Zhang, Y. Zhao, B. R. Brooks, G. K. L. Chan, D. M. Chipman, C. J. Cramer, W. A. Goddard, M. S. Gordon, W. J. Hehre, A. Klamt, H. F. Schaefer, M. W. Schmidt, C. D. Sherrill, D. G. Truhlar, A. Warshel, X. Xu, A. Aspuru-Guzik, R. Baer, A. T. Bell, N. A. Besley, J. Da Chai, A. Dreuw, B. D. Dunietz, T. R. Furlani, S. R. Gwaltney, C. P. Hsu, Y. Jung, J. Kong, D. S. Lambrecht, W. Liang, C. Ochsenfeld, V. A. Rassolov, L. V. Slipchenko, J. E. Subotnik, T. Van Voorhis, J. M. Herbert, A. I. Krylov, P. M. W. Gill and M. Head-Gordon, *Mol. Phys.*, 2015, **113**, 184–215.

2 R. A. Marcus, *J. Chem. Phys.*, 1956, **24**, 966–978.

3 S. Patwardhan and G. C. Schatz, *J. Phys. Chem. C*, 2015, **119**, 24238–24247.

7.2: Supporting Information for Chapter 3

Methods

Ligand (TBAPy) synthesis and characterisation: a detailed method including characterization by H^1NMR for TBAPy synthesis is described in Chapter 2.

Photoluminescence quantum yield: Quantum yield measurements were obtained through the spectrofluorimeter (Edinburgh Instruments F980) with a 15 cm integrating sphere. Sample emission was passed through a focusing lens into a monochromator (TMS302-M), followed by an air-cooled photomultiplier (Hamamatsu R928) that was used for detection. Before quantum yield calculation, the emission intensity of each scan was corrected for the detection efficiency. The samples were excited by a 405 nm continuous-wave fibre laser, which was first passed through a 430 nm short pass filter and lightly focused onto the sample by a silica lens. Direct excitation of the sample was used with a baffle between the sample and emission port.

Spectroscopy. Diffuse reflectance spectra were measured on solid samples using a Varian Cary 5000 spectrophotometer fitted with a Praying Mantis Diffuse Reflectance Accessory. Steady-state fluorescence measurements on solid samples were conducted on a Perkin Elmer LS 55 Spectrometer (slit widths: ex 2.5nm, em 2.5 nm) . Time-resolved fluorescence data were obtained using time-correlated single photon counting (TCSPC) on a commercial spectrometer (Halcyone, Ultrafast Systems). Solid MOF samples were mounted inside 0.8 mm glass capillaries and measured in reflection mode. The 400 nm excitation laser was generated by frequency doubling a portion of the output of a Ti-sapphire oscillator (Tsunami, Spectra Physics), with a pulse duration of ~100 fs and a pulse-picker used to reduce the repetition rate to 6.7 MHz.

Preparation of micro PCF-1: H_4TBAPy (50mg, 73µmol) was added to DMF (30mL). The solution was allowed to slowly evaporate over a number of days under ambient conditions resulting in the formation of needle like yellow crystals.

Preparation nano PCF-1: H_4TBAPy (10 mg, 0.015 mmol) was dissolved in 3 mL of DMF to which 10 mL H_2O was add-ed and stirred for 5 minutes. Then 8.3 mL of EtOH was add-ed to the mixture. The products were separated via centrifugation at 12000 rpm for 15 minutes and washed with EtOH and acetone.

Preparation nano PCF-1 (β-Carotene): 10 mg of Beta Carotene was added to the above solution of nano PFC-1 and stirred at room temperature for 4 hours.

Preparation of LED devices: A commercially available blue LED (max emission 468nm) was coated dropwise in a suspension of nano-PFC-1 (DMF,H_2O,EtOH) repeatedly under a constant flow of warm air until an even coating of PFC-1 was achieved. A voltage of 9 V was applied to the device with a current of 5mA for spectroscopy measurements and photographs. For the β-Carotene doped device the same procedure was carried out using nano PFC-1(β-Carotene) in place of nano PFC-1.

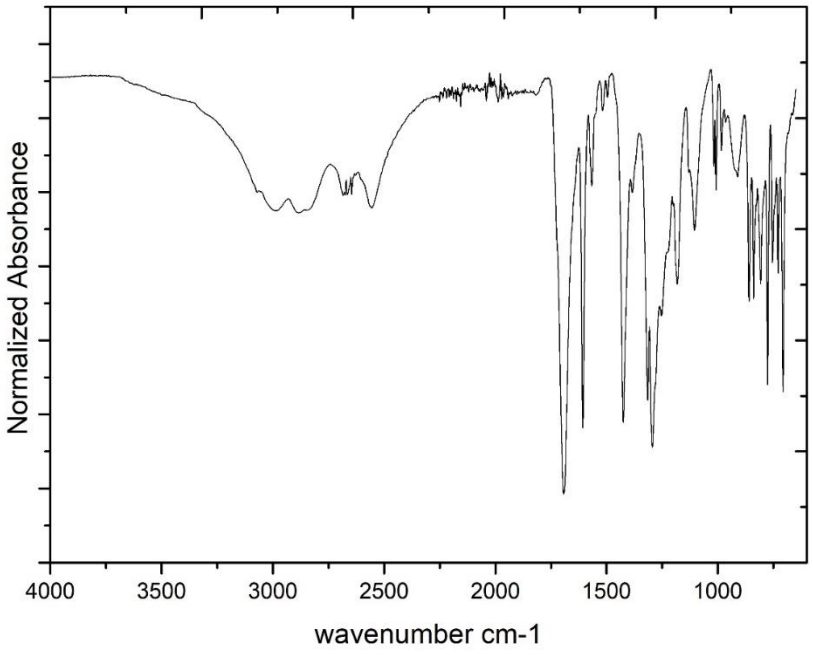

Fig. S1. Fourier-transform infrared (FTIR) spectroscopy. IR spectra of the PFC-1 Spectra were obtained on a PerkinElmer Spectrum 100 FTIR spectrometer using approximately 0.5 mg of ground sample.

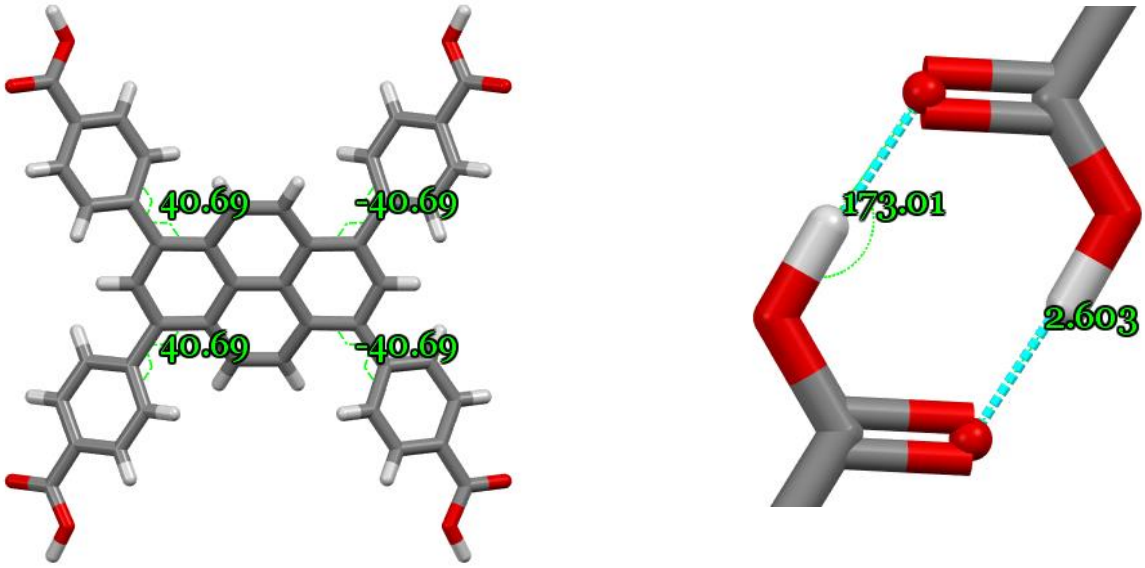

Fig. S2. **(a)** Pyrene–benzoate dihedral angles (in degrees) present in the ligand, **(b)** distance in ångstroms (O - O) and angles in degrees of the hydrogen bonds.

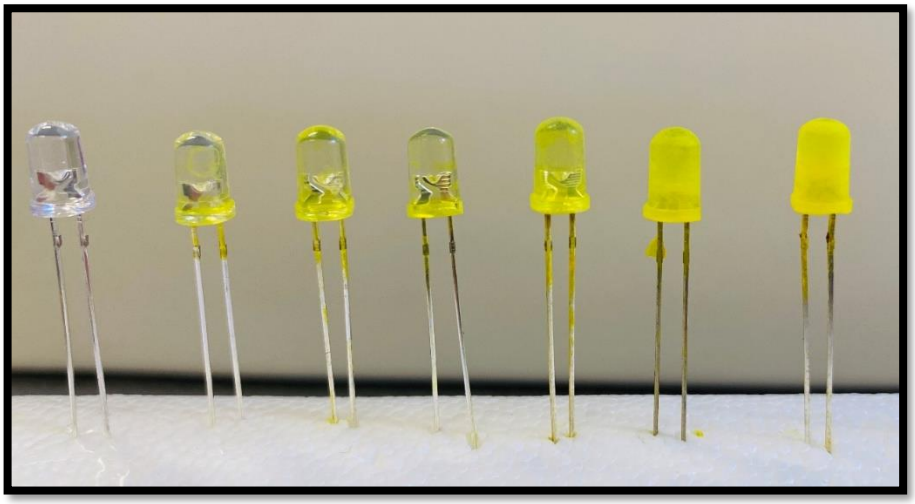

Fig. S3. Commercially available blue (468nm) LEDs coated with increasing amounts of PFC-1.

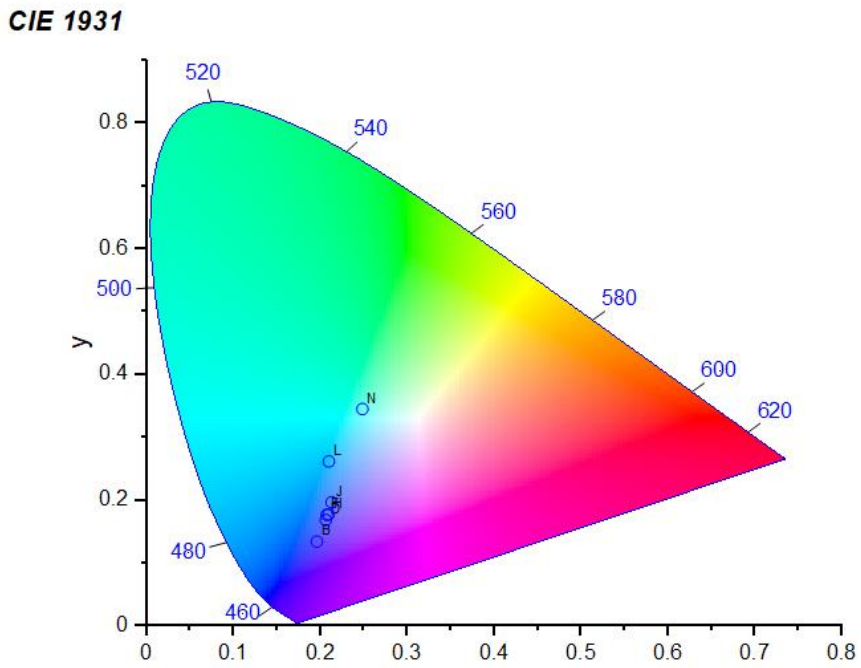

Fig. S4. CIE 1931 chromaticity co-ordinates obtained during the optimization of the blue LED/PFC-1 devices that can be seen in Fig S3.

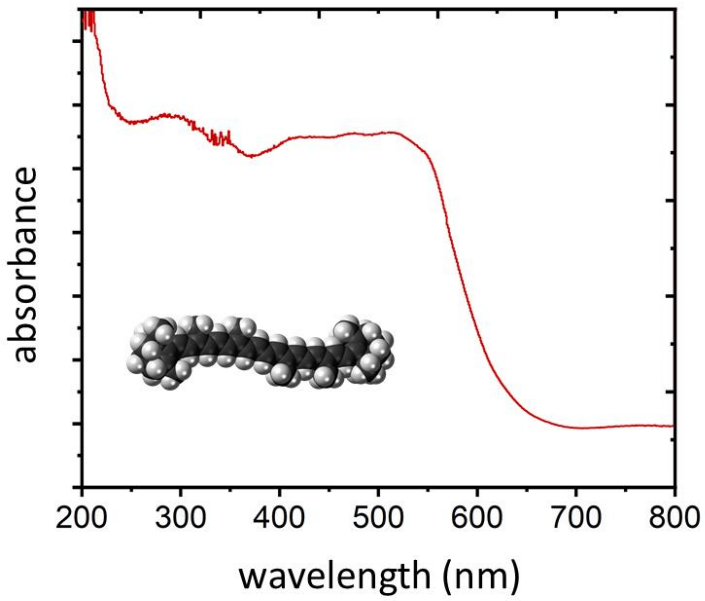

Fig. S5. Absorption spectrum of dry beta carotene powder.

Fig. S6. Dry PFC-1 fluorescing under 365nm light.

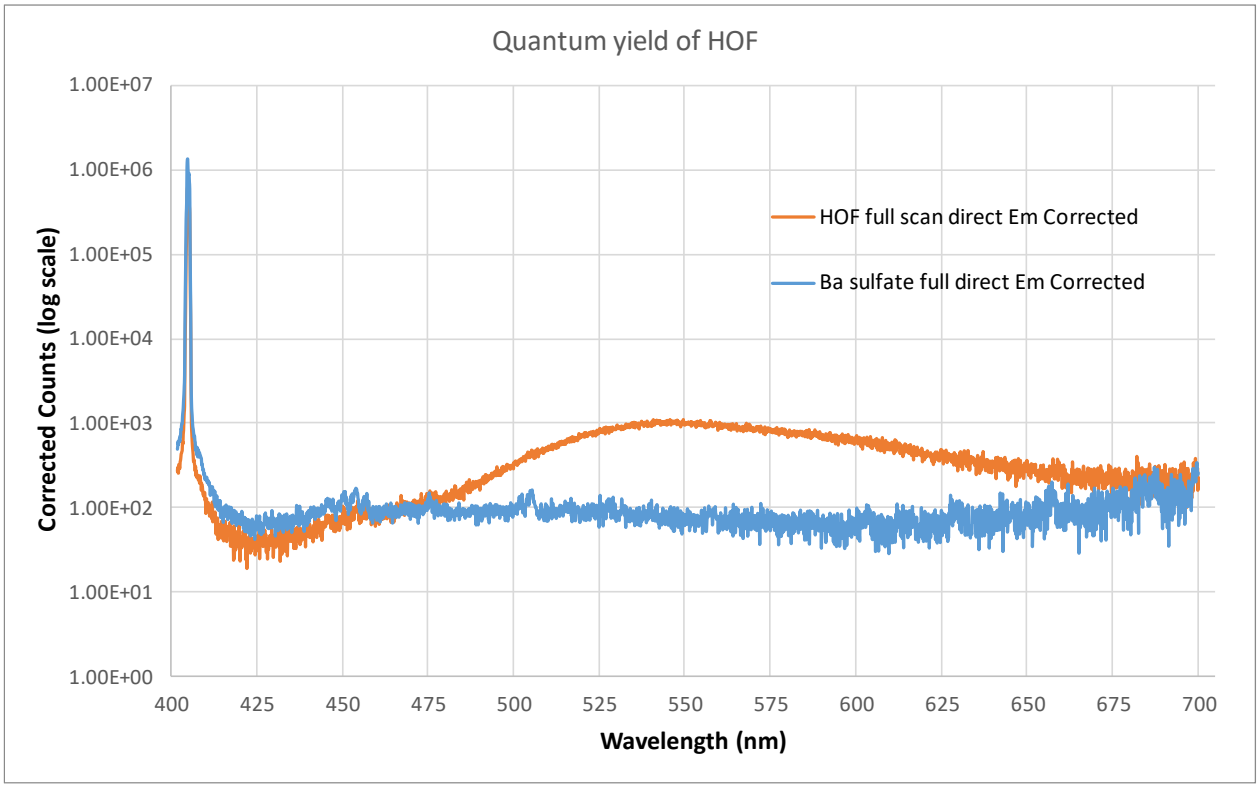

Fig. S7. Photo luminescence quantum yield results.